Carl von Ossietzky
Universität
Oldenburg

Sensor Integration for Ship Motion Analysis

Von der Fakultät für Informatik, Wirtschafts- und Rechtswissenschaften
der Carl von Ossietzky Universität Oldenburg
zur Erlangung des Grades und Titels eines

Doktors der Ingenieurwissenschaften (Dr.-Ing.)

angenommene Dissertation

von Frau Chen Zhang

geboren am 11. 01. 1989 in Shaanxi, China

Gutachter

Prof. Dr.-Ing. Axel Hahn

Prof. Dr. Alexander Härting

Tag der Disputation

09. 05. 2022

Abstract

The ship motions induced by the waves consist of two types, one is translations surge, sway and heave. The other one is rotations, containing roll, pitch and yaw. There is not a unique point for all those motions, therefore in this work a definition of a center of rotation (CR) is proposed. The CR is the point where the linear accelerations are influenced the least by the rotations. Sea trials were performed on several ships with various sizes and in diverse sea environments to determine the locations of CR. Low-cost inertial sensor boxes were installed onboard and utilized to measure and record ship motions. Three linear accelerations and three angular rates were recorded from the sensor boxes at an arbitrary position and regarded as the observations for the constructed mathematic model.

All the measured data needed to be processed in the first place, then introduced into a determination algorithm to estimate the location of CR and the ship motions at CR. Based on the structure of the known information and desired results, the Kalman filter is applied to construct the corresponding mathematic model. In addition, the transformation between relative coordinate systems is implemented and the measured motions data including the undesired noises and bias are processed as well. The angles used for the transformation are determined by a high-pass filter and the integration of the measured angular rates. Then the transformation between the ship body-fixed frame and the horizontal inertial frame with these angles is built, along with the additional unknown offset vector. The offset, is the investigated variable of this work, is defined as the distance between the CR and the sensor's location in three dimensions.

The results indicate that the Kalman filter can be applied to determine the location of CR uniquely. This location depends on the ship's dynamic characteristics. It is also found that there is a clear dependency on the angle of attack of the incoming waves. Different trials show that similar sea state conditions lead to similar positions of the CR. Thus, the CR actually bears information on the sea state. It is shown that with proper signal conditioning even low-cost sensor boxes provide sufficient quality data as input for the Kalman filter.

Abstract

Die durch die Wellen verursachten Schiffsbewegungen lassen sich in zwei Arten unterteilen: Die eine sind die Translationen von Schnellen, Querversatz und Tauchen. Die andere Art sind die Rotationen, die Rollen, Stampfen und Gieren umfasst. Da es keinen eindeutigen Punkt für alle diese Bewegungen gibt, wird in dieser Arbeit eine Definition des Drehpunkts (CR) vorgeschlagen. Der Drehpunkt ist der Punkt, an dem die linearen Beschleunigungen am wenigsten von den Drehungen beeinflusst werden. Auf mehreren Schiffen unterschiedlicher Größe und in verschiedenen Meeresumgebungen wurden Seeversuche durchgeführt, um die Lage des CR zu bestimmen. Kostengünstige Trägheitssensorboxen wurden an Bord installiert und zur Messung und Aufzeichnung der Schiffsbewegungen verwendet. Drei lineare Beschleunigungen und drei Winkelgeschwindigkeiten wurden von den Sensorboxen an einer beliebigen Position aufgezeichnet und als Beobachtungen für das konstruierte mathematische Modell betrachtet.

Alle gemessenen Daten mussten zunächst verarbeitet und dann in einen Bestimmungsalgorithmus eingeführt werden, um den Ort des CR und die Schiffsbewegungen am CR zu schätzen. Basierend auf der Struktur der bekannten Informationen und den gewünschten Ergebnissen wird der Kalman-Filter angewandt, um das entsprechende mathematische Modell zu konstruieren. Darüber hinaus wird die Transformation zwischen relativen Koordinatensystemen durchgeführt und die gemessenen Bewegungsdaten einschließlich der zufälligen und systematischen Fehler werden ebenfalls verarbeitet. Die für die Transformation verwendeten Winkel werden durch einen Hochpassfilter und die Integration der gemessenen Winkelraten bestimmt. Dann wird die Transformation zwischen dem schiffskörperfesten System und dem horizontalen Inertialsystem mit diesen Winkeln zusammen mit dem zusätzlichen unbekannten Offset-Vektor erstellt. Der Offset, die untersuchte Variable in dieser Arbeit, ist definiert als der Abstand zwischen dem CR und dem Standort des Sensors in drei Dimensionen.

Die Ergebnisse zeigen, dass der Kalman-Filter angewendet werden kann, um die Position des CR eindeutig zu bestimmen. Diese Position hängt von den dynamischen Eigenschaften des Schiffes ab. Es wird auch festgestellt, dass es eine klare Abhängigkeit vom Anstellwinkel der einlaufenden Wellen gibt. Verschiedene Versuche zeigen, dass ähnliche Seegangsbedingungen zu ähnlichen Positionen der CR führen. Das CR trägt tatsächlich Informationen über den Seegang. Es wird gezeigt, dass bei geeigneter Signalaufbereitung auch preiswerte Sensorboxen eine ausreichende Datenqualität als Input für den Kalman-Filter liefern.

Contents

1 Introduction 14
  1.1 Background 14
  1.2 Research Questions 15
  1.3 Research Motivations 15
  1.4 Organization of Thesis 16
2 Determination of the Centre of Rotation 18
  2.1 CR Calculation for 2D and 3D Motion 18
    2.1.1 CR for Planar Motion 18
    2.1.2 CR for 3D Motions 20
  2.2 Introduction of Ship Motions 22
  2.3 Characteristics of Ship Motions 23
    2.3.1 1-DOF Motion 23
    2.3.2 3-DOF Motion 24
    2.3.3 4-DOF Motion 25
    2.3.4 6-DOF Motion 26
  2.4 CR of Ship Motions 26
    2.4.1 Research Problems 26
    2.4.2 Definition of Ship's CR 27
    2.4.3 Significance of Ship's CR 28
    2.4.4 Calculation Method of Ship's CR 29
3 Identification of the CR 31
  3.1 Studies on the CM, CG, CB, CF and PP 31
  3.2 Studies on the Identification of CR 33
  3.3 Measurement Devices 34
  3.4 Feasible Requirements of the CR 37
4 Methodology of CR Determination 39
  4.1 Description of the Measurement Units 39
    4.1.1 Sensor I 40
    4.1.2 Sensor II 40
  4.2 Measured Data Processing 40
    4.2.1 Process with Integrated Data 41
    4.2.2 Process with Differential Data 45
  4.3 Introduction of the CR's Determination Method 45
  4.4 Kalman Filter 46
    4.4.1 Introduction of Kalman Filter 46
    4.4.2 Euler Transformation 47
    4.4.3 Input Mathematical Model 49
  4.5 Simulation Results 51
    4.5.1 Estimated Results of Planar Motion 51
    4.5.2 Estimated Results from a Simulated Sea Environment System 55
5 Experimental Procedures 59
  5.1 Introduction of Ships 59
    5.1.1 Marvin 59
    5.1.2 Fathom 10 60

5.1.3 RV Simon Stevin 61
5.1.4 S. A. Agulhas II 61
5.1.5 Catamaran Willi 62
5.2 Experimental Conditions 63
5.2.1 Marvin at the Hunte River 64
5.2.2 Fathom 10 at Cape Town 64
5.2.3 Simon Stevin at Ostend 65
5.2.4 Agulhas II at Antarctic 66
5.2.5 Willi in the Manoeuvre Basin 67
5.2.6 Willi at the Yachthafen 68
6 Evaluation of the Results 70
6.1 Results of Marvin 70
6.1.1 Analyses of Several Trials 70
6.1.2 Analyses of the Complete Results 76
6.2 Results of Fathom 10 79
6.2.1 Analyses of the 2014 Results 79
6.2.2 Analyses of the 2015 Results 86
6.3 Result of Simon Stevin 95
6.3.1 Analyses of Several Trials 95
6.3.2 Analyses of the Complete Results 103
6.4 Results of Agulhas II 106
6.4.1 Analyses of Several Trials 107
6.4.2 Analyses of the Complete Results 114
6.5 Results of Catamaran Willi 117
6.5.1 Results in the Manoeuvre Basin 117
6.5.2 Results at the Yachthafen 119
7 Conclusion 128
7.1 Summary of Results and Conclusion 128
7.2 Future Work 131
Appendix 133
A Calculation of Motion Spectra from Wave Buoy Data 133

List of Symbols

CR	Center of Rotation
CG	Center of Gravity
CM	Center of Mass
CB	Center of Buoyance
CF	Center of Floatation
2D	Two Dimensions
3D	Three Dimensions
m	Meter
Hz	Hertz
kn	Knot
v_{ob}	Linear Velocity of an Object in a Plane
v_{CR}	Linear Velocity at Center of Rotation in a Plane
a_{CR}	Linear Acceleration at Center of Rotation
ω	Angular Rate in a Plane
a_{ob}	Linear Acceleration of an Object
d_{oc}	Distance between the CR and Object in a Plane
$\vec{a}_{ob}$	Linear Acceleration at an Object in 3D System
$\vec{a}_{CR}$	Linear Acceleration at CR in 3D System
$\vec{a}_1$	Linear Acceleration at Point 1 in 3D System
$\vec{a}_2$	Linear Acceleration at Point 2 in 3D System
$\vec{d}_{oc}$	Distance between an Object and CR in 3D System
$\vec{\omega}$	Angular Rate in 3D System
$\dot{\vec{\omega}}$	Angular Acceleration in 3D System
$\vec{d}_{oc1}$	Distance between Point 1 of an Object and CR in 3D System
$\vec{d}_{oc2}$	Distance between Point 2 of an Object and CR in 3D System
$\dot{\vec{d}}_{oc1}$	Derivative of Distance between Point 1 of an Object and CR in 3D System

$\dot{\vec{d}}_{oc2}$	Derivative of Distance between Point 2 of an Object and CR in 3D System
d	Distance between two random Points from an Object after rotating
d_0	Distance between two random Points from an Object when not rotating
R_M	Rotation Matrix in 3D System
$\vec{r}$	offset vector, $[r_x, \mathrm{r}_y, \mathrm{r}_z]^T$
r_x	Offset in x-direction
r_y	Offset in y-direction
r_z	Offset in z-direction
$\mathrm{O_eX_eY_eZ_e}$	Earth Coordinate System / Inertial Coordinate System
OXYZ	Ship Body-fixed Coordinate System
$\mathrm{O_sX_sY_sZ_s}$	Sensor Coordinate System
$\phi, \dot{\phi}, \ddot{\phi}$	Roll Angle, Roll Angular Rate, Roll Angular Acceleration
$\theta, \dot{\theta}, \ddot{\theta}$	Pitch Angle, Pitch Angular Rate, Pitch Angular Acceleration
$\psi, \dot{\psi}, \ddot{\psi}$	Yaw Angle, Yaw Angular Rate, Yaw Angular Acceleration
$R_{x,\phi}$	Rotation Matrix of Euler Angle ϕ, around x-axis
$R_{y,\theta}$	Rotation Matrix of Euler Angle θ, around y-axis
$R_{z,\psi}$	Rotation Matrix of Euler Angle ψ, around z-axis
R_b^n	Rotation Matrix from Ship Body-fixed Frame to Inertial Frame
v_b^n	Linear Velocity transformed from Ship Body-fixed Frame to Inertial Frame
a_b^n	Linear Acceleration transformed from Ship Body-fixed Frame to Inertial Frame
$\mathrm{v_b}$	Linear Velocity in Ship Body-fixed Frame
$\mathrm{a_b}$	Linear Acceleration in Ship Body-fixed Frame
L	Ship Overall Length
$\mathrm{L_{pp}}$	Ship Length between Perpendicular Lines
B	Ship Breadth
T	Ship Draft
D	Ship Displacement

V	Volume of displacement
v	Ship velocity
KG	Vertical Length, measured from Keel to the Center of Gravity
ICR	Instantaneous Center of Roll
D_M	Moulded Ship Depth
R	Vertical Coordinate of Ship Rotational Center
T_{LC}	Drought at midship for the considered Loading Condition
T_{SC}	Scantling Drought
x_k	State Vector at time k
x_{k-1}	State Vector at time k-1
u_k	Control Vector
z_k	Observation Vector
w_k	Process Noise
v_k	Observation Noise
Q_k	Process Noise Covariance
R_k	Observation Noise Covariance
F	Matrix of State Transition Model
H	Matrix of Observation Model
ax_s	Linear Acceleration in x-direction at Sensor
ay_s	Linear Acceleration in y-direction at Sensor
az_s	Linear Acceleration in z-direction at Sensor
ax_n	Linear Acceleration in x-direction at Center of Rotation in Inertial Frame
ay_n	Linear Acceleration in y-direction at Center of Rotation in Inertial Frame
az_n	Linear Acceleration in z-direction at Center of Rotation in Inertial Frame
ax_{off}	Linear Acceleration caused by Offset in x-direction
ay_{off}	Linear Acceleration caused by Offset in y-direction
az_{off}	Linear Acceleration caused by Offset in z-direction
Stb	Starboard

PSD	Power Spectrum Distribution
RAO	Response Amplitude Operator

List of Figures

Figure 1.1 CR of circular motion........ 14
Figure 1.2 CR of an object in 3D space........ 14
Figure 2.1 CR of circular motion - Pendulum........ 18
Figure 2.2 CR of 2D motion........ 19
Figure 2.3 CR of a triangle rotating in plane........ 20
Figure 2.4 Rotated object in 3D system........ 21
Figure 2.5 Earth coordinate system........ 22
Figure 2.6 Ship body-fixed coordinate system........ 23
Figure 4.1 Onboard sensor box........ 40
Figure 4.2 Original spectrum of the integrated angle........ 41
Figure 4.3 Spectrum of filtered integrated angle at f_c=0.1 Hz........ 42
Figure 4.4 Spectrum of filtered integrated angle at f_c=0.04 Hz........ 42
Figure 4.5 Spectrum of filtered integrated angle at f_c=0.03 Hz........ 43
Figure 4.6 Pwelch with nfft of 256........ 43
Figure 4.7 Pwelch with nfft of 1024........ 44
Figure 4.8 Pwelch with nfft of 2048........ 44
Figure 4.9 Spectrum of the angular acceleration at f_c=1 Hz........ 45
Figure 4.10 Kalman filter process........ 47
Figure 4.11 Euler transformation process........ 49
Figure 4.12 Result of KF distance when r is given as 0.2 m........ 52
Figure 4.13 Comparison of linear acceleration at CR when r = 0.2 m........ 52
Figure 4.14 Result of distance when r is given as 1.5 m........ 53
Figure 4.15 Comparison of linear acceleration at CR when r = 1.5 m........ 53
Figure 4.16 Result of KF distance when r is given as 3 m........ 54
Figure 4.17 Comparison of linear acceleration at CR when r = 3 m........ 54
Figure 4.18 Result of distance when r is given as 8 m........ 54
Figure 4.19 Comparison of linear acceleration at CR when r = 8 m........ 55
Figure 4.20 Description of floating vessel motion........ 56
Figure 4.21 Estimated offset of the first case [0;10]........ 57
Figure 4.22 Estimated offset of the second case [0;100]........ 57
Figure 4.23 Estimated offset of the third case [180;10]........ 57
Figure 4.24 Estimated offset of the fourth case [180;100]........ 58
Figure 5.1 Marvin........ 59
Figure 5.2 Fathom 10........ 60
Figure 5.3 RV Simon Stevin........ 61
Figure 5.4 Agulhas II........ 62
Figure 5.5 Willi in the basin........ 63
Figure 5.6 Description of Willi’s structure........ 63
Figure 5.7 Sensor onboard: inside the ship (left), on top of ship (right)........ 64
Figure 5.8 Sensor box on working desk........ 65
Figure 5.9 Sensor box onboard Fathom 10........ 65
Figure 5.10 Sensor box onboard Simon Stevin........ 66
Figure 5.11 Sensor box onboard Agulhas II........ 67
Figure 5.12 Sensor box on Willi........ 67
Figure 5.13 Willi in the manoeuvre basin........ 68
Figure 5.14 Willi at the Yachthafen........ 69
Figure 6.1 Estimated offsets of trial two........ 71
Figure 6.2 Estimated offsets of trial five........ 71

Figure 6.3 Estimated offsets of trial four 71
Figure 6.4 Estimated offsets of trial seven 72
Figure 6.5 Estimated offsets of trial nine 72
Figure 6.6 Estimated offsets of trial ten 73
Figure 6.7 Estimated offsets of trial eleven 73
Figure 6.8 Sea map at Cape Town 79
Figure 6.9 Relative sea state of trial four 80
Figure 6.10 Estimated offsets of trial four 80
Figure 6.11 Relative sea state of trial six 80
Figure 6.12 Estimated offsets of trial six 81
Figure 6.13 Relative sea state of trial seven 82
Figure 6.14 Estimated offsets of trial seven 83
Figure 6.15 Relative sea state of trial nine 83
Figure 6.16 Estimated offsets of trial nine 83
Figure 6.17 Normalization of the offset for Fathom 10 86
Figure 6.18 Relative sea state of trial thirty-one 87
Figure 6.19 Estimated offsets of trial thirty-one 87
Figure 6.20 Comparison of surge PSD of trial thirty-one 88
Figure 6.21 Comparison of heave PSD of trial thirty-one 88
Figure 6.22 Relative sea state of trial thirty-two 89
Figure 6.23 Estimated offsets of trial thirty-two 89
Figure 6.24 Comparison of surge PSD of trial thirty-two 89
Figure 6.25 Comparison of heave PSD of trial thirty-two 90
Figure 6.26 Relative sea state of trial thirty-four 90
Figure 6.27 Estimated offsets of trial thirty-four 91
Figure 6.28 Comparison of surge PSD of trial thirty-four 91
Figure 6.29 Comparison of heave PSD of trial thirty-four 92
Figure 6.30 Relative sea state of trial four 95
Figure 6.31 Estimated offsets of trial four 96
Figure 6.32 Relative sea state of trial twenty-one 96
Figure 6.33 Estimated offsets of trial twenty-one 96
Figure 6.34 Relative sea state of trial nine 98
Figure 6.35 Estimated offsets of trial nine 98
Figure 6.36 Relative sea state of trial eighteen 98
Figure 6.37 Estimated offsets of trial eighteen 99
Figure 6.38 Relative sea state of trial three 100
Figure 6.39 Estimated offsets of trial three 100
Figure 6.40 Relative sea state of trial seventeen 100
Figure 6.41 Estimated offsets of trial seventeen 101
Figure 6.42 Relative sea state of trial twenty-two 101
Figure 6.43 Estimated offsets of trial twenty-two 101
Figure 6.44 Relative sea state of trial twenty-four 102
Figure 6.45 Estimated offsets of trial twenty-four 102
Figure 6.46 Normalization of the offset for Simon Stevin 105
Figure 6.47 Lag of roll angular rates 106
Figure 6.48 Synchronized part for both sensors after down-sampling 107
Figure 6.49 Relative sea state of trials 28 and 121 108
Figure 6.50 Estimated offsets of trials 28 and 121 108
Figure 6.51 Relative sea state of trials 38 and 135 108
Figure 6.52 Estimated offsets of trials 38 and 135 109

Figure 6.53 Relative sea state of trials 43 and 145 111
Figure 6.54 Estimated offsets of trials 43 and 145 111
Figure 6.55 Relative sea state of trials 10 and 44 as well as 10 and 80 112
Figure 6.56 Estimated offsets of trial 10 and 44... 112
Figure 6.57 Estimated offsets of trials 10 and 80 113
Figure 6.58 Estimated offsets of trial three 118
Figure 6.59 Estimated offsets of trial four 118
Figure 6.60 Estimated offsets of case three.. 119
Figure 6.61 Estimated offsets of case seven... 120
Figure 6.62 Estimated offsets of case nine... 121
Figure 6.63 Estimated offsets of case ten... 121
Figure 6.64 Estimated offsets of case fifteen 122
Figure 6.65 Estimated offsets of case sixteen 122
Figure 6.66 Estimated offsets of case eighteen 123
Figure 6.67 Estimated offsets of case nineteen 124
Figure 6.68 Estimated offsets of case twenty-one 125
Figure 6.69 Normalization of the offset for Willi... 127
Figure A.0.1 Encounter frequency ω_e as a function of sea-state frequency $\boldsymbol{\omega f}$ 133

List of Tables

Table 5.1 Marvin loading conditions 60
Table 5.2 Fathom 10 loading conditions 60
Table 5.3 Simon Stevin loading conditions 61
Table 5.4 Agulhas II loading conditions 62
Table 6.1 Offsets results of Marvin 78
Table 6.2 CR results of Fathom 10 in 2014 85
Table 6.3 CR results of Fathom 10 in 2015 94
Table 6.4 CR results of Simon Stevin 104
Table 6.5 CR results of Agulhas II 117
Table 6.6 Offsets results of catamaran 126

1 Introduction

1.1 Background

When an object rotates in a plane, the point about which it rotates is called the centre of rotation (CR). With a clear tendency of motion, the location of the CR can be determined. For example, consider circular motion, as shown in Figure 1.1.

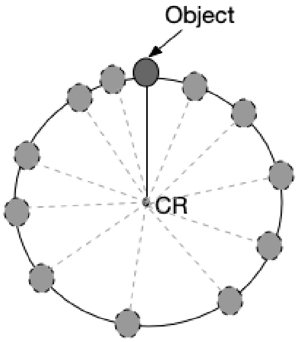

Figure 1.1 CR of circular motion

Expanding the analysis to a three-dimensional space, an object's motion is decomposed into three intersecting perpendicular directions, also known as axes. As shown in Figure 1.2, the original space is constructed with three axes (x_e, y_e, z_e), and three additional dashed axes are parallel to the original axes. The rotational system is (x, y, z) is generated by the object rotating around the fixed CR and with certain rotational angles in all three directions. Given the CR's location and the rotational angles, it is feasible to calculate the object's current motions in this original space.

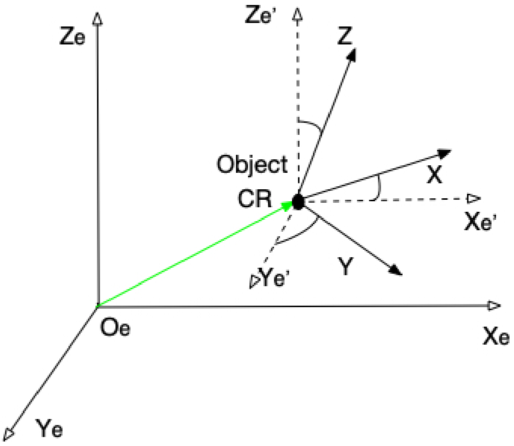

Figure 1.2 CR of an object in 3D space

In this work, the motion centre is regarded as the CR, which has a similar meaning to that of the CR mentioned in the previous part. Furthermore, the CR is also defined as the point about which all rotational motions have minor influences on all linear motions in this work, as illustrated in detail in Chapter 2.4. This definition is derived from the original physical explanation and characteristics of standard and relatively simple motions, such as circular motion. Depending upon the uneven distribution of the resultant forces or torques on the ship, the CR may not coincide with the centre of gravity (CG), as assumed in most recent research (Fermandes, 2016 [4]) (Costa, 2018 [5]) (Rogne, 2015 [6]). Moreover, under diverse external conditions, such as different encountered waves, there will be differences in the CR's relative positions for each particular condition. Determining the CR's location is much more complicated than for the CG, because the location of the CR is not expected to be directly observed.

When analysing the CR and its characteristics, another essential factor to consider is the distance between the CR and another point of interest, which would typically be the installation location of measurement devices. This distance is explicitly defined in this work as the offset. It is also a vector that can be resolved into three axes in a coordinate system. According to the circular theory, as mentioned previously, the offset contributes to the linear motions under the influence of a rigid body’s angular motions. Thus, the offset is vitally important to the study of the CR’s location and actual ship motions.

1.2 Research Questions

The location of a motion centre is not physically defined in ships and can’t be identified obviously. Besides, such a centre has many definitions which are described in chapter 3. Thus, the determination of this centre is complicated and fuzzy.

Regarding the CR defined in this work, the most significant question is its existence. If the CR doesn’t exist, what is exactly the motions’ centre? If the CR exists, how can we determine its location? Furthermore, since the motion’s centre is always regarded as the CG, is this CR coinciding with the CG, or other well-defined centres? And finally, how can the CR, namely the actual motions’ centre, affect the analysis of ship motions? Moreover, does this CR also have influence when analysing incident waves? These questions should be solved and discussed in this work.

1.3 Research Motivations

The centre of motion, which is regarded as the CR in this work, is an elementary parameter when studying rotational and related derived motions. Because ship motions are induced by the encountered waves, the motion centre is of significant interest to marine researchers and seafarers onboard when analysing and studying ship movement patterns and operating ships at sea. They are crucial to understanding ship behaviours, especially with respect to stability and safety. Furthermore, it is possible to make correct and timely decisions onboard based on these analyses.

Given the centre of motion, a better and more precise understanding of complicated and coupled ship motions can be achieved. Ship motions are only induced by the encountered waves without any extra contributions from measurement devices, which leads to the actual ship motions. Furthermore, according to the various CR locations, the distribution of the resultant force on the ship can be analysed to solve related physical problems.

The precise ship motion plays an essential role in ship applications, such as trajectory planning and dynamic positioning operations. Because waves induce ship motions, it is necessary to use precise motions to analyse and estimate the inducing waves. Furthermore, this would be beneficial for the development of the oceanic environment and related research. Nevertheless, obtaining precise motions is troublesome, because under most circumstances, measured data contain more than the ship motion information. Moreover, it seems to be a common problem that additional information concerning the distance between the sensor and the centre of motion is included in the measured data, and this additional distance will contribute to the ship motions as well. However, this problem is unavoidable because installing the measurement devices precisely at the point that describes the actual ship motions without any external disturbances is impossible under several conditions. For instance, it is difficult to place devices at the centre of motions when the required installation position is unreachable onboard. Moreover, large electrical devices may cover the ideal location, it may be inside the body structure, and so forth. Hence, this additional distance's contribution should be appropriately processed to obtain the actual ship motion data.

When implementing several sea trials, it is feasible to test and conclude the relationships between the CR and wave locations. Thus, CR location is no longer merely an abstract and intricate concept, but rather a practical point to help construct a more precise model for studies. Aided by the awareness of this relationship, the crew can have a clear and specific concept of the ship’s movements. In this way, they could be well-prepared for potential ship motions, execute timely operations to avoid certain hazardous behaviours such as capsizing, and maintain the ship’s stability and safety in a wide range of situations.

1.4 Organization of Thesis

The remainder of this thesis is organized as follows:

Chapter 2 starts with a basic introduction of a universal method to find the CR location for both planar and three-dimensional (3D) motions. Afterward, the complete conception of ship motions in three dimensions is addressed. According to the relationship between ship motions and waves, the contributions and problems caused by the CR are fully described. Thus, the initial thought about the determination of the ship's CR is presented.

Chapter 3 defines the current state of research, describing previous research on methods to confirm essential and diverse ship motion centres. The early and more recent studies on the development of definitions and how to determine the proposed CR are presented.

Chapter 4 describes the methodology used to resolve CR location. In the theoretical part, a mathematical model is constructed using the Kalman filter on the dependence of the measured sensor motion data structure and the knowledge of other noted contributing parameters. A simulation built in MATLAB Simulink is applied to test the Kalman filter's feasibility for both planar motion and ship motion. Finally, in the practical part, measurement devices and their generated motion data are presented.

Chapter 5 presents the experimental details, precisely illustrating the essential information of all the employed ships and the sea environment during the trial implementations. Moreover, the complete process of implementing all the trials is described.

The experimental results are evaluated in Chapter 6, including a discussion of the estimated results for the CR location obtained from all the applied ships. The errors acquired from both the estimated results and the Kalman filter process are evaluated to test the method's feasibility.

The final chapter concludes the thesis and offers a perspective on future work. It summarizes the conclusions obtained from the analyses of the estimated results and on-going discussions of existing problems. With respect to the unsolved problems, the expected further work is proposed to be finished in the near future.

2 Determination of the Centre of Rotation

As illustrated earlier, there are problems in determining the location of the CR during ship motions. Hence, a deeper understanding of the CR, its effects, and how they affect the ship motions is essential to solving these problems. In this chapter, an initial concept regarding finding the location of the CR is proposed:

1. A method to determine the CR's location for planar motion is depicted.
2. A complete description of a ship's motions in three dimensions is presented to obtain a comprehensive picture of its behaviours in the water.
3. A few related combinations of ship motions are depicted to clarify the connections among them. Next, the consequences imposed by the CR are discussed, that is, the creation of additional linear motions.
4. Based on the consequences, apart from the physical meaning, a more mathematical definition of CR is proposed.

2.1 CR Calculation for 2D and 3D Motion

According to the physical definition of the CR, it is feasible to determine the CR's location mathematically for either planar or spatial motion. Once the location is determined, a clear understanding of the motion is achieved.

2.1.1 CR for Planar Motion

As illustrated in Chapter 1.1, the CR for a complete circle motion is centre of the circle. For example, when an object swings like a pendulum, as shown in Figure 2.1, the CR is located at the marked upper point, and the linear velocity of this object can be calculated by the linear velocity of the CR and the angular motion.

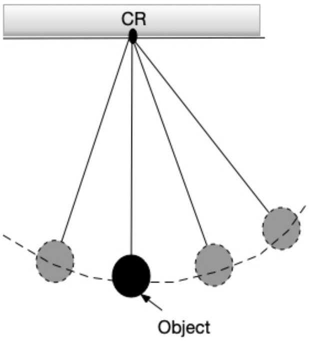

Figure 2.1 CR of circular motion - Pendulum

The linear velocity of the CR and an object in a plane are expressed as v_{CR} and v_{ob}, respectively, the distance between them is d_{oc}, and the angular rate for this rigid body is ω. Therefore, the relationship between these two points with respect to their linear velocities is shown in Equation 1. The difference in linear velocity between these two points is given by the product of the angular rate and the distance between them.

$$v_{ob} = v_{CR} + \omega * d_{oc} \quad (1)$$

Based on the relationship between the acceleration and velocity, it is possible to calculate the linear acceleration of the object. As shown in Figure 2.2, at the CR, the linear acceleration is a_{CR}. For planar motion, d_{oc} is a scalar. At the object, the angular rate ω is identical and the linear acceleration is a_{ob}, which can be obtained by differentiating Equation 1 with respect to time. That is,

$$a_{ob} = a_{CR} + \dot{\omega} * d_{oc} \quad (2)$$

where $\dot{\omega}$ is the angular acceleration, which is the time-derivative of the angular rate ω. Given a_{ob} and ω, the desired variables a_{CR} and d_{oc} can be acquired from this relatively straightforward expression of Equation 2.

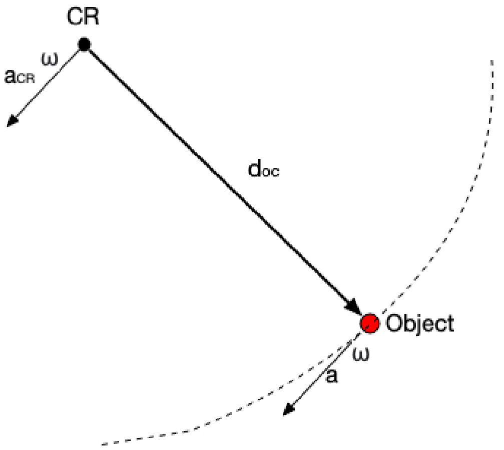

Figure 2.2 CR of 2D motion

Another example is shown in Figure 2.3. Typically, an object can rotate around one fixed point through any angle. This fixed point is regarded as the CR, and in this case, the object rotates through 90°. The dashed lines determine the location of the CR. The dashed lines are grouped into two categories. Those in the first category indicate the distance between the triangle's original points and the CR, whereas those in the second show the distance between the rotated points and the CR. For each point of the triangle, the two corresponding lines are of equal length and have been illustrated in the same colour. Moreover, the same-coloured lines intersect at right angles [1]. The location of the CR determines the characteristics of a particular motion, as illustrated by the examples of planar motions described here. Based on the knowledge of these motions, either rotational or linear motions can be derived.

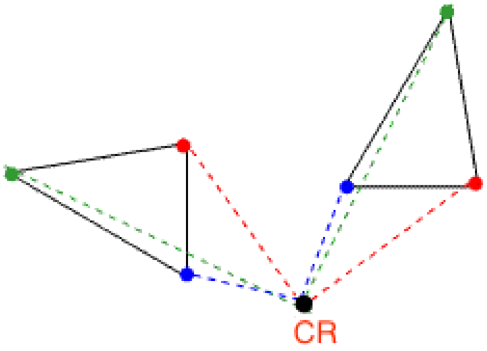

Figure 2.3 CR of a triangle rotating in plane

2.1.2 CR for 3D Motions

An object moving in space has certain features, such as its size and shape. These features should be considered when studying motions because they are related to the object's deformation (Decaudin, 1996 [2]). Therefore, a common assumption adopted for objects is to regard them as rigid bodies.

In physics, a rigid body is also known as a solid body, which exhibits zero or minimal deformation that can be neglected. The distance between any two points on the body remains constant, regardless of external forces. Linear and angular motions in rigid body kinematics may be considered in terms of positions, velocities, and accelerations. The position of a body can be represented as a vector in space for a linear motion, which is also the origin of a defined coordinate system fixed to the body; linear velocities and accelerations can be represented similarly. In the case of purely translational motions, all points on the rigid body have the same linear velocity. However, when rotational motions are involved, every point on the body exhibits the same angular rate. In this case, the linear velocities of any two points are different, owing to the contributions of the distances between them (Ault, 2021 [3]).

When studying motions in three dimensions, the linear velocities and angular rates as described in the first chapter are vectors with three components at any point in the object. When deriving the linear acceleration, that is the differential of the linear velocity in the time domain, the expression is similar to Equation 2, but all the parameters are vectors:

$$\vec{a}_{ob} = \vec{a}_{CR} + \dot{\vec{\omega}} \times \vec{d}_{oc} + \vec{\omega} \times (\vec{\omega} \times \vec{d}_{oc}) \quad (3)$$

where $\dot{\vec{\omega}}$ is the angular acceleration vector.

One method is to select two random points from the object when it moves in a given space, such that the linear accelerations of both points can be calculated by Equation 3:

$$\vec{a}_1 = \vec{a}_{CR} + \dot{\vec{\omega}} \times \vec{d}_{oc1} + \vec{\omega} \times \dot{\vec{d}}_{oc1} \ (4)$$

$$\vec{a}_2 = \vec{a}_{CR} + \dot{\vec{\omega}} \times \vec{d}_{oc2} + \vec{\omega} \times \dot{\vec{d}}_{oc2} (5)$$

$$\vec{d}_{oc2} = \vec{d}_{oc1} + \vec{d} \ (6)$$

where $\vec{a}_1$ and $\vec{a}_2$ are the linear acceleration vectors of these points, $\vec{d}_{oc1}$and $\vec{d}_{oc2}$ are the distances between each point and the CR, $\dot{\vec{d}}_{oc1}$ and $\dot{\vec{d}}_{oc2}$ are the time-derivatives of the distances, and $\vec{a}_{CR}$ is the linear acceleration vector at the CR. As the object is regarded as a rigid body, the angular rate $\vec{\omega}$ recorded at any point in the object is identical. $\dot{\vec{\omega}}$ is the angular acceleration obtained by differentiating $\vec{\omega}$. $\vec{d}$ is the known distance between the two points, which is constant in the object.

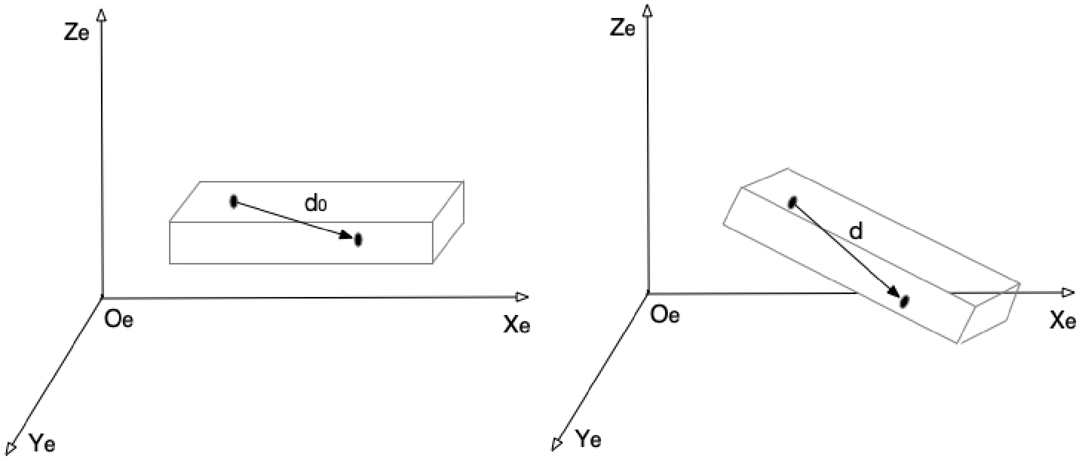

Figure 2.4 Rotated object in 3D system

However, in the given space, considering the relative position of these two points besides the object's body-fixed frame, this distance changes when rotational motions occur in the coordinate system $\{O_e, (X_e, Y_e, Z_e)\}$, as shown in Figure 2.4. Thus, it is necessary to introduce a rotation matrix when calculating the CR's location from Equations 4 and 5. Thus, $\vec{d}$ is recalculated from the distance in the initial position $\vec{d}_0$ and the rotation matrix R_M, as shown in Equation 7.

$$\vec{d} = R_M * \vec{d}_0 \ (7)$$

where R_M is time-dependent and contains the rotation angles. Finally, the expression for $\vec{a}_2$ can be rewritten as

$$\vec{a}_2 = \vec{a}_{CR} + \dot{\vec{\omega}} \times \vec{d}_{oc1} + \vec{\omega} \times \dot{\vec{d}}_{oc1} + \dot{\vec{\omega}} \times (\mathrm{R}_M * \vec{d}_0) + \vec{\omega} \times (\dot{R}_M * \vec{d}_0) \ (8)$$

Thus, by considering Equations 4 and 8, it is possible to calculate the variables $\vec{a}_{CR}$ and $\vec{d}_{oc1}$ using known parameters $\vec{a}_1$, $\vec{a}_2$, R_M, and $\vec{d}_0$. However, the motions of at least two points are required for this method.

2.2 Introduction of Ship Motions

Oscillating ship motions are the resultant movements caused by the combined action of different wave systems. One kind of wave is influenced by the wind, also known as the wind sea. The other is the swell, which is affected by waves generated by local wind in a specific location and impacted by a distant storm (Triantafyllou, 1981 [7]). These effects cause oscillating motions in six degrees of freedom (DOFs), which can be sorted into two main categories: translational and rotational motions.

Usually, when describing the motions of ships or vessels in six DOFs, it is convenient to establish a combination of two related coordinate systems as illustrated in Fossen (2011 [8]). One is called the earth-fixed coordinate system, and because vessels or ships have a relatively low velocity with respect to the angular rate of this coordinate system, the earth's rotation can be neglected and assumed to be inertial; hence, this frame is also known as the inertial coordinate system. With the origin at the centre of the earth, the vertical axis, z_e, points upward to the north, the transverse axis, y_e, points to the east, and the longitudinal axis, x_e, satisfies the right-handed rule, as shown in Figure 2.5; this is a widely used coordinate system in the fields of global guidance, navigation, and vessel motion control.

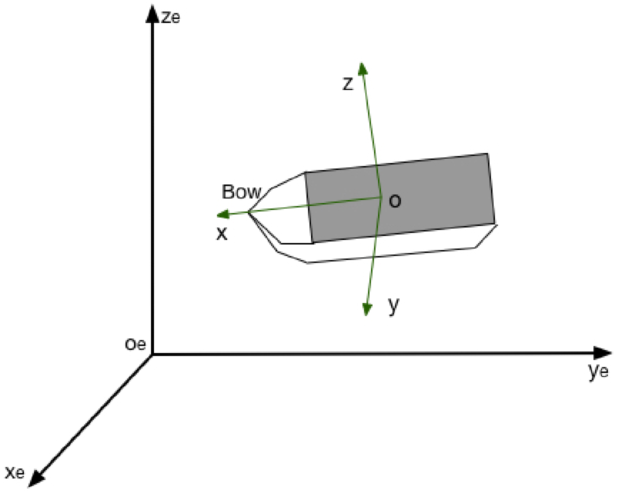

Figure 2.5 Earth coordinate system

The other coordinate system is called the ship body-fixed coordinate system. As shown in Figure 2.6, this coordinate system's origin is typically on the line formed by midships crossing the waterline. In practical applications, the origin is typically assumed to be the CG, such that an apparent physical characteristic can be used to determine it precisely and further simplify the related scientific work. This coordinate system is also made up of three axes, the longitudinal axis, *x*, transverse axis, *y*, and vertical axis, *z*, and it obeys right-handed Cartesian rule as well. The ship's longitudinal movement is named surge, and the positive direction points to the bow. The transverse movement is defined as sway, and the positive direction is towards the portside. Movement in the vertical direction is known as heave and the positive direction is upward. Finally, these three movements consist of the translational ship motions. The rotational movement related to the ship's behaviour is defined in three dimensions: roll is the rotation around the x-axis, pitch is the rotation around the y-axis, and yaw is the rotation around the z-axis.

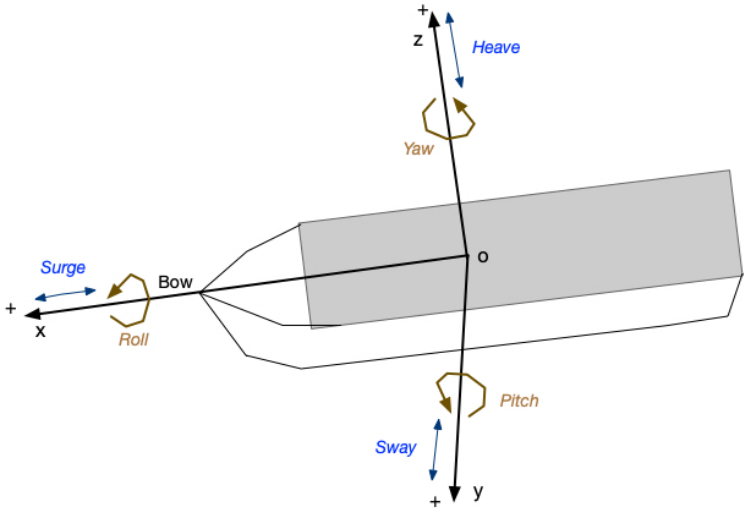

Figure 2.6 Ship body-fixed coordinate system

2.3 Characteristics of Ship Motions

Research on all dimensions of ship motions is the primary interest for analysing and designing ship motions in simulations and realistic sea environments. However, running numerical simulations of the entire six DOFs of motions would be significantly time-consuming. Along with constructing complicated mathematical models, a series of related parameters are required, and non-linear relationships are also involved. Therefore, to obtain efficient results, reductions of the multi-DOF state space are considered for certain specific circumstances and applications, thereby avoiding nonessential calculations.

2.3.1 1-DOF Motion

Suppose only one DOF motion is to be described. In that case, there must be an explicit and unique purpose, which could be a surprising approximation for a complex study. Typically, a specific motion does not occur alone; although we endeavour to avoid or decrease the effects of coupling among motions, they still affect each other. Therefore, a motion should be the most essential for a task when concentrating on only one specific motion. Meanwhile, it has an evidently larger amplitude compared with other motions.

Surge describes the forward ship motion, and the bow of the ship rises or dips when encountering strong waves. On the one hand, when trying to analyse the effect of the forward speed of the ship's behaviour, surge motion is the primary factor to be studied. It is usually superimposed on steady propulsive motion. On the other hand, a moored ship at the dock requires slight movements, and requirements on the amplitude of surge motion are quite critical, especially in the process of loading and unloading (Bont, 2010 [9]).

Heave motion is the most troublesome and must be compensated for a particular sea state for vertical motion analysis. It is related to many problems, such as seismic experiments for oil exploration, control of remotely operated vehicles, underwater target tracing, and float wave data analysis (Yang, 2009 [10]), as well as many specific marine applications for vertical motion, such as subsea lifting operations (Küchler, 2011 [11]) and safe aircraft landing on the vessels (Marconi, 2002 [12]).

Roll motion can strongly affect the ability of vessels or ships. With severe and excessive roll motion, the probability of the crew's seasickness increases, the operability of the onboard systems decreases, and the worst-case scenario is the vessel capsizing. Cargo may fall overboard, leading to massive economic loss and damage (Ivče, 2010 [13]). Hence, approaching roll motion alone and constructing its dynamic system will help to analyse roll motion and avoid unnecessary problems and loss.

Yaw describes the course of the vessel. However, it would have a drastic change when the ship is overtaken by waves, affecting the course's stability. The basic principle of moving the rudder to the desired angle when steering the ship is to regulate the appropriate yaw motion (Nicolau, 2003 [14]), and thus it is the primary part for feedback control when designing ship autopilots.

2.3.2 3-DOF Motion

Usually, ship motions are coupled with each other. One-DOF motion cannot describe this complexity and express the ship's behaviour in detail. Therefore, adopting several DOFs is a better way to study ship motion and waves. Combinations of three motions are most commonly used for several specific research areas.

Roll, pitch, and heave motions can cause discomfort to humans, and they are always treated as harmonic oscillations. It is well known that a ship's response can be strongly affected by the coupling relation between roll and pitch motion in waves. Meanwhile, a coupling effect between roll and heave leads to buoyance and moment lever change. The energy in heave and pitch can transfer to roll motion through non-linear coupling, resulting in excessive rolling problems (Ibrahim, 2009 [15]). These three motions can be determined during a standard seakeeping test for a ship.

Horizontal plane models, including surge, sway, and yaw motion, are frequently used in trajectory-tracking control, dynamic positioning, and path-following systems. All these three motions should be considered, such that even with constant forward speed and manoeuvring in oblique waves, analysing or investigating wave-induced forces and motion moment is feasible (Wicaksono, 2018 [16]).

Under the assumption that a ship can be divided into symmetric parts by the X–Z vertical plane, namely dividing it by lateral symmetry in shape and weight distribution, the six DOFs can be separated into two sets. One set consists of the lateral motions, sway, roll, and yaw. There will be a remarkable coupling between roll and yaw motions, such that with restricted yaw motion, roll motion can reach its maximum. When considering the forward speed, a linear approximation analysing roll motion is not sufficiently precise, and therefore yaw and sway motion coupling is introduced to illustrate ship motions, especially when focusing on capsizing problems (Das, 2006 [17]). Moreover, this combination can also be applied to aspects of turning and heading control with yaw motion regulation.

The other set consists of surge, heave, and pitch motions, establishing the longitudinal models of ships. When a ship has excessive longitudinal accelerations or strong longitudinal moments, which results in larger heave and pitch motion, it will significantly affect navigation performance (Zhang, 2019 [18]). This combination is also specifically applied when a ship advances with a constant forward speed, vessel diving and pitch control.

2.3.3 4-DOF Motion

The assembly of roll, pitch, heave, and surge motions is mainly still concerned with the roll motion. It avoids larger amplitude of roll angle, ship capsizing, and seasickness by introducing non-linear factors and increasing oscillation amplitudes. It is usually formed by adding surge motion to the model consisting of roll, pitch, and heave, and it primarily focuses on the condition in which the ship is advancing with a forward speed.

A numerical model consisting of four DOFs of surge, sway, roll, and yaw motions has been utilized to prevent capsizing of a ship in recent research work, especially for a vessel that is under the following and quartering seas with high forward speed (Umeda, 2002 [19]). With the non-linear dynamic model generated by this 4-DOF ship motion combination, applying optimal control algorithms eliminates undesired and irregular ship movement (Maki, 2009 [20]).

2.3.4 6-DOF Motion

A full six-DOF model contains all the described ship motions, considering all influences from the external forces, hydrodynamic forces, hydrostatic forces. All the linear and non-linear factors are included. This complete model is normally implemented in the construction of the ship's simulation. Afterwards, naval training can be applied into practice with this type of full-scale simulation, along with certain computer games containing maritime scenarios and backgrounds, possibly also including naval contents (Ueng, 2008 [21]) (Wooley, 2009 [22]). Moreover, the complete six-DOF motion simulation can also be applied to ship hull design. Simulations are essential tools for marine education (Ergum, 2009 [23]) (Sandaruwan, 2010 [24]).

On the research aspect, it is well known that this full six-DOF motion demands excessive computing resources, massive numerical calculations, and enormous expense. With computer science development, complicated calculations are no longer the most challenging problems for research. Novel techniques in this era can perform calculations with the full six-DOF model; this model has already been widely used for the prediction of coupled ship motion, and has also been applied in control system design for ships and underwater vehicles (Fossen, 2011 [8]) (Ayaz, 2003 [25]) (Giron-Sierra, 2004 [26]).

2.4 CR of Ship Motions

After describing all kinds of ship motions, study on ship's CR is essential and beneficial when analysing ship motions. Hence, the basic definition and significance of CR are addressed in this part, and the potential problems when studying on the CR is also proposed.

2.4.1 Research Problems

When studying the motions of a complex system such as a ship in three dimensions, the location of a CR is usually not entirely evident and convenient to determine. In practice, motions have their respective centres and are mutually coupled. However, there is still a doubt as to whether those centres would coincide with a specific centre or not. Thus, trying to study all motions and summarize their tendencies together would become a challenging task. If a CR can be detected, then its location would vary based on complicated resultant influences of the ship's motions.

There is no doubt that the CR is caused by the motions, while the motions have several different patterns. On the one aspect, when regarding the ship as an entire object such as the small ball shown in the figures above, the ship undergoes simple and straightforward circular motion, and it is clear to determine the location of the CR. On the other aspect, when a ship is floating in the sea, its motions are caused by waves or its propulsion system, or even both, and are no longer simple. One type of motion description is not sufficient to depict the ship's behaviour accurately. Furthermore, the ship would be affected by the resultant of all forces, such as hydrostatic and hydrodynamic forces, which are made by the sea environment, and occasionally including forces caused by the manoeuvring or controlling operations. All those complicated motions lead to difficulty in determining the location of the CR.

Apart from the ship itself, another factor that could affect the CR's location should also be considered, regarding the measurement devices onboard. Motion data measured from devices concern the motions at the point where the devices are placed. Therefore, they cannot be directly utilized as the ship motions because they are in the sensor's inherent frame, and the motion's centre is not the ship motion's centre. Hence, a method to transfer all those data into the ship body frame or earth frame is necessary. The distance between the measurement devices and the CR is included in the meantime. When the ship moves, this distance and the corresponding rotational motion introduce additional linear motion effects based on simple circular motion.

2.4.2 Definition of Ship's CR

The CR is commonly defined by the physical significance, as the rotational centre can be expressed and shown in many aspects, as shown in Figures 1.1, 2.1, and 2.3. In some cases, it is easily discovered. For example, a pendulum swings back and forth, undergoing circular motion, and it is apparent that the CR is located at the upper fixed point, which is the centre of the circle. For planar motions, the centre is easily identifiable when the motion tendency is clear.

However, in complex and integrated systems such as ships, the location of the CR cannot be distinguished during various motions caused by forces when the ship is under various external environments. The resultant forces are unevenly distributed along the ship, leading to different ship movement patterns, and the CR's location is no longer fixed. Hence, the elementary physical definition is certainly insufficient in such cases to determine the position of CR.

In this work, the CR is regarded as the point about which wave-induced linear motions and rotational motions are moving. Thus, both linear and rotational motions occur here. The rotational motions at the CR are the same as at other points in the ship. Furthermore, the correlation between the linear motions and the rotational motions is the least at the CR. Because of the characteristics of ship motions, the CR's location is not constant, and it changes under different motions.

Moreover, at this point, there is no additional information apart from ship motions; for instance, the additional resultant factors caused by the measured and recorded data, onboard staff, or installed devices. These are undesired or unexpected and should not be measured or detected at the CR. Both definitions are important and helpful to study for the relevant ship’s research.

During sea trials, ship motions would be recorded by specific measurement devices. Therefore, the contributing distance between points is the distance between the actual sensor's installed location and the CR, which is introduced and nominated as the offset. Thus, this offset is a vector and affects the linear ship motions simultaneously. Using the offset, it is feasible to construct the connection between the measured motion data and the wave-induced ship motions, because the measured data produced by the devices onboard indeed contain much of the expected and desired information about ship motions to determine the CR's location. The next steps are to summarize this relationship's theoretical expression with respect to the motion data, the offset, the ship itself, and the encountered waves; to find out an appropriate method or algorithm and realize this relationship in practice; and finally, to calculate the expected location of the CR.

2.4.3 Significance of Ship’s CR

Considering the structure and relationships among the translational and rotational motions of a ship, constructing an appropriate coordinate system is essential. Furthermore, determining an appropriate reference point, that is, the origin of this coordinate system, and also regarded as the centre of all the induced wave motions in this work, is vital. This centre can precisely and thoroughly describe the motions' relationships when describing the complete ship motions. Furthermore, the ship’s motion centre does not simply depend on the ship itself, but it can also be strongly affected by the distribution of the resultant forces.

Moreover, when studying ship motions, the assumption regarding the complete ship body as a rigid body is widely applied. By adopting this assumption, rigid body kinematics may be applied to generate a clear and straightforward scene when studying complicated ship motions.

However, the actual point around which motions occur, defined as the CR in this work, is rarely studied directly. In many previous studies, the CG is generally regarded as the point among all ship motions and further as the origin of the ship body-fixed coordinate system. Alternatively, the pivot point (PP) definition has been introduced to describe ship motions, primarily during operation. Nevertheless, in real sea states, it is not precisely true that the ship moves around the CG or PP; rather, they are approximated or empirical points around which the ship moves, in consideration of the convenience to construct simulated models and analyse wave characteristics.

Studying the CR has played an essential role in analysing ship's behaviour properly and estimating the precise wave characteristics. Therefore, determining the exact location of the CR is urgent and expected. For example, it is not easy to reach the centre or the point of interest, owing to ships' various structures. To be more specific, during the installation of measurement devices onboard, the ideal installation location may be covered by wires or hidden behind bulky electric equipment, or in some other unreachable location. Thus, this distance between the ideal location (that is, the location of the CR described in this work) and the measurement devices' actual location, which is defined as the offset in three dimensions, is included in the measured motion data. The offset information must be separated from the motion data to acquire the actual and pure motions at the CR, which could help to analyse the ship's behaviour in a real sea environment. Furthermore, when locating the CR is possible, there will be fewer limitations when installing measurement devices onboard and the required preparation time will be significantly reduced owing to the known offset.

Once the CR location is determined, the implementation of several research avenues becomes feasible, such as constructing reference coordinate systems and calculating the corresponding distances about the floatation or metacentre. Because all motions act around the CR, it is convenient to ascertain the CR as the original point when establishing reference coordinate systems. Motions would be symmetric and regular in this coordinate system, leading to lucubrating the ship's behaviour. Thus, constructing complete mathematical models to describe ship motions will be explicit and straightforward. At the CR, the ship motions are supposed to be purely induced by encountered waves. Thus, it is suitable for enhanced prediction of the ship's subsequent behaviour with this pure motion data. Moreover, it is helpful to estimate the current wave characteristics more precisely, without extra disturbing factors, and could be another way of recording sea state.

2.4.4 Calculation Method of Ship's CR

In actual sea trials, ship motions are induced by encountered waves and local wind, making all motions related, coupled, and continuous. Thus, it is difficult to determine the CR's location by an isolated and dependent sampling point acquired from measurement devices. Instead, the complete or selected motion process in a time series should be adopted to predict the location or range of the CR.

A widely used assumption regarding a ship as a rigid body is essential to establish a reasonable and appropriate mathematical model for studying ship motions. The related kinematics can be applied to ship motions. According to the characteristics of a rigid body, the angular rates at any point in the ship body should be identical. Furthermore, the linear velocities or accelerations are different at every point in a ship, owing to derivatives from angular rates and the distances between points. Similar expressions about these derivatives can be addressed for ship motion, as shown in Equation 3.

Typically, the given motion information of a ship is supported by several measurement devices onboard, such as sensor boxes equipped with accelerometers and gyros. Thus, the ship's linear accelerations and rotational rates are obtained in a time sequence. Based on the pattern of rigid body motion, when a sensor box is operating in the ship, the relationship between it and the CR with respect to the linear acceleration is expressed in Equation 9.

$$\vec{a}_s = \vec{a}_{CR} + \dot{\vec{\omega}} \times \vec{r} + \vec{\omega} \times (\vec{\omega} \times \vec{r}) \quad (9)$$

where $\vec{a}_s$ is the linear acceleration acquired from the sensor box and $\vec{r}$ is the offset vector as defined in Chapter 2.4.2.

One possible way to determine the location of a ship's CR is to utilize the calculation in 3D motion, as illustrated in Chapter 2.1.2. Therefore, at least two sensor boxes are required for this method. The advantage of using this method, as expressed from Equation 4 to Equation 8, is the avoidance of the ship's parameters and wave information. As long as the sensor boxes are operating, the ship motion information is obtained, and thus it is convenient to calculate the CR's location. However, the restriction on the number of sensor boxes renders this method inapplicable under some circumstances.

Therefore, a more feasible method is necessary to determine the CR's location that combines the given physical definitions and the mathematical method. It should have no requirements on the measurement devices' employment, avoid excessive prior knowledge of ships' parameters, and deal with a series of motion data in the time domain. Based on the structure of Equation 9, all components are described in space, and there is a relationship between the linear accelerations at the CR and sensor. Therefore, instead of solving this equation directly, several algorithms can be applied to solve this problem without adding another measurement device. For example, optimal algorithms can deal with issues presenting limitations or restrictions; moreover, the Kalman filter is an algorithm that is specialized in dealing with problems in space and is very suitable to the present work.

3 Identification of the CR

In the majority of research studies, instead of studying the CR, the CG, centre of mass (CM), centre of floatation (CF), centre of buoyance (CB) and pivot point (PP) have more commonly appeared, the related definitions of these centres are fully described in chapter 3.1. These five centres have advantages over the CR, specifically with respect to their explicit physical definitions. Under most circumstances, the CR seems to be an abstract and imaginary point, without any apparent connections to these practical centres. Therefore, it is convenient to concentrate on other centres to analyse wave-induced ship motions, and it is much easier to establish the mathematical models according to their physical meanings.

In this chapter, the study of ship motions using related centres is described, and then the more accurate and appropriate point to describe all ship motions is introduced, namely the CR, after which the concomitant problems when focusing on the CR are discussed. Finally, the current widely applied measurement devices onboard are depicted to determine which one would be more efficient and appropriate to install on the ship when analysing ship motions, and would also be convenient and straightforward to employ for the crew and other researchers, thus reducing the effort and time required to place devices and prepare experiments in real-world scenarios.

3.1 Studies on the CM, CG, CB, CF and PP

When studying ship motions, the gravitational field surrounding the ship is supposed to be uniform, such that the CM coincides with the CG [27], and thus it is possible to use certain numerical methods to calculate this type of geometric centre.

Most recent research works have revealed that a common strategy to study ship motions is to regard the CG as the complete centre of motions. Because the stability is affected partly by the ship's weight distribution and the hull itself, to be more specific, the continuous reduction in fuel and changeable water weight will affect a ship’s trim performance, and then a change in the floatation occurs (Krate, 2013 [28]). Thus, it is convenient and logical to regard the CG as the centre of motions, which can easily be illustrated, explained, and calculated in physics, so as to reduce superfluous computations (Hu, 2013 [29]) (Bryne, 2016 [30]) (Lee, 2016 [31]). The CG is regarded as the origin of described and desired frames, such as the ship-body frame or measurement frame. Usually, the location of the CG is treated as a fixed point with a few assumptions. It would be easier to determine, especially on model ships (Lee, 2002 [32]).

There are some commercial software packages such as SEAWAY (Journée, 2003 [33], 2001 [34]) and PDSTRIP (Söding, 2006 [35]), which use the CG as their reference original point in the existing coordinate system. The distance between the CG and the ship's keel has played an essential role in the calculation process. Such applications require more and more accuracy on the location of CG with the technological advances and broadening feasibility. The influence of the CG on static and dynamic ship characteristics is significant under certain circumstances, which can manipulate the ship's performance. For example, roll motion is very sensitive to the ship's loading, which causes the movement of the CG or CM, and in the worst case can cause the collapse of the ship (Fossen, 2011 [8]) (Tannuri, 2003 [36]). Under heave and pitch motions, the ship moves up and down in the waves, which also causes a shift in the CG, and with larger-amplitude motions, there is an increased probability of the ship capsizing.

The CB is defined as the geometric centre of the ship’s underwater hull body, and it is the point at which all buoyance forces are considered to act vertically upward. When the ship heels in small angles (less than 10°), the CB moves up or down based on the change in the water line (Chiotoroiu, 2015 [37]) (Schneekluth, 1998 [38]).

The CF is the centre of the ship's waterline area, and the ship trims about this point. As the waterplane area changes, the CF's position moves accordingly, slightly closer or farther from to the aft perpendicular. Usually, the CF's change curve is given in the stability booklet as the ship starts to run. Otherwise, the CF is approximately regarded as the point at which the middle perpendicular intersects with the waterplane. The traditional method to determine the CF's location is to use pitch motion by computing its maxima and minima. Nowadays, using a combination of motion sensors and cameras to record accelerations has become universal. A mathematical model was constructed on the basis of a point's accelerations rotating in a particular coordinate system (Abankwa, 2018 [39]). Both the CB and CF have a strong relationship with the metacentre, which is also utilized as the centre of ship motions. A previous study (Herder, 2004 [40]) found that rotational motion coincides with the metacentre.

Another widely adopted motion centre is the PP, as described in previous studies (Butuşină, 2012 [41][42]). The PP is defined as the centre around which the ship rotates when turning. This centre is located approximately one-third of the ship's length from the bow when the ship is moving forward, and at one-quarter of the ship's length from the stern when the ship is moving backward. Many experiments and sea trials have shown that the PP's position is also related to the currents, resultant forces, the ship itself, and other factors. Therefore, researchers are increasingly working to revise the traditional fuzzy definition of the PP in a more mathematically rigorous way (Capt. Cauvier, 2008 [43]) (Seo, 2016 [44]). Because it is essential in ship handling and necessary to seafarers, they are taught to understand the pattern of ship motions based on this point.

3.2 Studies on the Identification of CR

Although there are many research studies on different types of centres, the most suitable centre to describe wave-induced ship motions is the CR. The other centres are only substitutes, favoured for the easier confirmation of their locations and more straightforward subsequent computations. However, the centres' information is primarily ascertained during the design and recorded in the stability booklet when ships are newly built. As time passes, the ship's initial parameters change, such that the location of the centres changes as well. Moreover, not every ship has maintained its stability booklet. Many of them may be lost or accidentally destroyed, such that finding the information about the centres may be impossible. Hence, using mathematical or experimental methodologies with ships' parameters to determine the centres is necessary and imperative.

Regarding the CR's fundamental physical definition, it is the point around which all motions move, and it does not move along with the motions. In a simple rotational system, this point is primarily consistent with the CG. However, this is not always the case on a ship or a vessel, because these are complicated combinations of the body structures, installed equipment, staff deployment, and the resultant influence of the external factors such as waves and wind. Therefore, the static situation's location information is not accurately applied in the dynamic sea environment. As shown in recent studies, the location information based only on the preliminary stability characteristics can no longer meet the increasing expectations. Thus, mathematical or parametric methods to determine the location of centres have been proposed to obtain precise information of the locations (Abankwa, 2018 [39]) (Karolius, 2018 [45]).

The first study about the centre of motion can be traced back to the nineteenth century, in the work of Froude, which focused on the roll motion and proposed the related resultant influences of successive waves (Froude, 1861 [46]). Afterward, a more numerical method was proposed, which summarized the possible causes of larger-amplitude roll motion. In this case, the CR of roll motion would be located at the mean water surface (Chen, 2001 [47]). Nowadays, people who study the centre of roll motion believe that the instantaneous centre of roll (ICR) location depends on the wave frequencies and is linearly distributed, and that the ICR may not remain between the CG and CB and be a fixed point (Fernandes, 2016 [48]). In the study of Costa (2018 [49]), a tracking system was built with cameras to record motions, and with the help of calculated ship parameters, a similar centre of the pitch motion has been identified. In studying multi-motions, based on Archimedes' principle, the CR can be regarded as the application point of the resultant force on the ship, where the resultant force is defined as the combination of hydrostatic forces applied to the waterplane of a ship (Kliava, 2010 [50]). Considering angular momenta, the summary of the torques should be zero at the CR (Techet, 2004 [51]). When judging from experience, the CR would generally be located at one-third of the ship's length from the bow, and it will change its position according to the various waves' characteristics. Some researchers believe that the CR is at the centre of lateral resistance; in their work, it is referred to as the leaning point for arm levers (Capt. Cauvier, 2008 [43]) (Jeong, 2012 [52]) (Carreño, 2012 [53]) (Perera, 2015 [54]).

However, under different assumptions, the CR is replaced by the CG, CF, metacentre, or PP, and hence the actual study of the CR's confirmation is ignored. In this work, the clear location of the CR is depicted, as well as the methodology to determine it. An equation to calculate the vertical position of the CR was proposed by the DNV GL in the rules for the classification of ships (DNV GL, 2020 [55]), as shown in Equation 10.

$$R = \min(\frac{D_M}{4} + \frac{T_{LC}}{2}, \frac{D_M}{2}) \quad (10)$$

Here, R stands for the vertical coordinate of the ship rotational centre, expressed in metres, and D_M is the moulded depth of the ship, in metres; T_{LC} is the draught at midship for the considered loading condition. If this variable is not defined, another variable T_{SC}, defined as the scantling drought, can be equivalently utilized. However, the other two coordinates of the location of the CR still need to be studied.

In this work, more detailed, reasonable, and relevant characteristics of the CR are proposed based on the performance of the ship’s motions, as mentioned previously. The CR is the point at which linear and rotational motions are least correlated. This is quite an abstract definition, which can be explicitly explained as the position at which the amplitudes of the rotational motions are minimal and only influence the linear motions through the offsets. Therefore, a few optimal iterative methods such as the least-squares (Sotnikova, 2012 [56]), maximum likelihood (Åström, 1976 [57]) (Clark, 2010 [58]), and gradient descent (Fitch, 1991 [59]) methods can be applied to find this minimum position of the linear motions with an appropriately designed cost function. As it is well known that the optimal or regressive iterative methodologies require longer computation times, they are capable and sufficient to apply to research without a strict time limitation. However, when trying to process data in real time as ships are on voyages or missions, these complicated methods are no longer suitable or feasible. With such time-consuming methods, the expected results cannot be generated in time, which adversely affects ship motion strategies and decisions for the next step.

3.3 Measurement Devices

Measurement devices are most widely applied onboard to acquire and record the complete procedures of ship motions. The obtained information, also known as the motion data, can be utilized to analyse the ship’s behaviour and estimate and predict the surrounding wave status. There are several types of measurement devices nowadays, and they all have their specialties. An accelerometer can measure linear acceleration. A gyro can acquire rotational rates. A global positioning system (GPS) receiver determines local relative geographic information, and a magnetometer is used to obtain the direction information of a magnetic field. Devices may also benefit from the assistance of the global navigation satellite system (GNSS) or hydroacoustic measurements with a virtual vertical reference (Rogne, 2015 [6]).

The traditional method to measure ship motions requires a few sensors with a basic deployment that includes accelerometers and gyros. This type of sensor is not extremely expensive, but a certain number of sensors is needed to obtain enough motion information. Outdated versions of such sensors have long cables, which makes installation much more complicated. Therefore, placing experimental instruments onboard would require additional time that could otherwise be used for the experiment itself. However, with recent technological developments, the significant features of sensors include wireless connectivity, high integration, portability, built-in batteries, large storage space, and so forth (Abankwa, 2015 [60]). With the development of integration, the inertial measurement unit (IMU) has been widely applied in both research and industry, for instance, in the manoeuvring of aircraft, unmanned vehicles, and so on. The common IMU is a combination of accelerometers and gyros, and may also include a magnetometer. An additional GPS module can be deployed in an IMU to obtain accurate geographic information. With assistance of cameras, an optical motion system was constructed to acquire more precise motion information along a ship (Abankwa, 2018 [39]). For the convenience of handling ships appropriately, acquiring related motion information should be fast and accurate, especially under extreme weather conditions. Hence, a rapidly deployed measurement unit or an operating sensor is urgently expected for the researchers and crew (Hibbert, 2013 [61]).

Several novel technologies and relevant algorithms can be utilized when measuring and predicting ship motions. With new functions, more accurate motion data could be recorded and even processed in real time. Measurement devices can be remotely controlled by a computer or even by a smartphone via the Internet. These advanced technologies make observing, measuring, and analysing ship motions much more manageable and feasible than in previous times. Meanwhile, measurement units have advantages of size and portability over the previous devices. With the realization of industrial-grade high integration, it will be possible to install all the required modules into a single sensor box with a length of 10–20 cm or even smaller.

However, with multiple functions, the cost will increase. Measurement devices with high technologies and advanced techniques, such as a GPS, will of course require more cost, more human efforts, more computational time, an additional dependency on GPS availability, and increased fuel consumption, which result in certain restrictions when applying these devices. For instance, although novel and high technologies have advantages, in a few circumstances, where limitations of work or research exist on the aspects of funding, the ship’s conditions, or computing resources, such expensive and complicated devices may not be suitable for further application. Lower-cost and simplified operations would be the priority when implementing experiments onboard in real-world scenarios. Therefore, if the basic IMU performance could satisfy the research requirements, no more complex measurement devices are installed onboard. This type of measurement device should be applicable to most use cases. Hence, its construction and placement should be easy as well. The enhancement of the measurement accuracies of the basic IMU would be necessary, and methodologies to eliminate the corresponding bias or errors are imperative as well.

Furthermore, the operation becomes more complicated with the development of technology. The sensor box is equipped like a small computer, and it must handle several tasks, such as recording information about the temperature, weather conditions, date, linear accelerations, rotational motions, and GPS location; saving all these data to a memory card or a server; and sometimes this information should also be contemporaneously displayed on a monitor. Thus, all modules should cooperate, such that programming on this sensor box is an important and time-consuming aspect of its correct application. However, if the sensor box does not function appropriately, or something interrupts the recording program, it would be troublesome for the crew or the researcher to restart or fix the sensor box, especially if this process requires professional knowledge. Hence putting the sensor box on a ship or vessel to record her entire voyage would pose challenges, particularly when it lasts for a long time.

Moreover, when preparing to record the ship motion information, the measurement units or devices should be installed in an ideal position, where the following features are satisfied. First, the external effects are the least. For example, the measurement units remain still when recording. Second, the interior environment of the ship is safe. Many electric devices are onboard, and thus avoiding electromagnetic interference is necessary for the benefit of all electric devices. Finally, the position should be conveniently reachable. For instance, if a measurement device crashes while recording, the device should be replaced or reset immediately; therefore, the installation position must be rapidly accessible. The less time is needed to install, replace, or fix the measurement units, the more information will be recorded. Furthermore, because detecting the CR's position is not possible initially, the CG (if known) would be the ideal location to install the measurement devices when possible. In this way, the probable coincidence of the CR and CG is verified, and their relative position is acquired.

As a result, some researchers are focusing on novel methodologies to enhance the performance and abilities of measurement devices. Other researchers prefer to use existing technologies to achieve much safer and more stable device performance. These two different emphases lead to various solutions. This research focuses on the latter, using one or two low-cost sensor boxes equipped with a basic IMU integrating accelerometers and gyros to record motion data. The sensor box is convenient to operate by anyone on the ship, by simply installing it at any location and then pressing a switch on the device. Hence, it is probable to install the device onboard to operate for several months without the intervention of professional researchers.

With a basic IMU equipped with accelerometers and gyroscopes, the linear accelerations and rotational rates of ships can be obtained. After analysing the measured data from the IMU, either ship motions or wave characteristics can be described and expressed. Thus, more applications can be realized, such as the prediction of the ship's behaviour and trajectory tracking. According to the increased demand, the linear accelerations and angular rates alone are no longer sufficient to illustrate ship motions clearly and precisely. Therefore, the expectations of the ship's positions and rotational angles are increasing. By applying methodologies concerning one or two numerical integrations, the basic IMU's measured data can be used to generate related positions and angles. However, this kind of integration will also introduce infinite drift by enhancing the sensor's noise, bias, and misalignment caused by the production process, and then add those errors into the actual ship motion data. Therefore, researchers are now more likely to apply GPS, as Godhavn (2000 [62]) and Fossen and Peter (2009 [63]) have already done, magnetometers, and other similarly expensive devices to modify and correct the motion data, rather than simply utilizing the basic IMU, to eliminate the produced bias and avoid undesirable drift.

3.4 Feasible Requirements of the CR

Based on the previously discussed research status, after considering the characteristics of ship motion and the structure of measured motion data, a list of applicable requirements to determine the location of the CR can be generally described as follows:

1. The location of the CR for each trial is individual, but in total, all locations should at least remain within a certain range, dependent on the wave characteristics. That is, when encountering similar conditions of waves, the locations of the CR for the corresponding sea trials should be similar or even identical.

2. The estimated offset values should be systematic with various encountered waves. For example, their signs should be different when waves come from the portside compared to those when waves come from the starboard side.

3. The averaged discrepancy of the errors among all offset values should be no larger than 1% of the ship’s length.

4. The measurement devices should be installed in an accessible location and easily operable for everyone, to implement certain remedial operations such as resetting or restarting when problems occur. The shorter the time required to fix any problems, the more useful and precise data is recorded.

5. The number of employed measurement devices should be as few as possible, while still obtaining sufficient motion data.

6. To avoid redundant computations, instead of introducing many ship's coefficients that are not acquirable under certain circumstances, implementing available information such as measured motion data would be better. The appropriate methodology to determine the location of the CR should reduce computation time and complexity, thereby enhancing the performance of the algorithm in preparation for real-time calculations in the future.

4 Methodology of CR Determination

The first step to determine the CR is to collect the ship motion information with well installed onboard measurement devices in known positions. The second step is to construct mathematical models that can clearly and precisely illustrate the relationship between the ship motions at the CR and the position information of the measurement devices. Finally, with the assistance of the known data from measurement devices and the mathematical model, the location of CR can be determined. The next step is to analyse the ship motions at this CR, and then even calculate or predict the wave information. Although this actual CR's location might not be unique, their probable average values or intervals can be determined by processing the measured data, and the distance between the CR and CG can also be analysed using parameters such as the ship velocity and wave incident angles.

In this chapter, the sensor boxes employed for all the experiments are described and the measured motion data obtained from them are presented. Secondly, in consideration of the structure of the measured motion data, an appropriate method, namely the Kalman filter, is proposed to construct a mathematical model, which can be utilized to determine the location of the CR. Next, a detailed description of the Kalman filter is provided, including the variables, system model, and observation model. Afterward, based on the required variables of the Kalman filter, the processing of the measured data is illustrated. Then, two simulations are implemented to test the feasibility and accuracy of the Kalman filter.

4.1 Description of the Measurement Units

Self-made, low-cost sensor boxes were utilized and intended to be flexible and universally applicable in a diverse range of ships. These have the advantages of lower expense, less human effort, less computation time, and being more easily understood by the crew on the ships. For all the experiments illustrated in this research, the sensor boxes were well organized and then installed onboard for the sake of convenience and accuracy when processing the measured data afterward. Both sensor boxes utilized an ARM-controller (STM32F407) to sample data, and then wrote data to a serial interface. Sampling was controlled in both sensor boxes by a crystal oscillator with a precision of approximately ± 100 ppm (parts per million). The recorded data from the sensor boxes were stored on locally installed micro-SD memory cards to facilitate processing the measured motions offline. On the external case of the sensor box, there is an LCD display indicates the date and recording values of data, as well as five black buttons providing status information and allowing to setup and control the data acquisition, as shown in Figure 4.1.

4.1.1 Sensor I

Sensor I was placed on the Fathom 10 and Agulhas II in 2014, 2015, and 2017. It contains an accelerometer, that is a 3-axis LIS302DL from the ST-Microelectronics and two gyros, these are two 1-axis CRS03 from the Silicon Sensing for roll and pitch motion respectively. When conducting the experiments, the internal sampling rate was 50 Hz, and the output data rates serial was set to 10 Hz. The output files produced by Sensor I contain ten columns, which are the time in seconds since the measurement started, angles for roll and pitch, angular rates for roll and pitch, debug information, power supply voltage, and linear accelerations in three dimensions.

4.1.2 Sensor II

Sensor II was placed on Agulhas II in 2017, and it was always carried by Simon Stevin. The internal sampling rate was 400 Hz, and the output data rates serial was 8 Hz. The accelerometer was a 3-axis KXTF9 from the Kionix, and there was a 3–axis IMU-3000 from the InvenSense to measure angular rates for roll, pitch and yaw. The differences between Sensor I and II are that Sensor II has an extra GPS module and yaw motion. Thus, the output files produced by Sensor II have 13 resulting columns, including the date, time in hours, GPS flag, GPS data, GPS time, latitude, longitude, angular rates in three dimensions, and finally, linear accelerations in three dimensions.

Figure 4.1 Onboard sensor box

4.2 Measured Data Processing

For various practical applications of measured data, accelerations and angular rates alone may be insufficient. In such cases, more information about linear velocities, positions, and rotational angles is also required. Thus, one common way to obtain that required information is by using integration and differentiation in the time domain. However, such additional calculations performed on the raw data would generate drifts and errors during the computation process (Hu, 2013 [29]); therefore, after the calculations, the generated data should be filtered in the next step to remove undesired computational artefacts from the data.

4.2.1 Process with Integrated Data

In this work, when integrating the angular rates, the trapezoidal integration method is applied [64][65], and thus the corresponding angles are produced. Take the pitch angular rate in one trial from the Agulhas II as an example. As shown in the following figure, the curve describes the power spectrum distribution of the integrated pitch angle in the frequency domain. The y-axis represents the power of the pitch angle. Welch's power spectral density estimation is used to express the frequency domain of the integrated pitch angle [66]. Figure 4.2 demonstrates the existence of the drift caused by the integration. It is completely drifted out and strongly affects the actual spectrum distribution, because there are no other apparent components in the spectrum, except for the significant power around zero frequency.

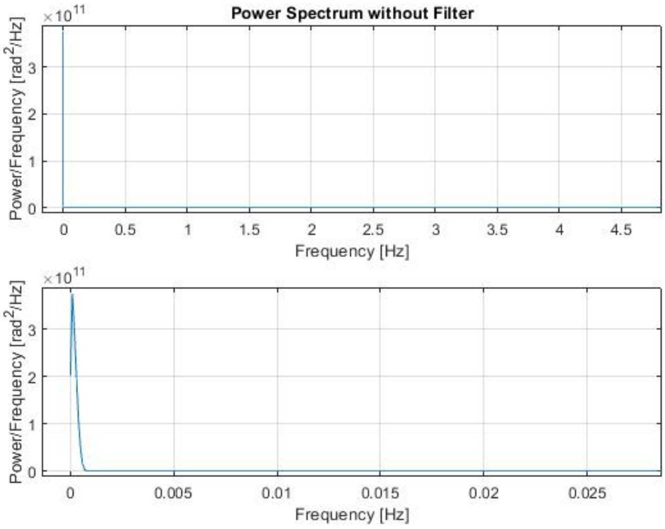

Figure 4.2 Original spectrum of the integrated angle

Therefore, a high-pass filter is utilized to resist this drift, eliminate the unreasonable power distribution at lower frequencies, and let the higher frequency pass. A Butterworth filter is applied in this work because it is designed to have as flat a response as possible in the passband and it is convenient to adjust related parameters, such as the cut-off frequency [67][68]. A cut-off frequency is defined as an edge in a filter that gives a frequency boundary between passband and stopband (Zumbahlen, 2011 [69]). The appropriate selection of the cut-off frequency varies with respect to different ships and their relative motions caused by encountered waves. In this work, based on the recorded original pitch angular rate, the peak frequency is approximately 0.13 Hz. Hence, when choosing the cut-off frequency of the high-pass filter, below 0.13 Hz is reasonable.

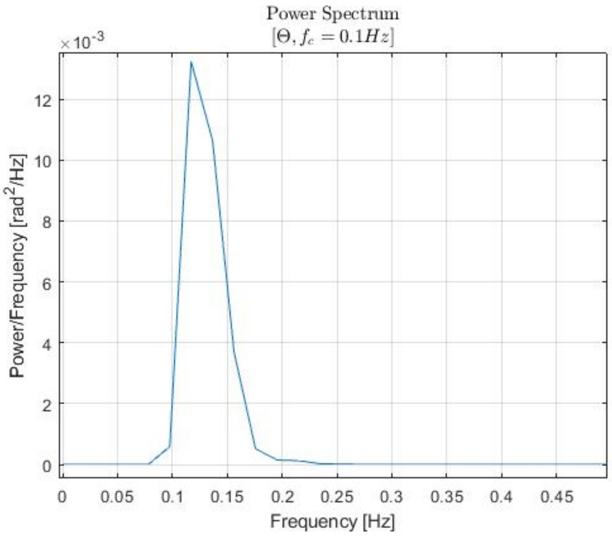

Figure 4.3 Spectrum of filtered integrated angle at f_c=0.1 Hz

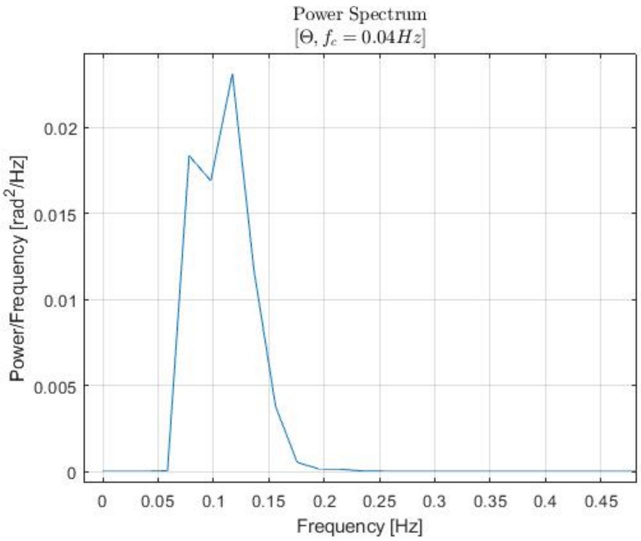

Figure 4.4 Spectrum of filtered integrated angle at f_c=0.04 Hz

According to Figure 4.2, the dominated power is mainly around zero frequency. Hence a low cut-off frequency below 0.13 Hz would be sufficient to omit this drift part. When the cut-off frequency, namely f_c, is 0.1 Hz, the actual spectrum distribution appears as described in Figure 4.3. However, judging from the figure below 0.1 Hz, there are still some power components at 0.07 Hz. Hence, by reducing f_c to 0.04 Hz, as shown in Figure 4.4, the entire power distribution is well expressed. When further reducing the cut-off frequency to 0.03 Hz, as shown in Figure 4.5, is the same as Figure 4.4, showing no obvious change with a lower cut-off frequency. Thus, it is not necessary to continue reducing f_c, and the final cut-off frequency is set to 0.04 Hz. The frequency characteristics of the calculated pitch angle are expressed in Figure 4.4. The Butterworth filter with this selected cut-off frequency and at the sixth order is applied to all the integrated angles for the whole series of experiments.

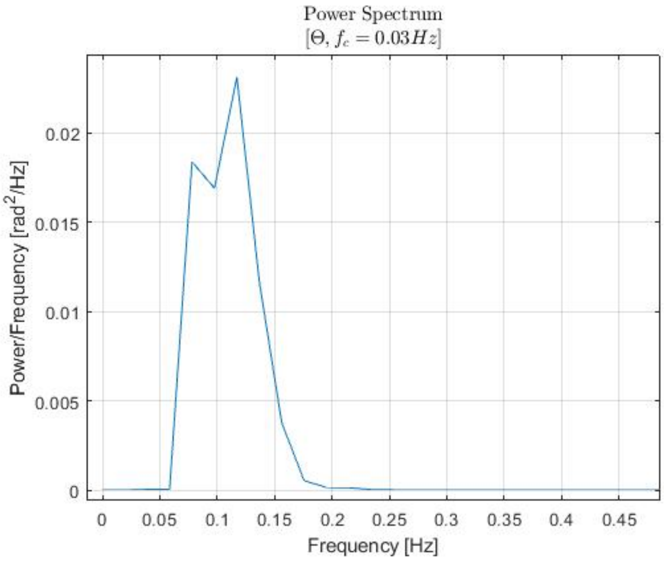

Figure 4.5 Spectrum of filtered integrated angle at f_c=0.03 Hz

In the process of using Welch’s estimation in MATLAB to calculate the power spectrum of this integrated pitch angle, there are three parameters to be clarified. One is the window that determines the length of the segments when dividing the input signal. The default window setting uses the Hamming window to obtain the eight segments. The second is the number of overlapped samples; this is utilized to set the length of the overlapped samples, which should be smaller than the window’s length. The default is 50% between each segment. In this work, these two parameters are set to default.

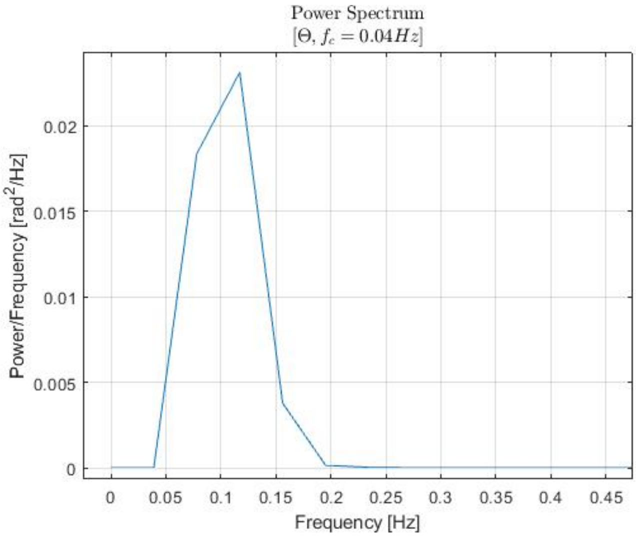

Figure 4.6 Pwelch with nfft of 256

The third parameter is the number of Fourier transformation points, abbreviated as nfft. It has been modified several times to obtain a precise power spectrum with enough details efficiently. As mentioned before, the dominant peak should appear at approximately 0.13 Hz, considering the original pitch angular rate characteristics. Figure 4.6 shows the power spectrum with the number of Fourier transformation points at 256, and this is the default number in MATLAB, while Figures 4.7 and 4.8 show the power spectra at 1024 and 2048, respectively. The final number we applied in this work is 512, as shown in Figure 4.4. Figure 4.6 gives a different shape of the power distribution from the others, indicating that the power spectrum characteristics are not entirely discovered owing to the smaller nfft. From the nfft value of 1024, the spectrum becomes noisy and more peaks appear. When nfft is 2048, the higher power spectrum even appears before the supposed dominant frequency. After comparing all these figures with different values of nfft, the best result is given by 512, as shown in Figure 4.4.

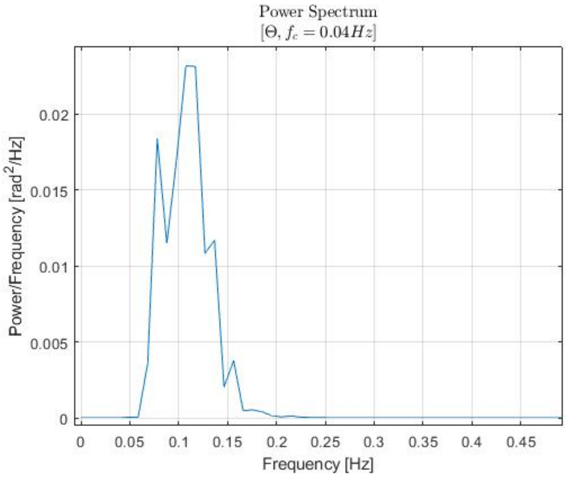

Figure 4.7 Pwelch with nfft of 1024

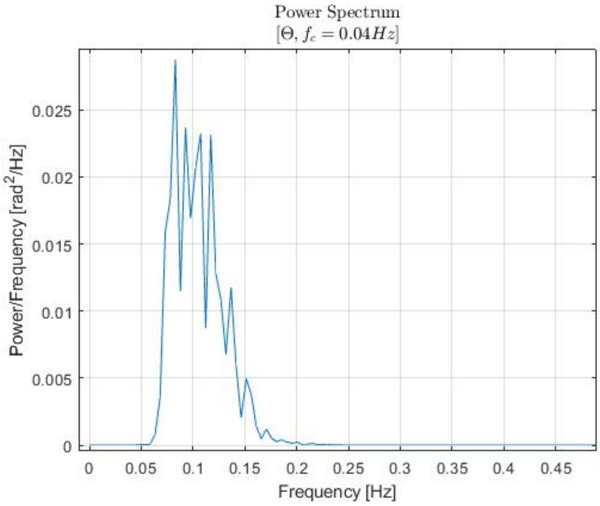

Figure 4.8 Pwelch with nfft of 2048

4.2.2 Process with Differential Data

Usually, the measured noise would appear in the high frequencies within the raw measured data. Moreover, the angular accelerations are generated by differentiating the raw angular rates, which also induces noise. Thus, a low-pass filter is essential to process these noises. In this work, a window-based FIR filter is applied at the 34th order with a Hamming window [70][71]. As shown in Figure 4.9, the power spectrum is also calculated by Welch's estimation method using the same parameters described in Chapter 4.2.1. These two curves are identical but with different ranges of the x-axis. They describe a frequency spectrum of the pitch angular acceleration. The upper figure is the original one and shows that the entire spectrum distribution appears under the frequency of 1 Hz. Therefore, a specifically selected interval of the x-axis is set and expressed in the figure below. Hence, the cut-off frequency is set at 1 Hz.

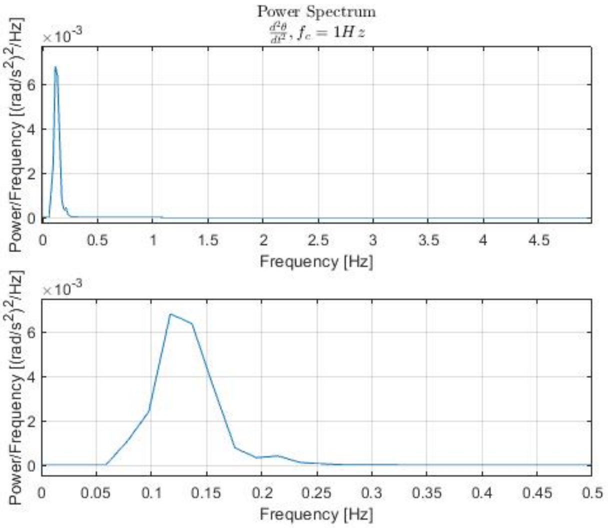

Figure 4.9 Spectrum of the angular acceleration at f_c=1 Hz

4.3 Introduction of the CR's Determination Method

As depicted above, the linear accelerations in three dimensions and angular rates in two or three dimensions were measured and recorded by two separate sensor boxes, the onboard installation of which as restricted by the structure of the ships when the actual sea trials were in progress.

The detailed description of all the ship's related hydrodynamic parameters can enhance the complexity when constructing the ship motion's mathematical model. It is much less complicated to introduce only the known accelerations and angular rates into the mathematical model. By introducing the definition of the offsets as illustrated in chapter 2.4.2, it is possible to describe the relationship between the measured motion data and the actual ship motion. To be more specific, the offset is expressed as the distance between the installed sensor box and the location of the CR in three dimensions.

In summary, the knowledge of linear accelerations and angular rates for different axes is obtained. The influence exerted by the offset on the linear motions in three dimensions is known. Moreover, the expected results are the motions and the offset in three dimensions. Considering the conditions mentioned previously, it is better to construct the system model in space for convenience and feasibility. In addition, a filter algorithm is also necessary owing to the errors and noise from the measured motion data, which are undesirable and must be processed. Therefore, a method that can describe the state space performance and include the noise model simultaneously is required. Because the Kalman filter is adapted to calibrate the current data and capable of predicting the motion's tendency in the future with known data, it is suitable to apply the Kalman filter to construct the appropriate mathematical model and eliminate redundant errors, noise, or bias, thus generating more accurate results.

4.4 Kalman Filter

Rudolf Emil Kalman invented the Kalman filter (KF), which is an optimal recursive data processing algorithm for linear systems. Since then, the Kalman filter algorithm has been widely applied both in industry and research. It can solve many navigation problems, control systems, sensor data fusion, certain military applications, etc. For objectives with non-linearities, where the traditional Kalman filter has limited and imprecise applicability, the extended Kalman filter (EKF) (Ehrman, 2008 [72]), unscented Kalman filter (UKF) (Wan, 2000 [73]), and other derived modified KF methods (Kulikov, 2016 [74]) (Zhang, 2005 [75]) (Du, 2013 [76]) (Germani, 2005 [77]) have been generated to deal with the non-linear system and more complicated environments.

4.4.1 Introduction of Kalman Filter

The Kalman filter is an algorithm that takes a series of measurements over time, including noise and bias, and generates the estimated corresponding variables in the time domain for the current time or the near future, depending on the application. As shown in Equation 11, x_k is the state vector at time k that can be calculated from the state at time k-1, namely x_{k-1}, and the related state transition model F_k. The observation vector z_k is derived from the x_k with the observation model H_k.

$$\begin{cases} \mathrm{x_k} = \mathrm{F}_k \mathrm{x}_{k-1} + \mathrm{u}_k + \mathrm{w_k} \\ \mathrm{z_k} = \mathrm{H}_k x_k + \mathrm{v_k} \end{cases} \quad (11)$$

where w_k and v_k are the process and observation noise, both of which are assumed to be zero-mean Gaussian noises with covariance Q_k and R_k, respectively (Kalman, 1960 [78]) (Gupta, 2007 [79]). In this work, there is no control vector included, and u_k is thus ignored.

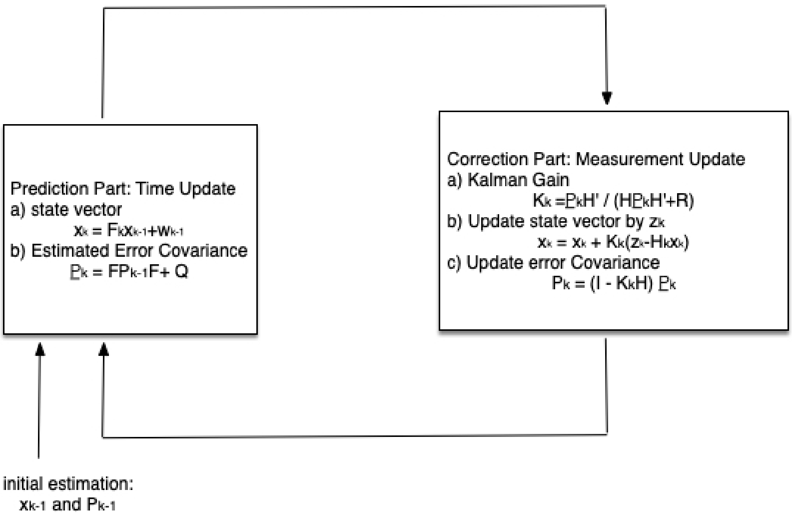

Figure 4.10 Kalman filter process

Figure 4.10 shows the basic operational principle of the Kalman filter, and the process is divided into two parts, as expressed. In the first part, known as the prediction phase, the initial state value x_{k-1} and covariance value P_{k-1} at time k-1 are used to calculate the estimated state vector x_k and error covariance P_k at time k. P_k is a measure of the accuracy of the state estimation, which is first calculated in the prediction part and then fixed in the correction part, as expressed in Equation 12 and Equation 13. Every component in the matrix constitutes the covariances of the errors of the related state variables.

$$P_{k-1} = cov(x_k - \tilde{x}_{k-1}) \text{ (12)}$$

$$P_k = cov(x_k - \tilde{x}_k) \text{ (13)}$$

In the second part, namely the correction phase, according to the calculated estimated state vector x_k in the previous step, the Kalman gain can be produced. Meanwhile, the estimated measurement vector z_k at time k can be computed as well. The correction of state vector $\tilde{x}_k$ at time k can be generated by multiplying by the Kalman gain, which should be much closer to the expected values. The error covariance $\tilde{P}_k$ is also corrected by the Kalman gain simultaneously. Finally, the corrected state vector $\tilde{x}_k$ and the updated error covariance $\tilde{P}_k$ at time k are applied to the next loop as the known state value, and the process restarts from the first phase until the maximum value of k is reached.

4.4.2 Euler Transformation

When discussing ship motions, these are generally based on the inertial coordinate system, whereas the measured motion data are in another coordinate system, known as the sensor's own frame. For this reason, the implemented sensor boxes were carefully installed to be parallel to the ship body-fixed frame. Therefore, the difference between the sensor's frame and the ship body's frame would simply be the positional deviation, namely the offset, without additional rotational operations, and thus, the only problem to be solved would be the transformation between the inertial and ship body-fixed frames.

The relationship between the inertial frame and the ship body-fixed frame can be represented by a transformation matrix, which can be applied to transform the motions from the inertial coordinate to the ship body-fixed coordinate to obtain an appropriate reference, and vice versa. One famous and widely used transformation matrix is the Euler transformation (Fossen, 2011 [8]). Figure 4.11 shows the transformation process with the Euler angles, where ϕ stands for roll, which rotates around the x-axis; θ represents pitch, which rotates around the y-axis; and ψ refers to yaw, which rotates around the z-axis. According to the figure, the relationship between the original and transformed coordinates can be substituted using the Euler angles. The Euler transformation matrices R with subscripts, indicating the rotational axis and related Euler angle, are described in Equation 14.

$$\mathrm{R}_{x,\phi} = \begin{bmatrix} 1 & 0 & 0 \\ 0 & \cos\phi & -\sin\phi \\ 0 & \sin\phi & \cos\phi \end{bmatrix}, \mathrm{R}_{y,\theta} = \begin{bmatrix} \cos\theta & 0 & \sin\theta \\ 0 & 1 & 0 \\ -\sin\theta & 0 & \cos\theta \end{bmatrix}, \mathrm{R}_{z,\psi} = \begin{bmatrix} \cos\psi & -\sin\psi & 0 \\ \sin\psi & \cos\psi & 0 \\ 0 & 0 & 1 \end{bmatrix} \quad (14)$$

With the transformation matrices, the Euler angles roll (ϕ), pitch (θ), and yaw (ψ) can be utilized to decompose the velocity vector $v_n$or acceleration vector a_n in the inertial frame, and then transfer them to the ship body-fixed coordinate system. Let R_n^b represent the rotation matrix in the direction from the earth frame to the ship body-fixed frame under the condition of employing Euler angles as described before. Hence,

$$\mathrm{v}_\mathrm{n}^\mathrm{b} = \mathrm{R}_n^\mathrm{b} \cdot \mathrm{v}_\mathrm{n} \quad (15)$$

$$\mathrm{a}_\mathrm{n}^\mathrm{b} = \mathrm{R}_\mathrm{n}^\mathrm{b} \cdot \mathrm{a}_\mathrm{n} \quad (16)$$

where $R_n^b = R_{x,\phi}^T \cdot R_{y,\theta}^T \cdot R_{z,\psi}^T$, substituting Equation 14, and thus generating the complete expression of the Euler transformation matrix, as shown in Equation 17.

$$\mathrm{R}_\mathrm{n}^\mathrm{b} = \begin{bmatrix} \cos\theta\cos\psi & \cos\theta\sin\psi & -\sin\theta \\ -\cos\phi\sin\psi + \sin\phi\sin\theta\cos\psi & \cos\phi\cos\psi + \sin\phi\sin\theta\sin\psi & \sin\phi \mathrm{s}\cos\theta \\ \sin\phi\sin\psi + \cos\phi\sin\theta\cos\psi & -\sin\phi\cos\psi + \cos\phi\sin\theta\sin\psi & \cos\phi\cos\theta \end{bmatrix} (17)$$

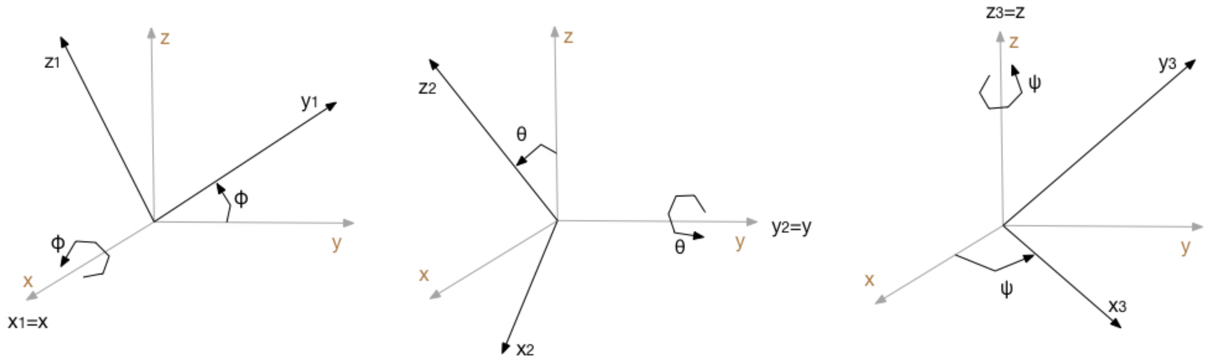

Figure 4.11 Euler transformation process

Based on the application with the Euler transformation, it has advantages of better analysing and describing a ship's behaviour under different circumstances, and thus more accurate research results can be obtained to express a clear and precise understanding of ship motions in the actual sea state.

4.4.3 Input Mathematical Model

The sensor boxes applied in this study can obtain time series of linear accelerations and angular rates. Therefore, the measured accelerations from the sensor boxes are used as the measurement inputs. The angular rates are considered as identical at any point of the ship, under the assumption that the whole ship body is a rigid body. Thus, the corresponding angles can be generated by integrating the angular rates, which are used as the additional known inputs. Moreover, the angular accelerations can be produced by differentiating the angular rates and treated as known information.

To establish a mathematical model based on the measured motions data from the sensor boxes, we should be aware that there will be differences between the accelerations at the CR and those at the installed sensor box. These differences are mainly caused by the offset, and the influences caused by the sensor's own bias and instrument errors have been considered as well.

As the complete motion data are recorded, the Kalman filter is applied here to filter and correct the data. As illustrated in Chapter 4.4.1, the entire procedure of the Kalman filter is explicitly depicted in the following part for this determination algorithm. In the prediction part, the initial linear accelerations and offset are set to zeros. Afterward, the state vector at the next time is calculated with the transition matrix, namely the unit matrix in this work. No extra calculation of the state vector is depicted here because we want to avoid many hydro-coefficients and previous knowledge requirements. Hence, the first propagated state vector and its error covariance are obtained. These two components are then applied to the correction part. In the correction part, the result from the propagated state vector and the mathematical relationship is acquired. Then, the sensor-measured linear accelerations are introduced. Thirdly, the difference between the result and the measured data is obtained and utilized to generate the correction factor. With this correction factor, the propagated state vector and its *P* matrix are compared and corrected, and then applied to the next loop. Hence, the state vector at each time is only related to the previous time and the present measured data. Each loop updates the error covariance and corrects the state vector, and thus the bias from the measured data can be eliminated to generate the actual linear accelerations and offset.

As illustrated above, the variable for the mathematical model should be the linear accelerations at the CR in three dimensions $[ax_n, ay_n, az_n]^T$, where the subscript n represents the inertial frame. Moreover, in this study, the distance between the sensor box and the ship's CR is defined as the offset vector $[r_x, r_y, r_z]^T$. That is, the state vector x_k has six variables, namely $[ax_n, ay_n, az_n, r_x, r_y, r_z]^T$, and their initial values are set to zero. Furthermore, P_k is set up as a sixth-order identity matrix with a value of 0.5 in the diagonal line. In the prediction part, to construct a simple but sufficient model, the transition matrix F_k is set as a unit matrix with six dimensions.

At the location of the CR, based on the circular theory, the offset affects the linear accelerations in concert with the angular accelerations. The relative linear accelerations caused by the offset and the angular accelerations in three dimensions are expressed by the vector $[ax_{off}, ay_{off}, az_{off}]^T$; the relation is illustrated in Equation 18, where $\ddot{\phi}, \ddot{\theta}, \ddot{\psi}$ are the angular accelerations of the Euler angles. Hence, the linear accelerations are produced by angular accelerations cross-multiplied by the offset vector.

$$\begin{bmatrix} \mathrm{ax_{off}} \\ \mathrm{ay_{off}} \\ \mathrm{az_{off}} \end{bmatrix} = \begin{bmatrix} \ddot{\phi} \\ \ddot{\theta} \\ \ddot{\psi} \end{bmatrix} \times \begin{bmatrix} \mathrm{r_x} \\ \mathrm{r_y} \\ \mathrm{r_z} \end{bmatrix} \quad (18)$$

To conclude the foregoing, in the correction part, the linear accelerations from the sensor boxes should be regarded as the known information as the measurement vector z_k, referred to as $[ax_s, ay_s, az_s]^T$. In consideration of the resultant effects, the measured motion data are made up of the wave-induced motions at the CR and the linear motions created by the offset. Thus, the mathematical model for ship motion in the correction part of the Kalman filter can be established as expressed in Equation 19:

$$\begin{bmatrix} \mathrm{ax_s} \\ \mathrm{ay_s} \\ \mathrm{az_s} \end{bmatrix} = \left[\mathrm{R_n^b} \cdot \begin{bmatrix} \mathrm{ax_n} \\ \mathrm{ay_n} \\ \mathrm{az_n + g} \end{bmatrix} + \begin{bmatrix} \mathrm{ax_{off}} \\ \mathrm{ay_{off}} \\ \mathrm{az_{off}} \end{bmatrix} \right] \quad (19)$$

where $[ax_s, ay_s, az_s]^T$ refers to the measured linear accelerations at the sensor box in the ship body-fixed frame. $[ax_n, ay_n, az_n]^T$ represents the linear accelerations at the CR in the inertial coordinate system, R_n^b is the Euler transformation matrix which transfers the motion from the inertial coordinate system to the ship body-fixed frame, g represents the gravitational acceleration, and the linear accelerations contributed from the offset, represented as $[ax_{off}, ay_{off}, az_{off}]^T$, are described in Equation 19 above.

In this study, the gravitational acceleration should be considered in the vertical direction. Moreover, except for Simon Stevin and the catamaran, the yaw motion is neglected because it is too small to impact the other motions, owing to the implemented experiment conditions. Therefore, the whole model can be expressed in detail as shown in Equations 20 and 21 below, where Equation 21 shows the state of ignoring the yaw motion. After introducing Equations 17 and 18 into Equation 19, the primary mathematical model is generated to find the CR's location.

$$\begin{bmatrix} ax_s \\ ay_s \\ az_s \end{bmatrix} = \begin{bmatrix} ax_n\cos\theta\cos\psi + ay_n\cos\theta\sin\psi - az_n\sin\theta - g\sin\theta + r_z\ddot{\theta} - r_y\ddot{\psi} \\ ax_n(\sin\phi\sin\theta\cos\psi - \cos\phi\sin\psi) + ay_n(\cos\phi\cos\psi + \sin\phi\sin\theta\sin\psi) \\ +az_n\sin\phi\cos\theta + g\sin\phi\cos\theta + r_x\ddot{\psi} - r_z\ddot{\phi} \\ ax_n(\sin\phi\sin\psi + \cos\phi\sin\theta\cos\psi) + ay_n(\cos\phi\sin\theta\sin\psi - \sin\phi\cos\psi) \\ +az_n\cos\phi\cos\theta + g\cos\phi\cos\theta + r_y\ddot{\phi} - r_x\ddot{\theta} \end{bmatrix} \tag{20}$$

$$\begin{bmatrix} ax_s \\ ay_s \\ az_s \end{bmatrix} = \begin{bmatrix} ax_n\cos\theta - az_n\sin\theta - g\sin\theta + r_z\ddot{\theta} \\ ax_n\sin\phi\sin\theta + ay_n\cos\phi + az_n\sin\phi\cos\theta + g\sin\phi\cos\theta - r_z\ddot{\phi} \\ ax_n\cos\phi\sin\theta - ay_n\sin\phi + az_n\cos\phi\cos\theta + g\cos\phi\cos\theta + r_y\ddot{\phi} - r_x\ddot{\theta} \end{bmatrix} \tag{21}$$

4.5 Simulation Results

Two simulated models are introduced to test the feasibility of the determination method. As the locations of CR are predetermined, the estimated offset values should lead to the same locations of CR. Otherwise, the algorithm is not working correctly and properly. The first one is a simulated pendulum model in a plane. The second simulation system is constructed by the research group in Jade University of Applied Science to simulate catamaran motions in diverse sea environments. Based on the given information, the determination algorithm is modified for specific applications.

4.5.1 Estimated Results of Planar Motion

Figure 2.2 shows the fundamental relationship between the CR and an object with the contribution of the offset in a plane. Based on this relationship, as expressed in Equation 2, a simulated circular motion model is constructed with a known angular rate and linear acceleration at the object. The sampling frequency is 10 Hz and the motion lasts for 10000 s. The period of this simulated model pendulum is 6 s. According to the determination method, all parameters for this planar motion are not vectors. Thus, the Euler transformation is unnecessary and omitted. In the Kalman filter, a_{ob} and ω are regarded as the system inputs, the outputs are d_{oc} and a_{CR}, and the mathematical model is constructed based on Equation 2. To test the feasibility and accuracy of the Kalman filter, the distance d_{oc}, referring to the length of the pendulum, and a_{CR} are given and compared with the estimated outputs.

The results are shown from Figure 4.12 to Figure 4.19, which can be divided into two categories. One category shows estimated offset values, and the other contains comparisons of the input and calculated linear accelerations. They are generated under four different conditions, and the differences among these four pairs of figures are the offset values. The settled value starts from a short length of 0.2 m, and then increases to 1.5 m and 3 m. Finally, it reaches 8 m. These values are representative out of a large amount of settled values. The validation is carried out on 100 settled values up to 20 m. Overall, the results show that the Kalman filter is capable of determining two desired variables, d_{oc} and a_{CR}, within one equation for planar motion.

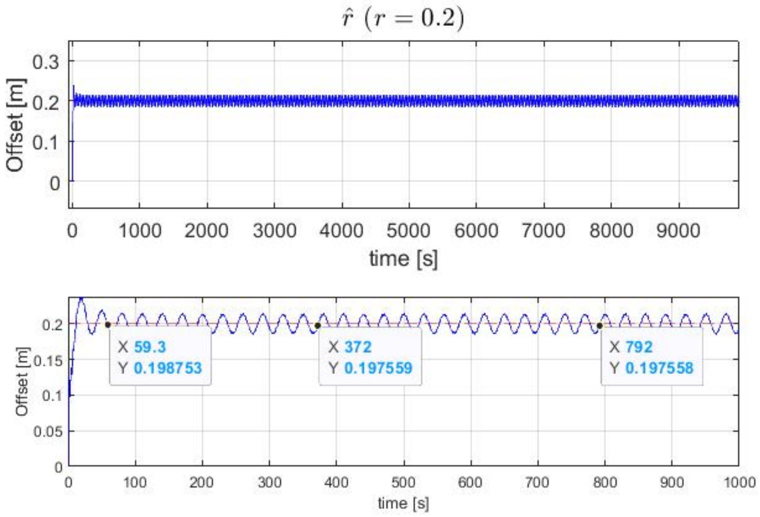

Figure 4.12 Result of KF distance when *r* is given as 0.2 m

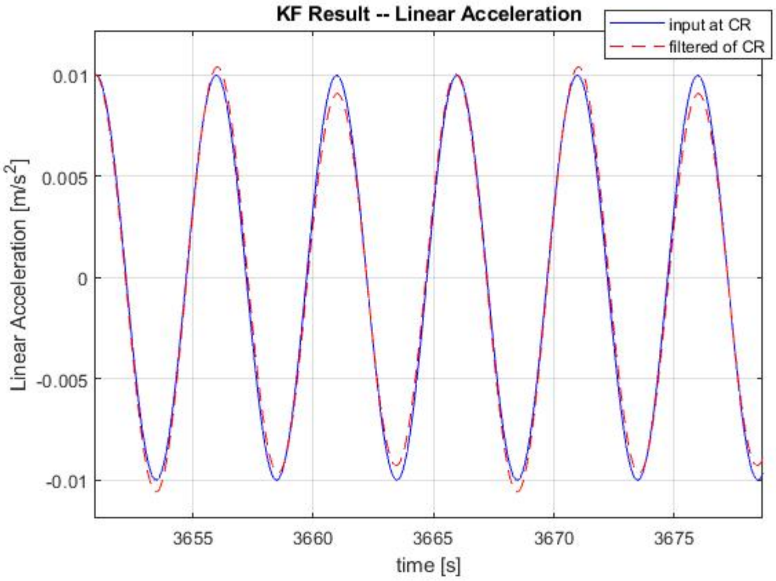

Figure 4.13 Comparison of linear acceleration at CR when *r* = 0.2 m

There are two subgraphs in Figures 4.12, 4.14, 4.16, and 4.18, which show the estimated offset values. The upper graphs describe the complete process of determining the distance, while the lower ones indicate more detailed adjustments. The blue curves indicate the estimated distance obtained from the Kalman filter, and the red horizontal lines in the lower subgraphs indicate the given distance. The trends of the blue curves show that the final estimated distances have reached their expected values after the adjustments. As expressed in the figures, the estimated results oscillate around the given values; they are more precise when the given distance values are not large, and the error is only 0.1%. Furthermore, a much shorter time is required to adjust the offset to their steady values in Figures 4.12, 4.14, and 4.16 than in Figure 4.18.

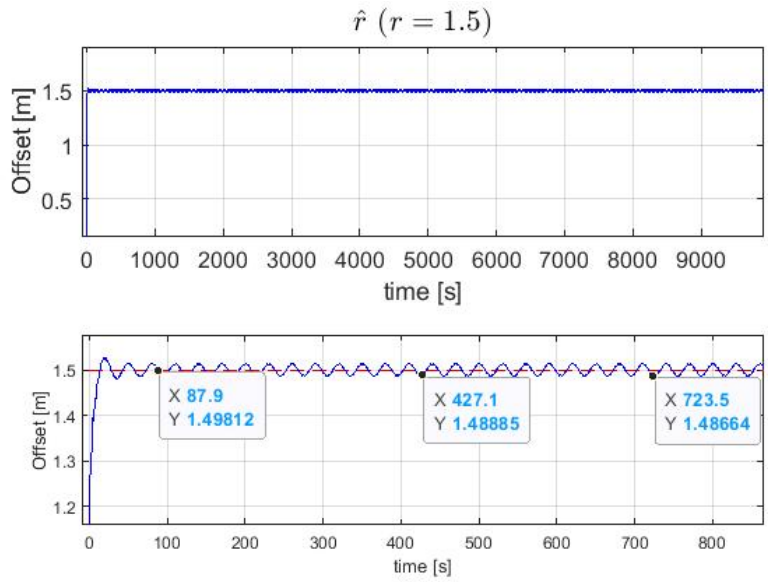

Figure 4.14 Result of distance when *r* is given as 1.5 m

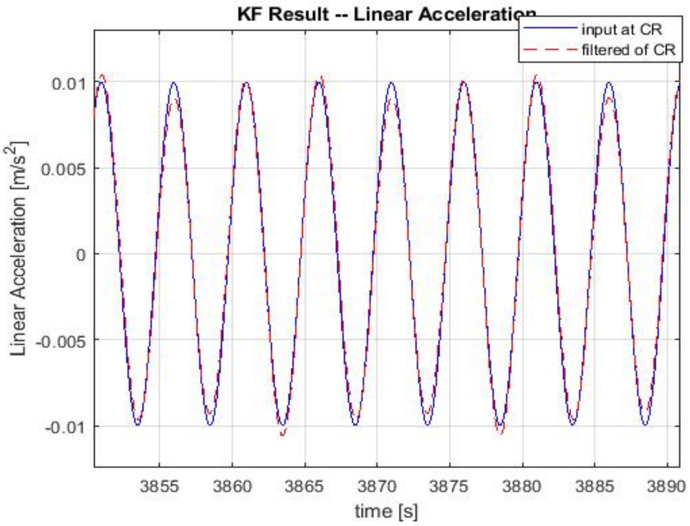

Figure 4.15 Comparison of linear acceleration at CR when *r* = 1.5 m

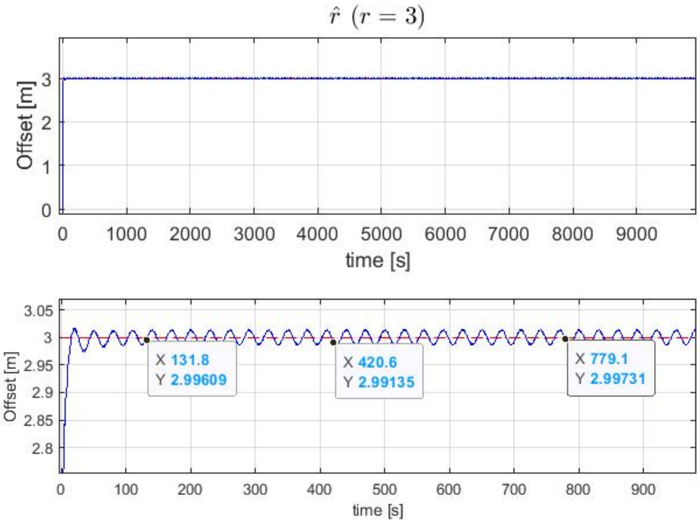

Figure 4.16 Result of KF distance when *r* is given as 3 m

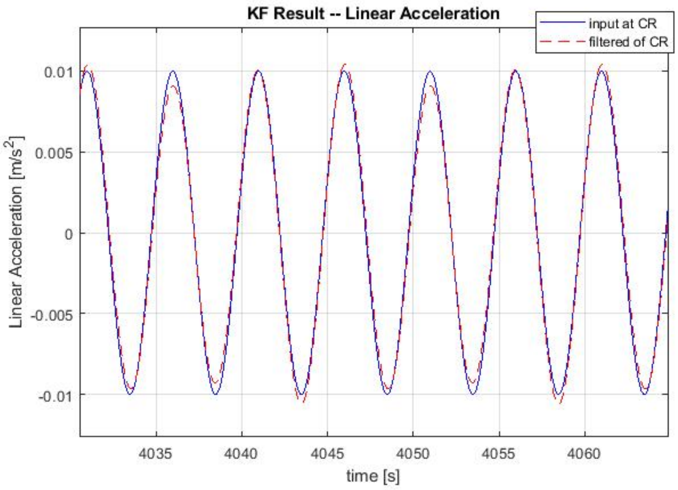

Figure 4.17 Comparison of linear acceleration at CR when *r* = 3 m

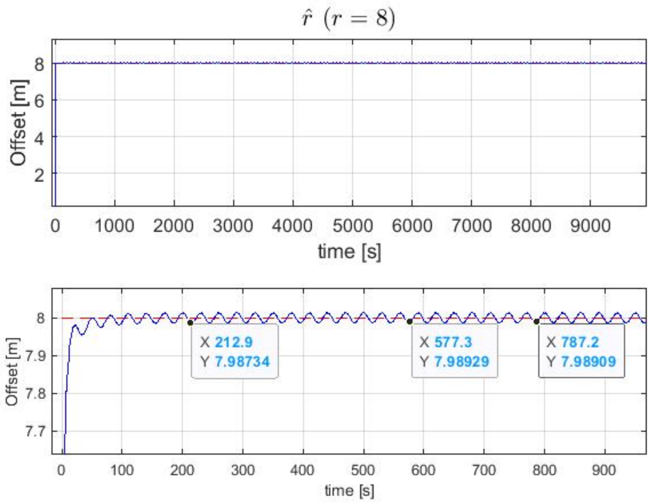

Figure 4.18 Result of distance when *r* is given as 8 m

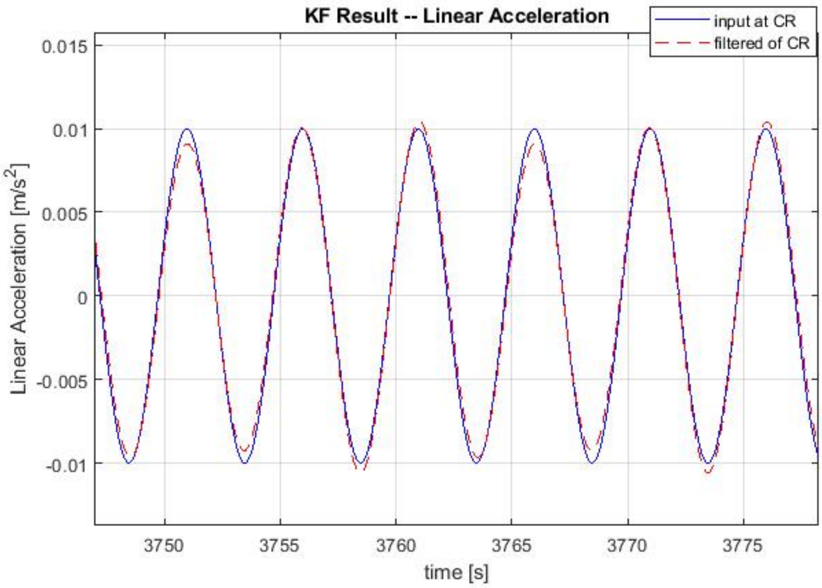

Figure 4.19 Comparison of linear acceleration at CR when $r = 8$ m

Figures 4.13, 4.15, 4.17, and 4.19 show comparisons between the given and estimated a_{CR} values with different settled offsets. The blue and red dashed lines show the given and estimated a_{CR} values, respectively. The estimated a_{CR} has coincident shape and almost identical magnitudes with the given values. However, some noticeable differences in amplitudes appear now and then. The differences would be caused by the oscillations in estimated offset values.

4.5.2 Estimated Results from a Simulated Sea Environment System

This simulated system describes the motions of a floating vessel while it encounters swell and wind sea (Korte, 2017 [80]). The ship model is a crew transfer vessel which has a catamaran hull with a length of 22 m and a breadth of 8.3 m. In this system, it is possible to change the direction, length, and height of all encountered waves, and all related hydrodynamic parameters are given. As shown in Figure 4.20, the black line expresses the trajectory of the floating vessel, which moves from the north to southwest under the encountered waves from the west that can be regarded as bow seas. The colour coding depicts the wave height, which is mostly below 0.5 m.

In the simulation, the encountered waves consist of two swells with different wavelengths of 96 and 180 m. The length and height are fixed, whereas the directions of these two swells are varied during the simulation. Four cases are depicted here, including [0;10], [0;100], [180;10], and [180;100]. These four pairs are the directions of the two swells. For example, the first pair indicates that the first swell comes from 0 degrees, namely directly from the north, and at the bow, with a length of 96 m. At the same time, the second swell comes from 10 degrees away from the north, with a length of 180 m. Therefore, the first case is the combination of bow seas, as depicted in Figure 4.20. The second case is a combination of bow and beam seas. The third case is a combination of bow and following seas, and the fourth case is a combination of beam and following seas.

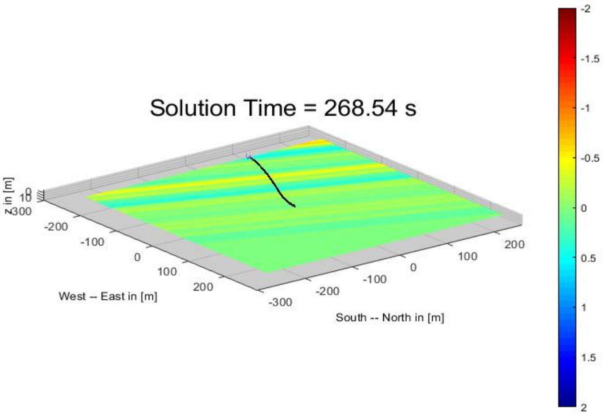

Figure 4.20 Description of floating vessel motion

From this simulated system, the full six DOFs can be obtained. Therefore, when applying the KF, all three linear motions and rotational motions are introduced. As the outputs of this simulated system are positions and angles, several differentials should be utilized to generate the relevant linear accelerations, angular rates, and angular accelerations, along with the filtering process as depicted in Chapter 4.2. As initially defined for this simulated system, the motion centre is the CG of this floating vessel, which is also the origin of the body-fixed frame. Thus, the coordinates of this centre are set to (0,0,0).

Figures 4.21 to 4.24 show the estimated offset results from this simulated system in four different directions of encountered waves but with the same length as depicted before. Figure 4.21 and Figure 4.23 show that the estimated offset values are not stable and do not converge. Usually, bow seas can cause irregular ship motions, resulting in unstable offset estimations, as shown in Figure 4.21 with pure bow seas. In Figure 4.23, with a combination of a bow sea and following sea, the estimated offset values are not steady owing to the complicated encountered waves. In these two cases, the offset values are relatively similar. In the x-direction, the values are approximately minus six or seven centimetres, in the y-direction, they are only approximately minus one centimetre, and in the z-direction, they are approximately three centimetres. In Figures 4.22 and 4.24, the estimated offset values are more stable than in the other two cases, and they remain at rather similar values with the same signs in the y- and z-direction. The values are approximately minus five centimetres in the y-direction and three centimetres in the z-direction. In the x-direction, a difference on the order of millimetres appears, but this is tolerable with respect to the size of the ship model.

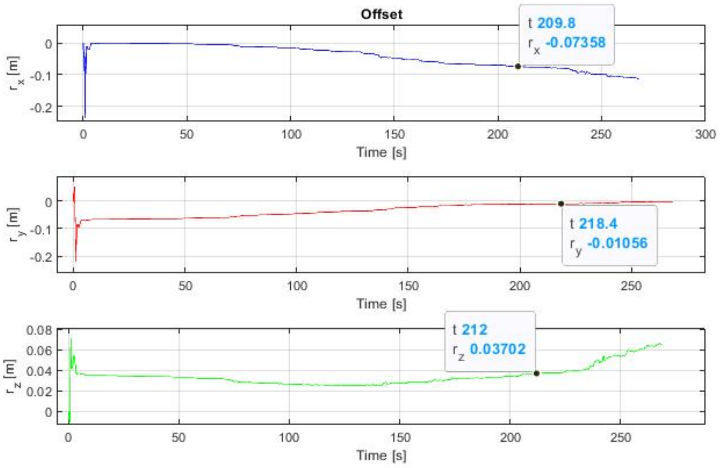

Figure 4.21 Estimated offset of the first case [0;10]

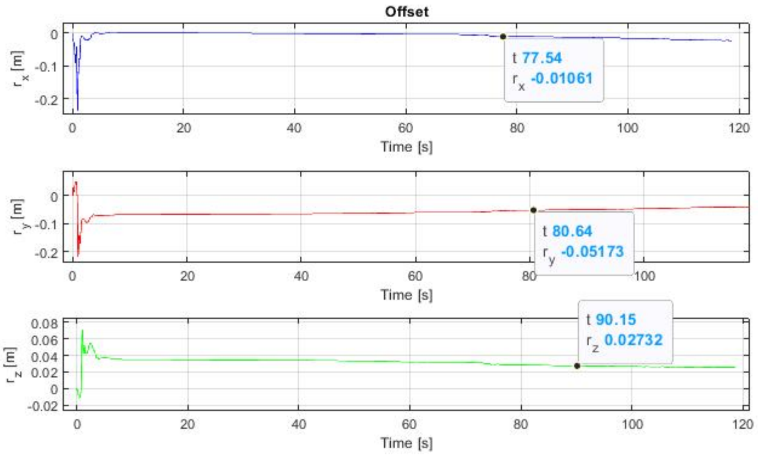

Figure 4.22 Estimated offset of the second case [0;100]

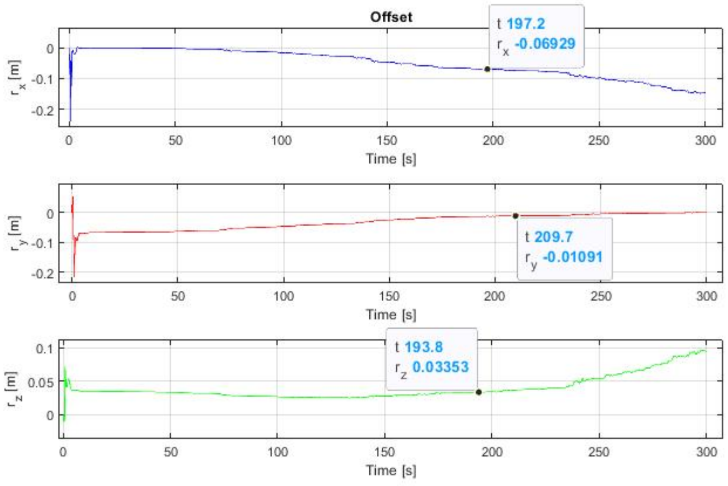

Figure 4.23 Estimated offset of the third case [180;10]

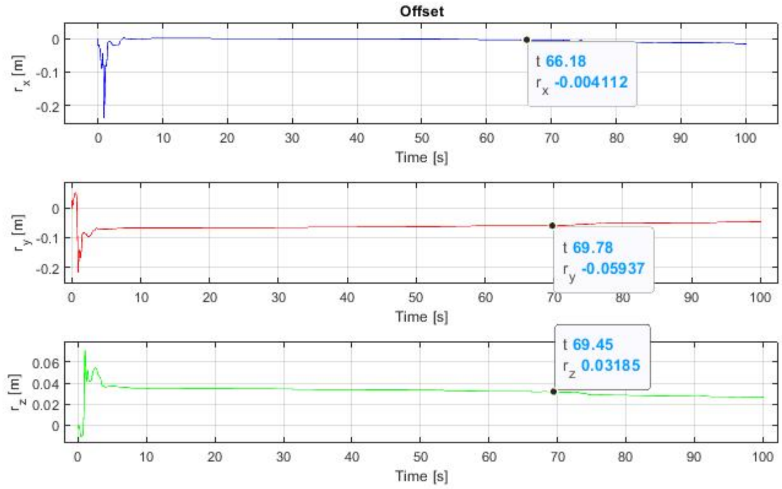

Figure 4.24 Estimated offset of the fourth case [180;100]

In conclusion, the offset values are likely to be determined using this proposed Kalman filter, even under the extreme wave conditions used for this ship model. Significant differences are shown in the x- and y-direction, with deviations of several centimetres, but all these are negative values. The offset values in the z-direction are similar within all these cases. These offset values indicate that the motion centre, defined as the CR for this work, is not fixed to a specific location but moves within a particular range. By comparing with the location of the given CG, namely the origin, the estimated offset values have yielded a possible location of the CR. This location is a few centimetres behind the CG in the longitudinal direction, several centimetres to the starboard side of the CG in the transverse direction, and approximately three centimetres above the CG in the vertical direction. The differences between the estimated offset and the given CG on the order of centimetres are tolerable with respect to the size of the simulated ship model.

Comparing the estimated offset results for these two simulated models, it appears that the CR's location can be determined by the proposed determination algorithm using the Kalman filter. Although the estimated results are not identical to the given condition, they are close to the given values and remain constant after a short time adjustment.

5 Experimental Procedures

In consideration of improved verification and to ensure wide practical applicability, several ships have been employed in this research, ranging from a small boat to a large icebreaker ship. Moreover, for the sake of obtaining more accurate motion data, identical sensor boxes have been used in totally different water areas, such as a river, the coastline of the North Sea, and the Antarctic. In this chapter, the essential characteristics of all the relevant ships are described in detail, and the entire process of implementing the experiments is addressed as well. To guarantee the accuracy and stability of the experimental results, multiple trials were implemented under a similar experimental environment, including fixed and stable ship velocities, similar encountered waves, fixed heading angles, and identical water areas.

5.1 Introduction of Ships

Here, the basic characteristics of all the employed ships are introduced, including their length, width, draught, displacement, and maximum velocity. All the information is based on the stability booklets of the respective ships.

5.1.1 Marvin

Marvin is a small research boat from the Jade University of Applied Science in Germany. It is usually used as a teaching and research assistant vessel. Figure 5.1 shows the Marvin floating at a dock alongside the river Hunte, and Table 5.1 shows the basic properties of the Marvin.

Figure 5.1 Marvin

Name	Symbol	Quantity	Unit
Overall length	L	6.7	m
Breadth	B	2.4	m
Draft	T	0.5	m
Displacement	D	3.5	t
Maximum ship velocity	v	17	kn

Table 5.1 Marvin loading conditions

5.1.2 Fathom 10

Fathom 10 is a training vessel that is slightly larger than the Marvin. It belongs to the Maritime Department of the Cape Peninsula University of Technology (CPUT) in Cape Town, South Africa. It used to be a fishery patrol boat, but now serves teaching and research purposes for the university. Figure 5.2 shows the vessel in a dry dock and Table 5.2 lists the properties of the Fathom 10.

Figure 5.2 Fathom 10

Name	Symbol	Quantity	Unit
Overall length	L	19.6	m
Length between perpendiculars	L_{pp}	17.61	m
Breadth	B	5.0	m
Draft	T	1.64	m
Displacement	D	56.6	t
Vertical position of centre of gravity, measured from keel	KG	1.97	m
Maximum ship velocity	v	13.5	kn

Table 5.2 Fathom 10 loading conditions

5.1.3 RV Simon Stevin

RV Simon Stevin is a multidisciplinary research vessel deployed for coastal and oceanographic research in the Southern Bight of the North Sea and the eastern part of the English Channel. It is also a training platform for students devoted to marine science and maritime studies, and it serves as a test platform for new marine technologies. Figure 5.3 shows a photograph of Simon Stevin on duty in the sea [84] and Table 5.3 illustrates the basic properties of the vessel.

Figure 5.3 RV Simon Stevin

Name	Symbol	Quantity	Unit
Length between perpendiculars	L_{pp}	32.1	m
Breadth	B	9.4	m
Draft	T	3.55	m
Deadweight (summer)	D	80	t
Vertical position of centre of gravity, measured from keel	KG	4.18	m
Maximum ship velocity	v	12	kn

Table 5.3 Simon Stevin loading conditions

5.1.4 S. A. Agulhas II

The Agulhas II is a South African icebreaking polar supply and research ship, and it was designed to both carry out scientific research and supply South African research stations in the Antarctic. Figure 5.4 shows the Agulhas II on one of her voyages in the polar region [85], and Table 5.4 shows its basic properties in detail.

Figure 5.4 Agulhas II

Name	**Symbol**	**Quantity**	**Unit**
Overall length	L	134.0	m
Length between perpendiculars	L_{pp}	121.25	m
Breadth	B	22.0	m
Draft	T	7.65	m
Displacement	D	13687	t
Vertical Position of centre of gravity, measured from keel	KG	8.9	m
Maximum ship velocity	v	16	kn

Table 5.4 Agulhas II loading conditions

5.1.5 Catamaran Willi

The catamaran Willi was designed and constructed by the Jade University of Applied Science under a project, and it was applied in this research to test the proposed algorithm to find the location of CR. The conditions and performance of Willi can be regarded as a simulated model, and its CG location is assured when constructed. Hence, the location of the CR is easily determined. Furthermore, the motion data would lend itself to more precise analysis without any undesired factors from the ship itself. The Willi was placed in a basin and then in a yacht harbour. Therefore, both simulated and practical motion data could be generated by the sensor box installed onboard to verify the accuracy of the estimated results, which is regarded as a good example and verification of the determination algorithm.

The Willi is a small catamaran equipped with propellers and motors on both the port and starboard sides. Therefore, the propulsion system can be replaced with these two models when implementing the experiment. The two ship bodies are connected by a metal platform, on which a power supply and measurement devices can be placed. As shown in Figure 5.5, the power supply of Willi is positioned on the lower part of the platform, while the sensor box occupies the upper part of the platform, along with an IMU equipped with a GPS module and a wireless router that transmits the measured data to a specific cloud server. Figure 5.6 illustrates the general structural details of the Willi, the regular draft of which is approximately 20 cm.

Figure 5.5 Willi in the basin

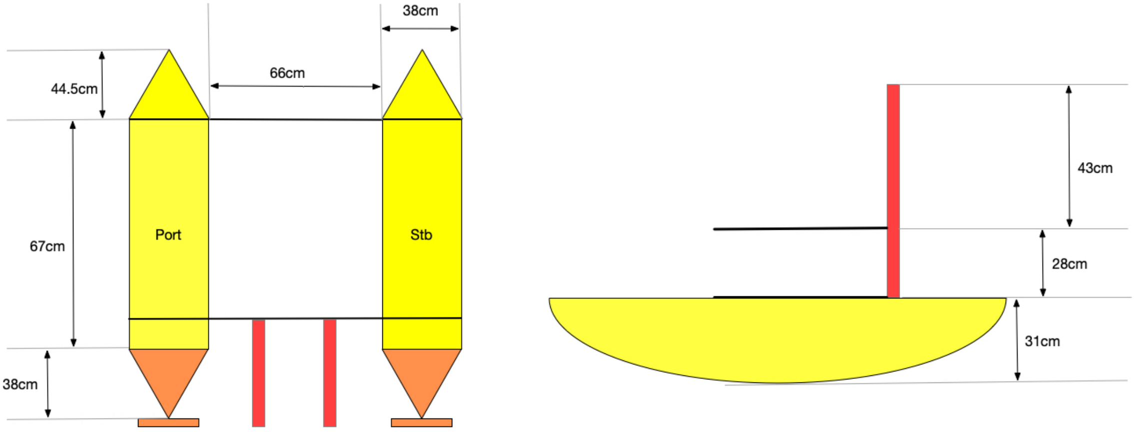

Figure 5.6 Description of Willi’s structure

5.2 Experimental Conditions

The processes for each experiment carried out on every ship are described in the following, including the current sea environment, velocity and heading angles of the ship, and placement of the sensor boxes.

5.2.1 Marvin at the Hunte River

The sensor installed on the Marvin was a small IMU composed of a triple gyroscope and a triple accelerometer to generate angular rates and linear accelerations in three dimensions, respectively. First, this sensor was fixed horizontally on a plane to test and calibrate its static characteristics, such as its internal noise and bias. Second, it was tied to a pendulum in the laboratory to observe its rotational performance. Eventually, it was installed and fixed properly on the Marvin for measuring and recording the ship motion data, at two different locations onboard: one was inside the ship, as shown in Figure 5.7 (left), approximately 1.2 m above the keel, and the other was on the top of the ship, as shown in Figure 5.7 (right), approximately 1.95 m above the keel.

During the experiments, the Marvin was first parked at the dock and moved freely without any manual forces. Then, it was driven into the middle of the river Hunte to carry out a few short voyages. It drifted in the current caused by other large cargo ships passing by in the river. Finally, with a speed of 4.5 or 5 kn, the Marvin was steered along the river course back and forth several times to complete the manoeuvring part or this experiment.

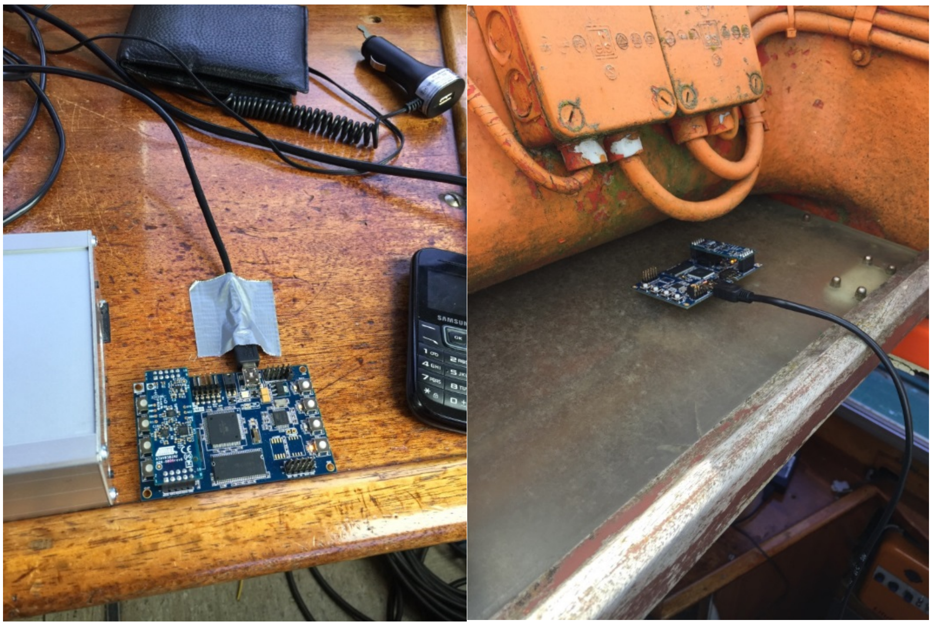

Figure 5.7 Sensor onboard: inside the ship (left), on top of ship (right)

5.2.2 Fathom 10 at Cape Town

The experiments were performed in the open water to the west of Cape Town in February 2014 and February 2015. In 2014, the waves were coming from the peak direction of 225° from the north with a peak period of 12 s, and the peak height was about 2.0 m. While in 2015, the waves' peak direction was approximately 220° from the north with a peak period and peak height of 11 s and 2.3 m, respectively.

Motion data were recorded using a sensor box placed laterally close to the ship's estimated CG with its axes aligned with the ship's body-fixed frame. The relative position between the sensor box and the CG is shown in Figure 5.9. Figure 5.8 shows the sensor box placed at the right edge of the table. Data were sent to a serial interface and recorded on a micro-SD memory card. The accelerometers and gyros integrated in an IMU inside the sensor box provided linear accelerations in three dimensions and angular rates around the x- and y-axis. The experiments were carried out with a settled sampling rate at 10 Hz. The motion data were recorded while the vessel sailed at a velocity of 7.5 kn and maintained a constant heading angle against the encountered waves; each trial lasted approximately 15 min and was repeated several times to obtain more stable data. Ultimately, a series of similar experiments were performed under similar conditions but at different heading angles.

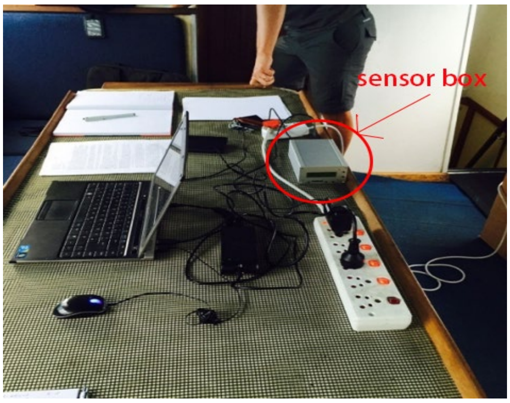

Figure 5.8 Sensor box on working desk

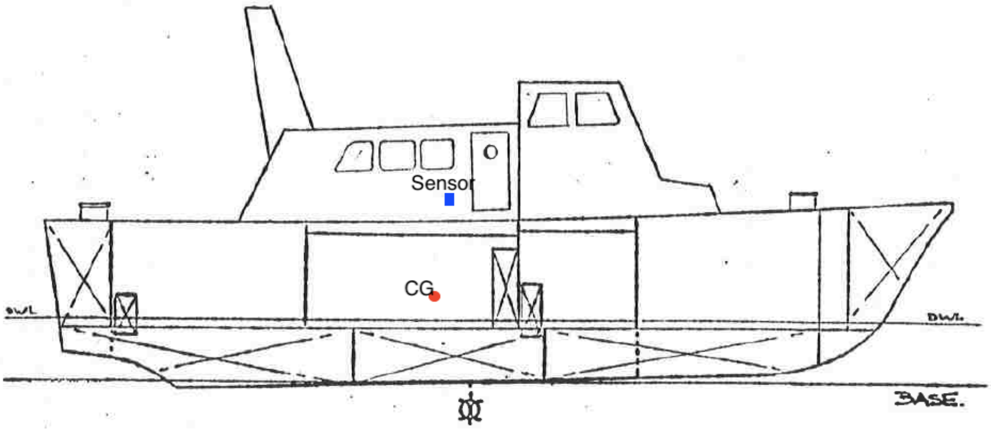

Figure 5.9 Sensor box onboard Fathom 10

5.2.3 Simon Stevin at Ostend

The experiments were performed during two different periods, from 1st to 3rd August 2017 and from 6th to 8th November 2017. Both experiments were implemented in Belgian water near

Ostend. The water depth in the operational area was generally greater than 20 m, except for a few sandbanks, where the water depth could be approximately 12 m. When the ship was fixed at a constant moving speed and a stable heading, the experiments were performed, and each trial lasted for 30 min. The wave buoys nearby provided sea state data of the operational water area. There were several sensors on board, but only two sensors were used, as shown in Figure 5.10; one was on the bridge and the other was in the survey room. Both were equivalent in type to sensor II, and provided linear accelerations and angular rates in three dimensions.

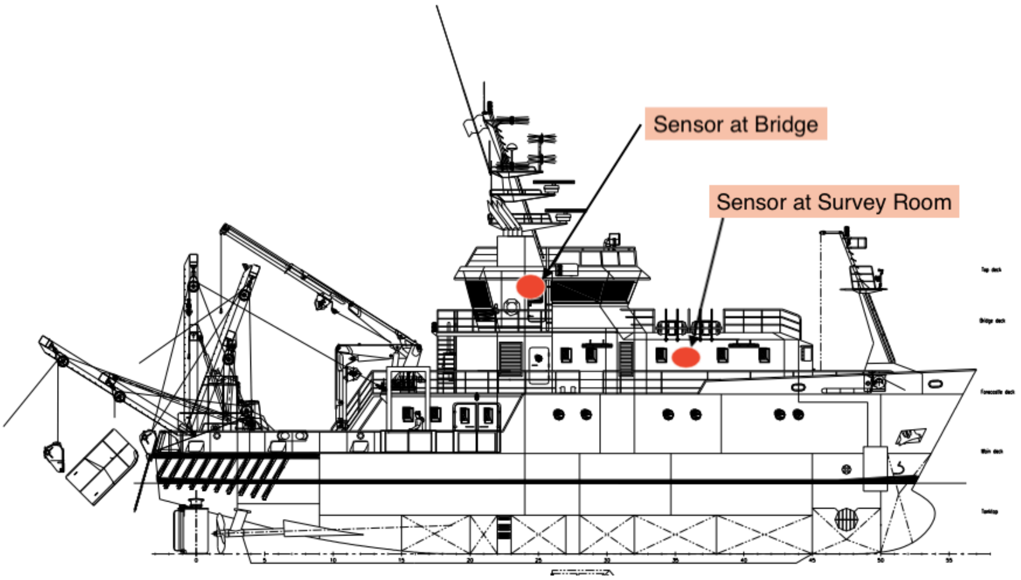

Figure 5.10 Sensor box onboard Simon Stevin

(Diagram from [84], legend by the author)

5.2.4 Agulhas II at Antarctic

The measurements were performed during her voyage from Cape Town to the Antarctic and back to Cape Town from 28th June to 12th July in 2017. Sensor boxes with low-cost gyros and accelerometers installed onboard recorded the whole ship motions autonomously, as described in Chapter 4.1. The two sensor boxes were installed on the vessel as shown in Figure 5.11; sensor I was placed in the engine room within 2 m from the estimated CG, and sensor II was placed on the observation deck above the navigation bridge. Furthermore, sensor II provided accurate date and time information, along with the position tags using its GPS module.

The datasets to be analysed were obtained during the procedures. The ship moved forward with a steady heading angle, with a relatively constant velocity, and then sailed for several hours. As her voyage lasted for approximately half a month, the experiments were able to be performed and repeated quite often. The wave information was provided by visual observations recorded by the

South African weather service meteorologists on board, and the estimated wind sea was negligible.

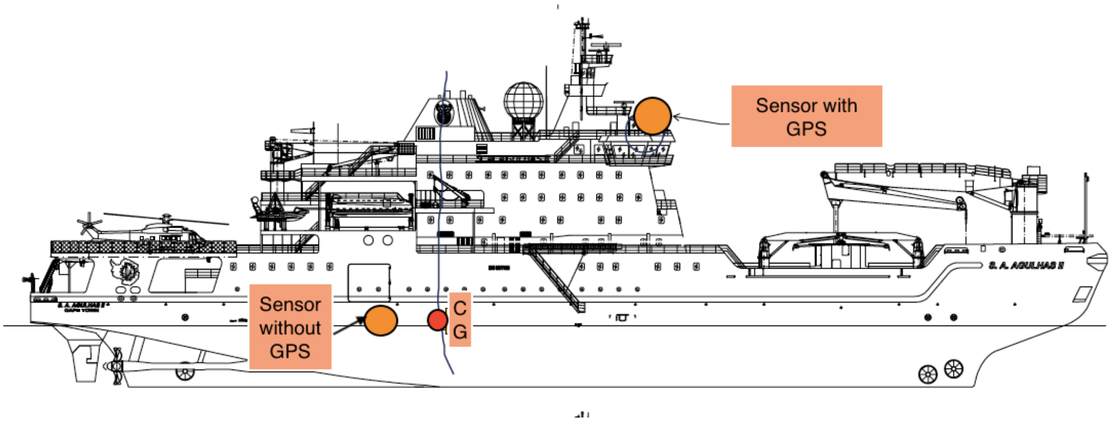

Figure 5.11 Sensor box onboard Agulhas II

(Diagram from (Bekker, 2018 [86]), legend by the author)

5.2.5 Willi in the Manoeuvre Basin

The experiments of the Willi were implemented in two locations. One is the manoeuvring basin at the Jade University of Applied Science, which is considered as a simulated environment with manually generated waves. The other one is at the Yachthafen alongside the river Hunte.

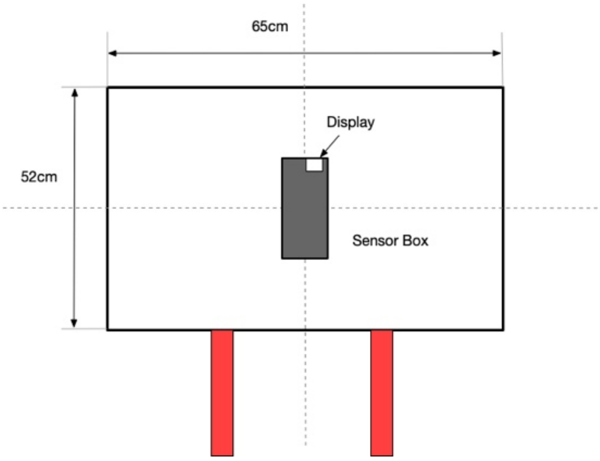

Figure 5.12 Sensor box on Willi

The measurement device installed on the catamaran was sensor II as illustrated in the previous chapter, and the sampling rate was set to 8 Hz. Considering the availability of Willi’s remote controller and the range limitation of the yacht dock, the Willi moved forward no farther than 50 m. Thus, each trial could last for 10 min at most, which essentially allowed approximately 5 min to acquire the appropriate amount of motion data for processing. The sensor box was installed and fixed precisely in the middle zone on the upper part of Willi’s platform, with the edges of the case parallel to the corresponding sides of the platform, as shown in Figure 5.12.

First, the catamaran drove with propellers or rudders in the basin, as shown in Figure 5.13. The total length of the basin is 24 m. Apart from a few facilities, the Willi moved straight ahead for approximately 18 m and then performed turns at a wider part of the basin. The width here is approximately 6 m. No extra waves were introduced here. The water was calm inside the basin, with only echo and wake flow caused by Willi itself. Owing to the limitation of the basin's size, the experiments lasted for only a few minutes, even with multiple repetitions. With the sampling rate of 8 Hz, the size of the motion dataset generated in the basin was insufficient. Thus, a larger experimental site was required.

Figure 5.13 Willi in the manoeuvre basin

5.2.6 Willi at the Yachthafen

As shown in Figure 5.14, the Willi was put into a yacht dock near the university, which is a small water area used for parking private yachts alongside the river Hunte as the experiments were conducted in the winter, the area was empty and an ideal place for performing research experiments. The actual location where the experiments were implemented was close to the bank, with a range of 50 m in width and 80 m in length.

The experiments were carried out in two phases, with the first including making circles by both sides and the second involving moving straight ahead and then turning back to the bank. The catamaran was equipped with propellers and repeated these two phases with the same routes.

Figure 5.14 Willi at the Yachthafen

6 Evaluation of the Results

After implementing the experiments on all ships, the results of the determination algorithm are processed and analysed in this chapter. All the results of the estimated offsets value and ship motions of the implemented experiments on different ships are presented and explored individually. One way to verify the determination algorithm presents itself when precise information about the recorded wave spectra is available from other researchers, which is to compare the current wave information with that estimated by the ship motion calculated from the KF. Another method to test the determination algorithm is to compare the results among actual-sized ships and the model catamaran Willi, which is essentially to compare real-world and experimental scenarios. This chapter evaluates the errors from the applied sensor boxes and the calculation process, especially for the Kalman filter, to assess the accuracy of the estimated location of the CR and the feasibility of the method proposed in this work.

6.1 Results of Marvin

The results of estimated offset values and their evaluations for Marvin are presented in this part. As shown in the following figures, the trials are named after their sequences. According to the experimental record, the sensor box was located slightly to the starboard side on the desk but in the centre along the ship's length and was 1.2 m above the keel. Moreover, the other location of the sensor box, on top of the cabin, was on the middle transverse line of the ship, approximately 4 m behind the bow and 1.95 m above the keel.

6.1.1 Analyses of Several Trials

Figures 6.1 to 6.4 express the estimated offsets from the trials when the sensor box was on the desk. As shown in the figures, after a period of oscillation, a relatively short time is needed to reach the appropriate range of values, and then the results become constant in the final phase, especially in y- and z-direction. However, among all these figures, the results of Figure 6.1 and Figure 6.2 show more oscillations in the x-direction than the others, because these two trials were under the condition of sudden but non-persisting shaking movements from the ship. Hence, there are a few significant adjustments initially, and then with the reduction in amplitude, the estimated offsets begin to converge. On the contrary, trials four and seven consisted of continuous and manual shaking movements. The estimated offsets in the x-direction showed oscillation and tuning within a narrow range affected by stable and persistent ship movements, as shown in Figure 6.3 and Figure 6.4.

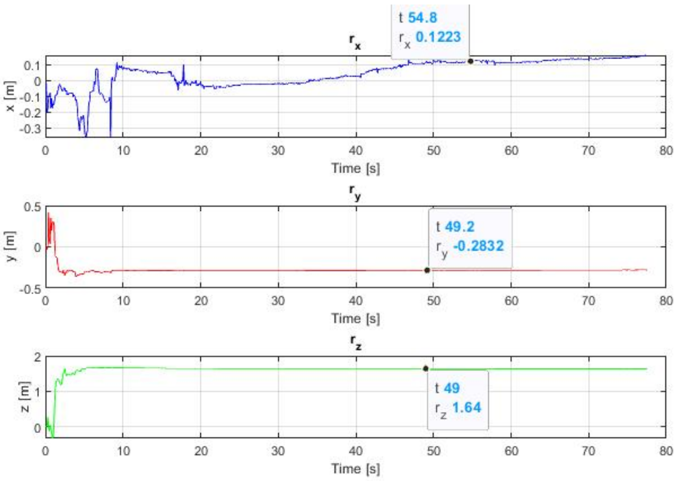

Figure 6.1 Estimated offsets of trial two

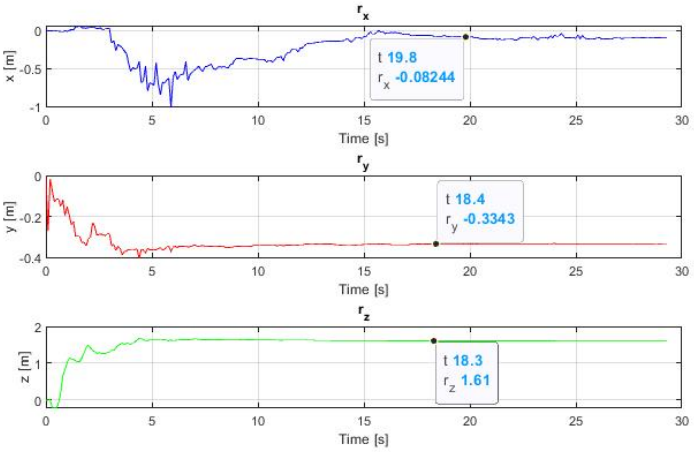

Figure 6.2 Estimated offsets of trial five

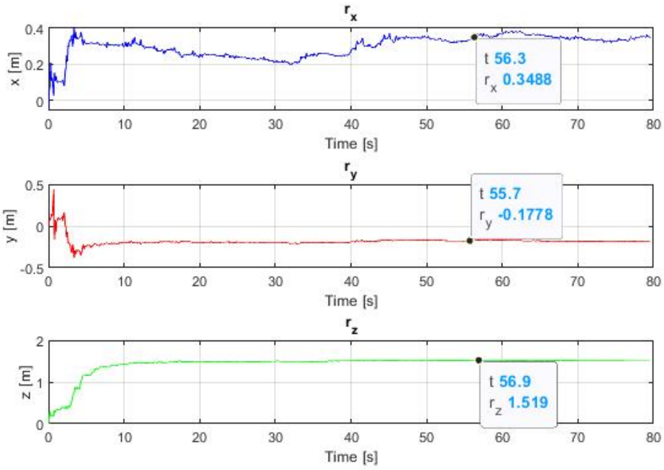

Figure 6.3 Estimated offsets of trial four

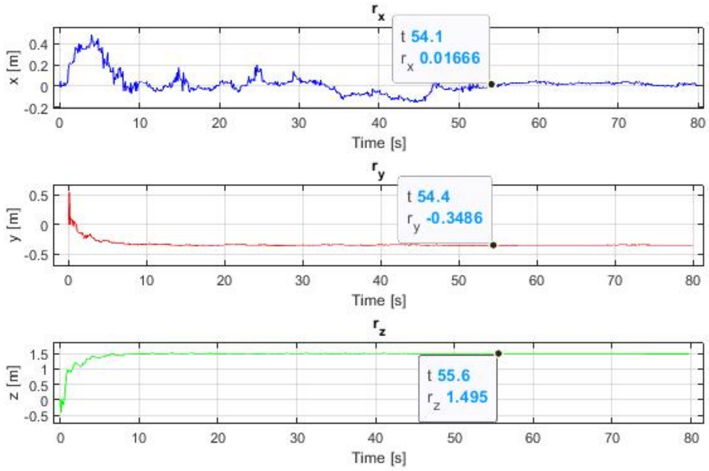

Figure 6.4 Estimated offsets of trial seven

The values marked in the figures are randomly selected from their relatively stable phases, in an attempt to indicate the probable data range of offsets in all three dimensions. As shown in the figures, r_z is relatively stable, and the distance between the CR and sensor on the desk is approximately 1.6 m. r_y has slightly wider range, from 20 to 35 cm; that is, the sensor is on the starboard side of the CR. However, the values for r_x have changed significantly; it is possible that the results are influenced by the different ship behaviours or their amplitudes.

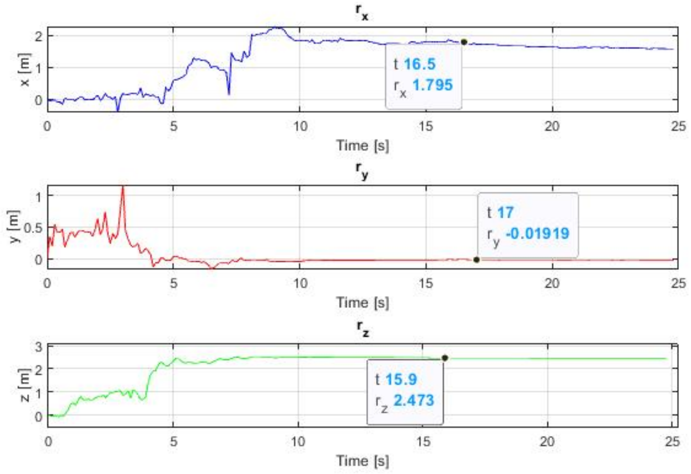

Figure 6.5 Estimated offsets of trial nine

The estimated offset values generated by the sensor box on top of the cabin are illustrated in Figure 6.5 to Figure 6.7; again, the first two figures are affected by sudden movements and Figure 6.7 describes the results of a continuous ship motion. For these three trials, in the x-direction, the offset values seem to be more adjustable. They eventually converged after a longer tuning time but with relatively large deviations among these three trials. r_y and r_z are relatively stable as the corresponding results from the desk. Slight differences among all three trials have appeared, both in the y- and z-direction, which require shorter tuning time before the curves become stable.

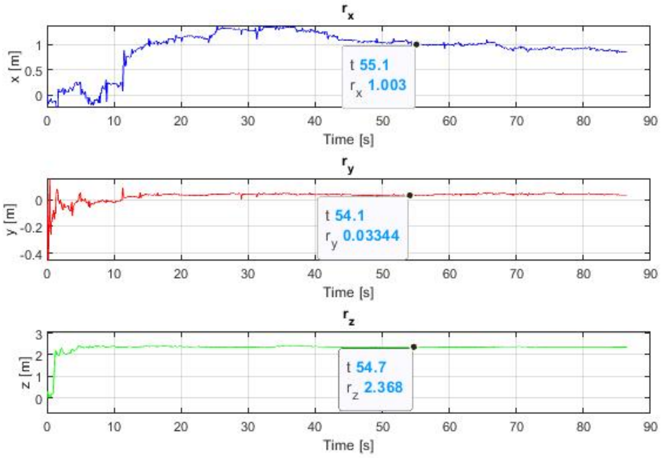

Figure 6.6 Estimated offsets of trial ten

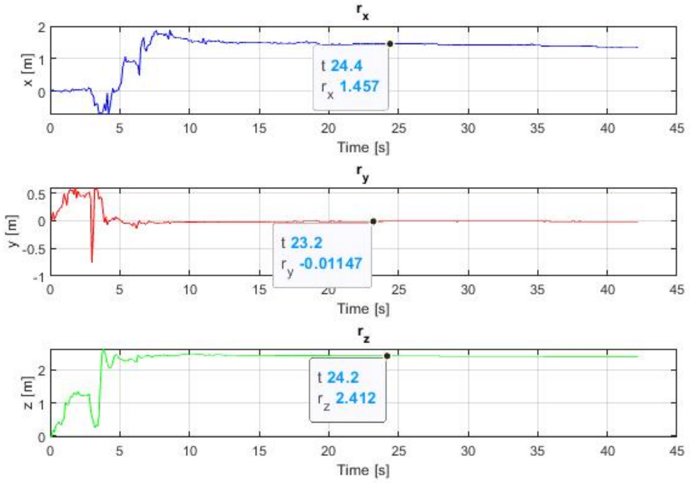

Figure 6.7 Estimated offsets of trial eleven

The evaluations of these estimated offsets results are based on the *P* matrix produced in the Kalman filter process, as illustrated in Chapter 4.4. The *P* matrix is defined as a 6*6 matrix describing the error covariances of the state vector $[ax_n, ay_n, az_n, r_x, r_y, r_z]^T$ specifically for this work. As shown in the following, *P2* is the matrix is generated by trial two, *P5* is the matrix from trial five, and so forth. The order of the rows and columns is in the same sequence as the state vector. For instance, the component located at the second row and the second column is the estimated linear acceleration error in the y-direction. According to the setting of the *P* matrix, as an identity matrix, most of the non-zero values should occur on the main diagonal. The remaining elements are zero, indicating that there are no correlations among the corresponding variables. However, judging from the location, the value of -0.003 indicates that the linear acceleration in the z-axis is anti-correlated with the offset in the x-direction, while the value of 0.025 means that the offset in the y-direction is correlated with the offset in the x-direction. Based on the correlation and units of all components in the *P* matrix, the *P* matrix can be divided into four parts with four different units, as shown in the following.

The magnitudes of the values are essentially the square of the corresponding errors according to the definition of the covariances and the *P* matrix. The initial values are 0.5, rather large as compared to the amplitudes of the variables. Nevertheless, the component values of the produced *P* matrix are comparatively smaller but more reasonable. For example, among all the presented *P* matrices, the errors for the linear accelerations are 0.01 m/s^2. On the contrary, take trial two as an example for the offset. The errors of the offset in each direction are approximately 0.209, 0.035, and 0.032 m, respectively. These errors affect the values of the offset. Hence, the final estimated results are different after comparing the *P* matrix for each trial.

$$P\,2 = 10^{-4} * \begin{bmatrix} 1 & 0 & 0 & \vdots & 0 & 0 & 0 \\ 0 & 1 & 0 & \vdots & 0 & 0 & 0 \\ 0 & 0 & 1 & \vdots & -3 & -1 & 0 \\ \cdots & \cdots & \cdots & \vdots & \cdots & \cdots & \cdots \\ 0 & 0 & -3 & \vdots & 437 & 25 & 0 \\ 0 & 0 & -1 & \vdots & 25 & 12 & 0 \\ 0 & 0 & 0 & \vdots & 0 & 0 & 10 \end{bmatrix} \begin{bmatrix} [(m/s^2)^2] & [m^2/s^2] \\ [m^2/s^2] & [m^2] \end{bmatrix}$$

Trials two and five encountered similar forces. However, apart from the first three values in the diagonal line and the technical zeros, the other values are not similar at all. These values are one reason that the final estimated offset is not identical. Overall, the offset in the x- and y-direction are slightly correlated with the linear acceleration in the z-direction, and they are mutually correlated simultaneously. The errors of the offset in the x-direction are much larger than in the other directions.

$$P\,5 = 10^{-4} * \begin{bmatrix} 1 & 0 & 0 & \vdots & 0 & 0 & 0 \\ 0 & 1 & 0 & \vdots & 0 & 0 & 0 \\ 0 & 0 & 1 & \vdots & 2 & 0 & 0 \\ \cdots & \cdots & \cdots & \vdots & \cdots & \cdots & \cdots \\ 0 & 0 & 2 & \vdots & 1913 & 4 & 0 \\ 0 & 0 & 0 & \vdots & 4 & 8 & 0 \\ 0 & 0 & 0 & \vdots & 0 & 0 & 8 \end{bmatrix} \begin{bmatrix} [(m/s^2)^2] & [m^2/s^2] \\ [m^2/s^2] & [m^2] \end{bmatrix}$$

Another factor in evaluating the *P* matrix is the correlation coefficient, a numerical measure to illustrate the statistical relationship between the two variables, which a built-in function in MATLAB can directly calculate (Taylor, 1997 [87]) [88]. This correlation coefficient provides a much clearer understanding of the relationship between the linear accelerations and offsets. In the following matrix *CC2*, CC stands for 'correlation coefficient' and 2 is the trial number; *CC5* is defined similarly. All the values on the diagonal line are one because they are self-referential. The off-diagonal values below 0.5 can be regarded as weakly correlated, while the values closer to one indicate that the two corresponding variables are more strongly correlated. *CC2* indicates that the linear acceleration in the z-direction has strong correlations with the offset in the x- and y-direction. In *CC5*, a strong correlation appears only in linear acceleration in the z-direction and the offset in the x-direction.

$$CC\ 2 = \begin{bmatrix} 1.0000 & -0.2774 & 0.1495 & -0.2141 & -0.2908 & -0.1659 \\ -0.2744 & 1.0000 & 0.2112 & -0.2982 & -0.4009 & 0.2543 \\ 0.1495 & 0.2112 & 1.0000 & -0.9318 & -0.9382 & 0.1587 \\ -0.2141 & -0.2982 & -0.9318 & 1.0000 & 0.9111 & -0.2230 \\ -0.2908 & -0.4009 & -0.9382 & 0.9111 & 1.0000 & -0.2989 \\ -0.1659 & 0.2543 & 0.1587 & -0.2230 & -0.2989 & 1.0000 \end{bmatrix}$$

$$CC\ 5 = \begin{bmatrix} 1.0000 & -0.2523 & -0.2514 & -0.1983 & -0.2877 & -0.2160 \\ -0.2523 & 1.0000 & -0.3236 & -0.2559 & -0.3686 & 0.0688 \\ -0.2514 & -0.3236 & 1.0000 & 0.9067 & 0.1308 & -0.2694 \\ -0.1983 & -0.2559 & 0.9067 & 1.0000 & 0.3506 & -0.2147 \\ -0.2877 & -0.3686 & 0.1308 & 0.3506 & 1.0000 & -0.3030 \\ -0.2160 & 0.0688 & -0.2694 & -0.2147 & -0.3030 & 1.0000 \end{bmatrix}$$

Trials four and seven encountered similar continuous external forces, but the error results are not identical either. However, the errors for the three linear accelerations are identical, and they both have a larger error of the offset in the x-direction. The correlations appear between linear acceleration in the z-direction and the offset on the x- and y-direction. Furthermore, the offset in the x- and y-direction is correlated with each other as well. The error magnitudes for the offset are approximately 0.195 m in the x-direction, 0.044 m in the y-direction, and 0.02 m in the z-direction for trial four. On the contrary, for trial seven, these are 0.35 m in the x-direction and 0.022 m in both the y- and z-direction. The correlation coefficients of trials four and seven are similar, as shown in *CC4* and *CC7*. Strong correlations are shown in the linear acceleration in the z-direction and the offset in the x- and y-direction. These are consistent with the error covariance matrices.

$$P\ 4 = 10^{-4} * \begin{bmatrix} 1 & 0 & 0 & \vdots & 0 & 0 & 0 \\ 0 & 1 & 0 & \vdots & 0 & 0 & 0 \\ 0 & 0 & 1 & \vdots & -11 & -2 & 0 \\ \cdots & \cdots & \cdots & \vdots & \cdots & \cdots & \cdots \\ 0 & 0 & -11 & \vdots & 382 & 75 & 0 \\ 0 & 0 & -2 & \vdots & 75 & 19 & 0 \\ 0 & 0 & 0 & \vdots & 0 & 0 & 4 \end{bmatrix} \begin{bmatrix} [(m/s^2)^2] & [m^2/s^2] \\ [m^2/s^2] & [m^2] \end{bmatrix}$$

$$CC4 = \begin{bmatrix} 1.0000 & -0.2408 & 0.2140 & -0.2449 & -0.2595 & -0.0001 \\ -0.2408 & 1.0000 & 0.1666 & -0.1871 & -0.1966 & -0.3921 \\ 0.2140 & 0.1666 & 1.0000 & -0.9968 & -0.9950 & 0.2097 \\ -0.2449 & -0.1871 & -0.9968 & 1.0000 & 0.9982 & -0.2356 \\ -0.2595 & -0.1966 & -0.9950 & 0.9982 & 1.0000 & -0.2477 \\ -0.0001 & 0.2543 & 0.2097 & -0.2356 & -0.2477 & 1.0000 \end{bmatrix}$$

$$P\,7 = 10^{-4} * \begin{bmatrix} 1 & 0 & 0 & \vdots & 0 & 0 & 0 \\ 0 & 1 & 0 & \vdots & 0 & 0 & 0 \\ 0 & 0 & 1 & \vdots & -12 & 0 & 0 \\ \cdots & \cdots & \cdots & \vdots & \cdots & \cdots & \cdots \\ 0 & 0 & -12 & \vdots & 1206 & 5 & 0 \\ 0 & 0 & 0 & \vdots & 5 & 5 & 0 \\ 0 & 0 & 0 & \vdots & 0 & 0 & 5 \end{bmatrix} \begin{bmatrix} [(m/s^2)^2] & [m^2/s^2] \\ [m^2/s^2] & [m^2] \end{bmatrix}$$

$$CC7 = \begin{bmatrix} 1.0000 & -0.1670 & 0.1848 & -0.2093 & -0.3451 & -0.1216 \\ -0.1670 & 1.0000 & 0.1210 & -0.1366 & -0.2215 & -0.4698 \\ 0.1848 & 0.1210 & 1.0000 & -0.9975 & -0.6194 & 0.1692 \\ -0.2093 & -0.1366 & -0.9975 & 1.0000 & 0.6243 & -0.1912 \\ -0.3451 & -0.2215 & -0.6194 & 0.6243 & 1.0000 & -0.3113 \\ -0.1216 & -0.4698 & 0.1692 & -0.1912 & -0.3113 & 1.0000 \end{bmatrix}$$

$$P\,9 = 10^{-4} * \begin{bmatrix} 1 & 0 & 0 & \vdots & 0 & 0 & 0 \\ 0 & 1 & 0 & \vdots & 0 & 0 & 0 \\ 0 & 0 & 1 & \vdots & 6 & 1 & 0 \\ \cdots & \cdots & \cdots & \vdots & \cdots & \cdots & \cdots \\ 0 & 0 & 6 & \vdots & 593 & 14 & 0 \\ 0 & 0 & 0 & \vdots & 14 & 6 & 0 \\ 0 & 0 & 0 & \vdots & 0 & 0 & 6 \end{bmatrix} \begin{bmatrix} [(m/s^2)^2] & [m^2/s^2] \\ [m^2/s^2] & [m^2] \end{bmatrix}$$

$$CC9 = \begin{bmatrix} 1.0000 & -0.0734 & -0.2478 & -0.1960 & -0.2781 & -0.2375 \\ -0.0734 & 1.0000 & -0.1352 & -0.1062 & -0.1523 & -0.5734 \\ -0.2478 & -0.1352 & 1.0000 & 0.9862 & 0.9194 & -0.2449 \\ -0.1960 & -0.1062 & 0.9862 & 1.0000 & 0.9173 & -0.1952 \\ -0.2781 & -0.1523 & 0.9194 & 0.9173 & 1.0000 & -0.2736 \\ -0.2375 & -0.5734 & -0.2449 & -0.1952 & -0.2736 & 1.0000 \end{bmatrix}$$

P9 presents the errors of trial nine, in which the sensor was placed on the top of the ship. The values show a similar pattern of this trial to that of the other trials, in which the sensor was in the cabin. The error covariances of the linear accelerations are the same. Moreover, the correlations are similar to those of the former trials, whereby strong correlations appear among the linear acceleration in the z-direction and the offset in x- and y-direction, and only the values are different.

Among all selected *P* matrices above, the correlations are relatively clear and plausible because the offset in the x- and y-direction are the factors that contribute to the linear acceleration in the z-direction. The more significant errors occurred in the x-direction of the offset, indicating that this variable would change more than others, allowing a greater probability of obtaining unusual or outlying values.

6.1.2 Analyses of the Complete Results

Table 6.1 expresses the estimated offsets directly for Marvin. Namely, it describes the information about the distances between the CR and onboard sensor. Trials one to seven were implemented when the sensor box was on the desk in the cabin, and the other trials were performed when the sensor was on the top of the cabin. As depicted earlier in the *P* matrix, differences of a few centimetres are acceptable for the offset in the y- and z-direction. However, for the x-direction, the errors are much larger at approximately 0.2 m. Therefore, greater oscillations in this value would be estimated and predicted.

First, as illustrated before, the sensor box on the desk was 1.2 m above the keel, while that on top of the cabin was 1.95 m above the keel. When judging from the table, all the r_z values are out of range of the ship, although they vary among the trials. Based on the experimental process, however, these values are possible to obtain. The descriptions of the sudden shaking or continuous shaking in the former part were all generated manually, which means the ship was subjected to external forces from only one side to roll in the water. With such sudden and extreme forces, the ship was moved quite obviously under such unbalanced movements, and then the CR could be out of the range of the ship. Similarly, when the ship experiences extreme weather or encountered waves, the amplitude is larger than normal, and thus the centre is abnormal as well.

The results of r_z obtained from two different placements of the sensor box are compared, with trial one to trial seven corresponding to the sensor on the desk, and the others corresponding to the sensor on top of the cabin. As measured in the experiments, the vertical distance between the two installation locations was 0.75 m. From the results shown in Table 6.1, the average value of r_z estimated from the sensor on the desk is 1.58 m, and the mean value from the sensor on the top is approximately 2.43 m. Therefore, the distance between them is approximately 0.85 m, which is acceptable and credible on account of the experimental conditions and manual measurement errors, and possibly differences introduced by averaging the estimated results.

The estimated r_y is relatively stable in both installation locations, and as illustrated before, the sensor on the desk was slightly closer to the starboard than that on the top. Thus, the average value of r_y estimated from the desk is 0.29 m from the centre, and that estimated from the top is only 0.02 m away from the central line. In general, the r_y estimated from the top and desk sensor is relatively stable among all cases, apart from trial four. For trial four, it is evident that the estimated r_z is also smaller than that in other cases, but when comparing with a similar case of trial seven, the values of r_z are similar. Nevertheless, there are still significant differences in the x- and y-direction for these two cases. After analysing the curves, the r_x of trial four seems to be unstable. It is still in the process of adjusting and thus generating a rather strange value of r_x.

The estimated values of r_x oscillate with a wide range. As shown in the P matrix, the most significant error covariances appeared in this variable, which could lead to unstable and widely varied values. The most probable explanation of these varying results would be the external forces used to generate the ship movements for each trial. As described previously, rather than being caused by waves in the river, these forces were generated manually. Hence, the magnitudes of the forces applied for each trial would be diverse, leading to uneven and possibly irregular ship movements. Furthermore, the most part subjected to the most significant forces was the bow. Thus, the surge, sway, and roll motions would be entirely coupled and strongly correlated, leading to consequent difficulties in analysing the respective motions. They would relate to each other even at small angles. Therefore, it is quite hard to separate them approximately, and thus the estimated offsets value would be affected by coupled motions, especially in the x-direction.

According to the values described in Table 6.1, the location of CR can be approximately determined. The CR's location in the x-direction is close to the bow. The estimated offset values in the x-direction are primarily in front of the sensor box along the longitudinal line, even with an uncertain distance. In the y-direction, the CR's location is quite close to the place where the sensor was installed on top along the transverse line and at the portside of the desk. Finally, in the z-direction, the CR position is beyond the ship under the water, slightly lower than the keel. That is to say, the CR is located at the mid-ship but in the water immediately below the keel.

Trial No.	**r_x [m]**	**r_y [m]**	**r_z [m]**
1	0.34	-0.29	1.55
2	0.08	-0.29	1.64
3	0.36	-0.26	1.63
4	0.35	-0.18	1.51
5	-0.08	-0.33	1.61
6	-1.61	-0.33	1.62
7	0.01	-0.35	1.49
8	1.18	0.01	2.43
9	1.72	-0.02	2.48
10	0.98	0.04	2.37
11	1.44	-0.01	2.41
12	0.49	-0.03	2.46
13	0.42	-0.02	2.41

Table 6.1 Offsets results of Marvin

In conclusion, the first attempt to use the determination algorithm to ascertain the location of CR is successful on account of the stable and narrow range of the location information in the y- and z-axis. Moreover, the adjusting time needed for all cases is rather short compared to the experimental duration, which only lasts for a few seconds. However, owing to the limited external conditions when implementing experiments, there are a few disturbances in the direction of the x-axis. Thus, all three dimensions of the CR locations cannot be precisely determined as previously expected. Hence, the surrounding environment and conditions when conducting the experiments should be set up more carefully and systematically, and should be well-recorded. In addition, the size of the ship may be a reason for generating strange values of r_x, as the value of r_z is always out of the ship, which is an unusual situation in real-world scenarios. This value would certainly affect the surge and sway motion, and further impact the offset in the other directions.

6.2 Results of Fathom 10

A few sea trials are analysed in this part, and the Kalman filter is utilized to estimate the offset values. Based on the estimated offsets and ship motions at the CR, the wave characteristics can also be obtained. With the help of buoys that collected information about the current waves in 2015, a few sea trials from 2015 are analysed and utilized to generate methods to acquire wave spectra for comparison with the buoys' information. Figure 6.8 shows the relative location of the ship and nearby buoys when implementing the experiments at Cape town in 2015. The experiment site was approximately five miles southwest of the harbour. When conducting experiments, the ship was continually driven for one or two miles for each trial in different directions. The buoy was positioned further to the south as marked in the figure.

Figure 6.8 Sea map at Cape Town

(Diagram from [89] legend by the author)

6.2.1 Analyses of the 2014 Results

Figure 6.9 shows the relationship between the encountered wave and ship's heading angle in sea trial four, and the encountered wave came from the beam portside. Figure 6.10 shows the results of the estimated offset values. The results show an initial period of adjustment, followed by relatively stable ranges in x- and z-direction, where the results can be determined. However, before entering the stable phase, there is a sharp decline in the y-direction, which may be caused by abnormal recorded data from the sensor itself. Finally, the offset values for the y-axis are acquired as well.

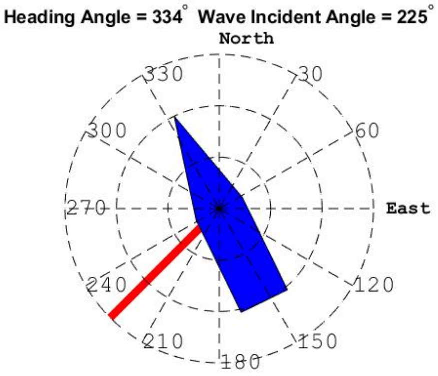

Figure 6.9 Relative sea state of trial four

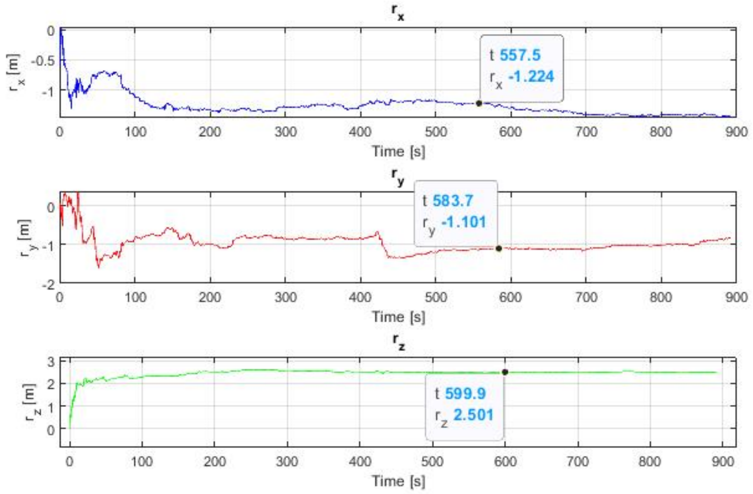

Figure 6.10 Estimated offsets of trial four

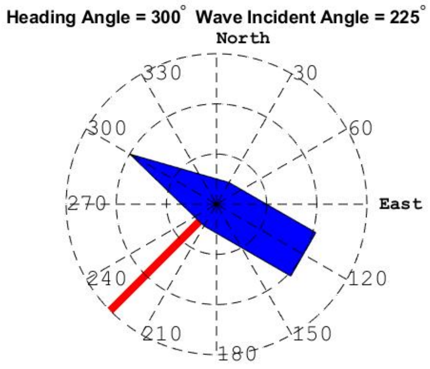

Figure 6.11 Relative sea state of trial six

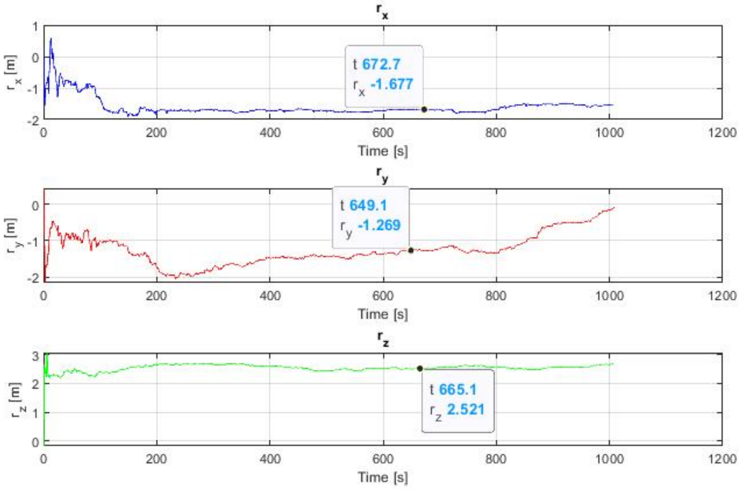

Figure 6.12 Estimated offsets of trial six

Figure 6.11 is the schematic diagram of the relationship between the encountered wave and the ship's heading in trial six. The apparent wave came as the beam sea from the portside, which is similar to the condition shown in Figure 6.9 for trial four. The estimated offsets in Figure 6.12 reached a stable value after a period of adjustment, which was quite short for the z-direction. The offset estimating curves are not stable in the y-direction either. It seems that the values begin to enter another range and then adjust again. Thus, the processing time appears to be insufficient for this trial. The selected points marked in Figures 6.10 and 6.12 demonstrate that the estimated offset values are relatively similar under analogous wave conditions.

$$P\,4 = 10^{-4} * \begin{bmatrix} 1 & 0 & 0 & \vdots & 0 & 0 & 1 \\ 0 & 1 & 0 & \vdots & 0 & 0 & 0 \\ 0 & 0 & 1 & \vdots & -1 & 0 & 0 \\ \cdots & \cdots & \cdots & \vdots & \cdots & \cdots & \cdots \\ 0 & 0 & -1 & \vdots & 42 & 2 & 0 \\ 0 & 0 & 0 & \vdots & 2 & 52 & 0 \\ 1 & 0 & 0 & \vdots & 0 & 0 & 32 \end{bmatrix} \begin{bmatrix} [(m/s^2)^2] & [m^2/s^2] \\ [m^2/s^2] & [m^2] \end{bmatrix}$$

$$CC\,4 = \begin{bmatrix} 1.0000 & -0.2843 & 0.0002 & -0.3128 & -0.3195 & 0.4634 \\ -0.2843 & 1.0000 & 0.0084 & -0.2252 & -0.2182 & -0.1535 \\ 0.0002 & 0.0084 & 1.0000 & -0.7491 & -0.1138 & 0.0003 \\ -0.3128 & -0.2252 & -0.7491 & 1.0000 & -0.1294 & -0.2074 \\ -0.3195 & -0.2182 & -0.1138 & -0.1294 & 1.0000 & -0.2122 \\ 0.4634 & -0.1535 & 0.0003 & -0.2074 & -0.2122 & 1.0000 \end{bmatrix}$$

According to the values in the *P* matrices, there are several pairs of correlations among variables for trial four. For example, the linear acceleration in the x-axis and offset in the z-axis, the linear acceleration in the z-axis and the offset in the x- and y-axis, and the offset in the x- and y-direction. Based on the mathematical model, those correlations are possible. The errors of the offset shown in the matrix would be 0.065, 0.072, and 0.057 m for the three dimensions. According to the correlation coefficient matrix *CC4*, the linear acceleration in the z-direction has a relatively strong correlation with the offset in the x-direction. However, there are still some correlations among other linear accelerations and offsets, such as the linear acceleration in the x-direction and the offset in the z-axis, as illustrated in the *P* matrix. These slight but similar correlations would affect the final estimated offset values under certain limitations.

$$P\,6 = 10^{-4} * \begin{bmatrix} 1 & 0 & 0 & \vdots & 0 & 0 & 0 \\ 0 & 1 & 0 & \vdots & 0 & 0 & 1 \\ 0 & 0 & 1 & \vdots & 0 & -1 & 0 \\ \cdots & \cdots & \cdots & \vdots & \cdots & \cdots & \cdots \\ 0 & 0 & 0 & \vdots & 29 & -1 & 0 \\ 0 & 0 & -1 & \vdots & -1 & 33 & 0 \\ 0 & 1 & 0 & \vdots & 0 & 0 & 22 \end{bmatrix} \begin{bmatrix} [(m/s^2)^2] & [m^2/s^2] \\ [m^2/s^2] & [m^2] \end{bmatrix}$$

$$CC\,6 = \begin{bmatrix} 1.0000 & -0.2052 & 0.0189 & -0.2336 & -0.2355 & 0.0267 \\ -0.2052 & 1.0000 & 0.0298 & -0.2794 & -0.2957 & 0.3832 \\ 0.0189 & 0.0298 & 1.0000 & -0.1657 & -0.6786 & 0.0014 \\ -0.2336 & -0.2794 & -0.1657 & 1.0000 & -0.2775 & -0.1906 \\ -0.2355 & -0.2957 & -0.6786 & -0.2775 & 1.0000 & -0.1924 \\ 0.0267 & 0.3832 & 0.0014 & -0.1906 & -0.1924 & 1.0000 \end{bmatrix}$$

For trial six, the correlations appear differently in the linear acceleration for the y-direction and offset in the z-direction from trial four. As shown in *CC6*, the linear acceleration in the z-direction has an obvious correlation with the offset in the y-axis, rather than the x-axis as in trial four. The remaining weak correlations are similar but slightly smaller than those of trial four. The errors of the offset are smaller than those of trial four.

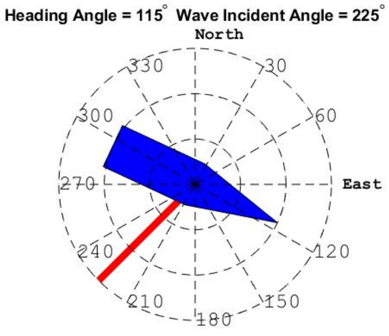

Figure 6.13 Relative sea state of trial seven

As shown in Figures 6.13 and 6.15, the relative directions between encountered waves and ship heading angles in two different sea trials are expressed. According to the figures, the ship encountered beam seas from the starboard side in both trials. Figures 6.14 and 6.16 give the estimated results of the offsets in both sea trials. A shorter time is needed when adjusting the values in the z-direction than in the x-direction, and they eventually reach steady states. After comparing the estimated values, the estimated offsets in the x- and z-direction are close to each other. However, there is a big difference in the y-direction, from 1.7 to 0.3 m. This situation is quite unusual under similar experimental conditions, and it cannot be clearly explained yet with known related coefficients.

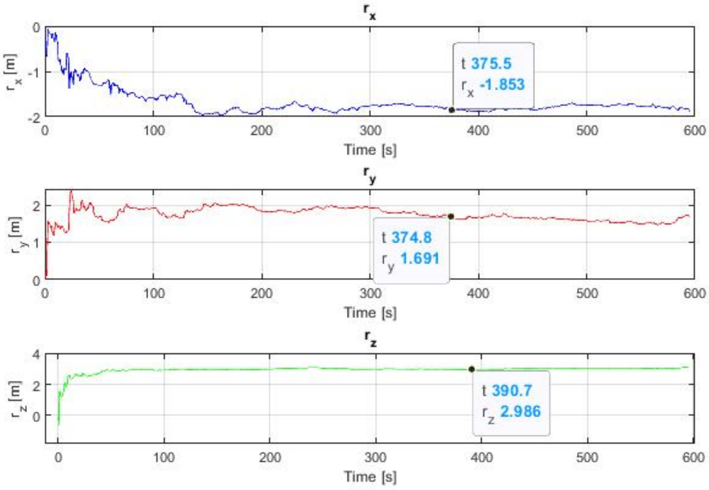

Figure 6.14 Estimated offsets of trial seven

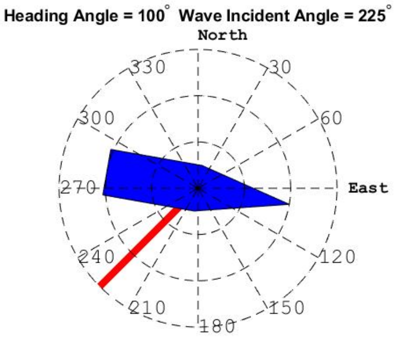

Figure 6.15 Relative sea state of trial nine

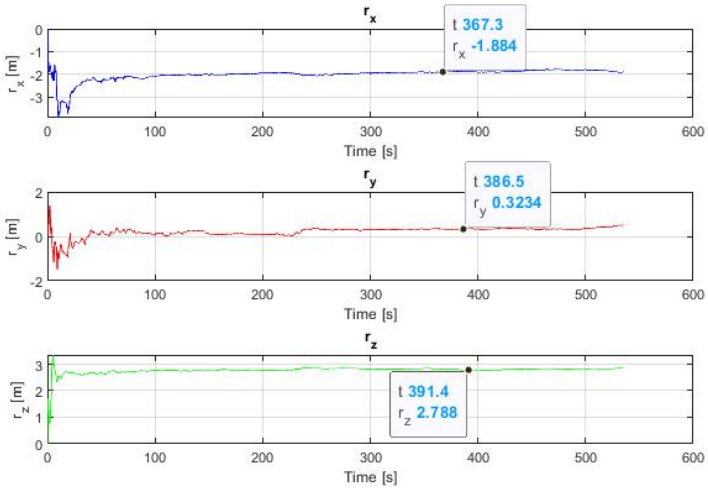

Figure 6.16 Estimated offsets of trial nine

$$P\,7 = 10^{-4} * \begin{bmatrix} 1 & 0 & 0 & \vdots & 0 & 0 & 1 \\ 0 & 1 & 0 & \vdots & 0 & 0 & 0 \\ 0 & 0 & 1 & \vdots & -1 & 0 & 0 \\ \cdots & \cdots & \cdots & \vdots & \cdots & \cdots & \cdots \\ 0 & 0 & -1 & \vdots & 39 & 0 & 0 \\ 0 & 0 & 0 & \vdots & 0 & 30 & 0 \\ 1 & 0 & 0 & \vdots & 0 & 0 & 22 \end{bmatrix} \begin{bmatrix} [(m/s^2)^2] & [m^2/s^2] \\ [m^2/s^2] & [m^2] \end{bmatrix}$$

$$CC\,7 = \begin{bmatrix} 1.0000 & -0.3850 & 0.0472 & -0.3022 & -0.3071 & 0.6082 \\ -0.3850 & 1.0000 & 0.0989 & -0.2304 & -0.1143 & -0.3692 \\ 0.0472 & 0.0989 & 1.0000 & -0.8980 & 0.2034 & 0.0245 \\ -0.3022 & -0.2304 & -0.8980 & 1.0000 & -0.2195 & -0.1913 \\ -0.3071 & -0.1143 & 0.2034 & -0.2195 & 1.0000 & -0.2065 \\ 0.6082 & -0.3692 & 0.0245 & -0.1913 & -0.2065 & 1.0000 \end{bmatrix}$$

$$P\,9 = 10^{-4} * \begin{bmatrix} 1 & 0 & 0 & \vdots & 0 & 0 & 0 \\ 0 & 1 & 0 & \vdots & 0 & 0 & 0 \\ 0 & 0 & 1 & \vdots & 1 & 0 & 0 \\ \cdots & \cdots & \cdots & \vdots & \cdots & \cdots & \cdots \\ 0 & 0 & 1 & \vdots & 34 & 1 & 0 \\ 0 & 0 & 0 & \vdots & 1 & 35 & 0 \\ 0 & 0 & 0 & \vdots & 0 & 0 & 25 \end{bmatrix} \begin{bmatrix} [(m/s^2)^2] & [m^2/s^2] \\ [m^2/s^2] & [m^2] \end{bmatrix}$$

$$CC\,9 = \begin{bmatrix} 1.0000 & -0.0402 & -0.1649 & -0.1066 & -0.1016 & -0.5552 \\ -0.0402 & 1.0000 & -0.3056 & -0.1994 & -0.1861 & -0.2831 \\ -0.1649 & -0.3056 & 1.0000 & 0.3683 & -0.1472 & -0.3379 \\ -0.1066 & -0.1994 & 0.3683 & 1.0000 & -0.1376 & -0.2063 \\ -0.1016 & -0.1861 & -0.1472 & -0.1376 & 1.0000 & -0.2047 \\ -0.5552 & -0.2831 & -0.3379 & -0.2063 & -0.2047 & 1.0000 \end{bmatrix}$$

In trial seven, again, the correlation between the linear acceleration in the x-direction and the offset in the z-direction occurs, except for common correlations. However, in trial nine, these additional correlations disappear. Such tendencies are also consistent in the correlation coefficients matrices. In *CC7*, a strong correlation appears between the linear acceleration in the z-direction and the offset in the x-axis, whereas in *CC9*, no apparent correlation occurs among those variables.

In Table 6.2, the results from all sea trials implemented on Fathom 10 in 2014 are shown. The first column headed ‘No.’ shows the sequence name of every sea trial. It starts from two because trial one was performed when the ship was coming out from the dock into the sea. Owing to many uncertainties, such as heading angles and ship velocities, accompanied by complex external forces, this trial is not suitable to estimate the location of the CR. The second column shows the heading angles. The third column shows the relative direction between the encountered wave at an angle of 225° and the ship. Using known CG as the origin of a reference coordinate system, the position of the sensor box in this coordinate system should be (0.5, 0, 1.9) m in bow, portside, and upward direction. The fourth to the seventh columns present the averaged estimated offsets values after settling in three dimensions, and the eighth to the last columns show the distance between the CR and CG in three dimensions, which are calculated by subtracting the estimated offsets values from the sensor position to give a position with respect to the known position of the CG.

For all the sea trials in 2014, either portside or starboard side, the offset values in the z-direction vary in a small range. The largest difference among them is almost 1 m in the z-direction, but the smallest difference is only 3 cm. The values changed slightly more in the x-direction than those in the z-direction but still within an acceptable range compared to the ship's length. However, according to the *P* matrix, the errors generated from the estimation process should be within at most around 0.1 m. As shown in the figures, most of the calculation process is relatively stable, and the values are steady, but much more significant differences are expressed in the table. The initial measured data would cause these differences. Because the values are not precisely at certain specific points, we could only conclude that the location of CR is in that region with differences in the x- and z-direction due to different effects of wave conditions, ship behaviour, and measurement errors. When waves affect the portside, the location of the CR in the y-direction shifts slightly to the starboard side and vice versa, which is plausible. However, the differences between these two sides in the y-direction vary quite significantly. The most probable reason is that the beam sea was dominant during that period. Moreover, the wavelength was rather long, approximately 150 m, compared with the length of the ship; this massive difference would cause unsteady ship behaviours, and therefore the estimated values cannot remain stable according to this strong and direct influence from the waves.

No.	**Heading Angle [°]**	**Wave and Ship Relative Direction**	**Offset Value [m]**			**Distance between CR and CG [m]**		
			r_x	**r_y**	**r_z**	**x**	**y**	**z**
2	40	Port	-1.45	0.14	2.64	1.95	-0.14	-0.74
3	180	Stb	-1.52	2.17	2.16	2.02	-2.17	-0.26
4	334	Port	-1.33	-1.09	2.50	1.83	1.09	-0.60
5	140	Stb	-1.88	2.65	2.69	2.38	-2.65	-0.79
6	300	Port	-1.70	-1.37	2.55	2.20	1.37	-0.65
7	115	Stb	-1.80	1.74	3.01	2.30	-1.74	-1.11
8	278	Port	-2.05	-2.60	2.85	2.55	2.60	-0.95
9	100	Stb	-1.88	0.33	2.82	2.38	-0.33	-0.92
10	249	Port	-1.98	-3.04	2.42	2.48	3.04	-0.58
11	111	Stb	-1.63	-0.12	2.70	2.13	0.12	-0.80
12	220	Stb	-1.49	-2.00	2.09	1.99	2.00	-0.19
13	39	Port	-1.58	-0.26	2.74	2.08	0.26	-0.84

Table 6.2 CR results of Fathom 10 in 2014

Considering the results in the table, each sea trial has a set of unique, certain values of the estimated averaged offsets and shows that the location of CR in the x- and z-direction moving within a small range in the ship. As described in Figure 6.17, the x-axis represents the trial number and the y-axis represents the normalized offset values for all three dimensions. The normalization method applied here uses the actual values to divide the absolute maximum value among all values. This method is quite clear to obtain the relative information of all the offset values. The positive and negative directions are consistent with the directions describing the defined ship body-fixed frame in this work. As shown in the table and illustrated in the figure, the offset in the x- and z-direction is relatively stable, whereas in the y-direction, the values are not stable at all and continually change their sign.

Overall, the CR's location remains ahead of the CG by approximately 2 m in the x-direction, namely close to the bow, and remains below the CG by approximately 0.9 m in the z-direction, near the keel. In the y-direction, the positive and negative values are mainly based on the direction from which the waves approach; they are systematic, but the values change unstably and irregularly, indicating that the beam sea has a significant influence on the lateral motions of the ship, and it can indeed produce much stronger effects on the ship's movement with respect to the relative length between the ship and encountered wave.

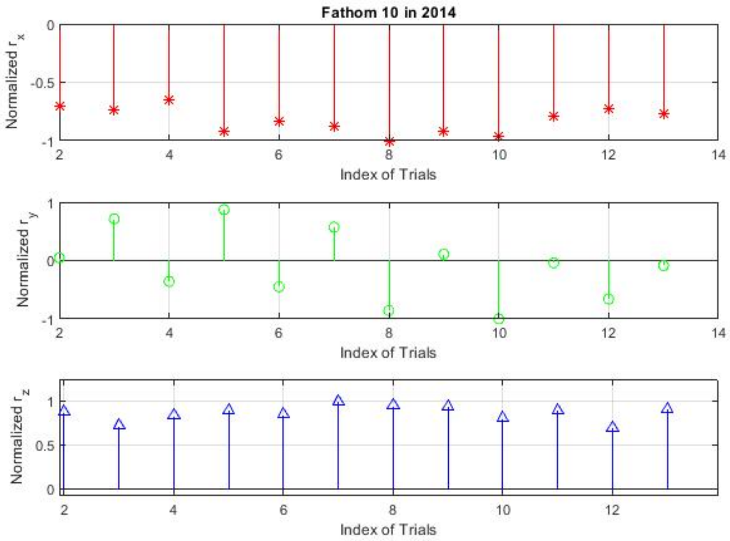

Figure 6.17 Normalization of the offset for Fathom 10

6.2.2 Analyses of the 2015 Results

The results of 2015 are presented in this section; the peak direction of the encountered wave was 210°, in contrast to 225° as in 2014. Based on the wave information provided by the buoys, the wave information generated from the estimated ship motion can be utilized to make comparisons with the buoy information, so as to test the validity of the located CR in an authentic and feasible way.

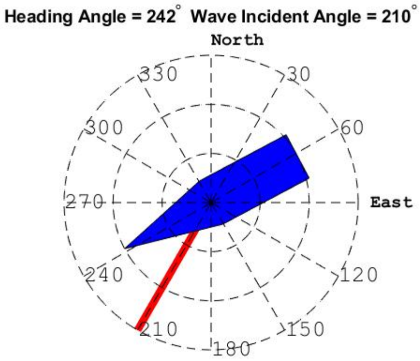

Figure 6.18 Relative sea state of trial thirty-one

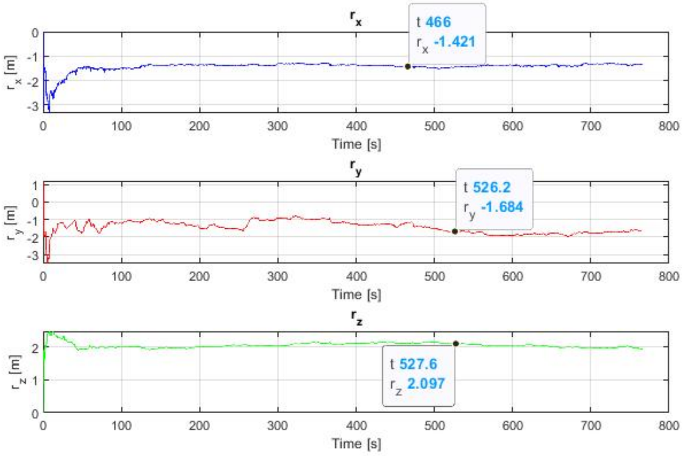

Figure 6.19 Estimated offsets of trial thirty-one

Figure 6.18 gives information about the relationship between the ship's heading angle and the encountered wave for sea trial thirty-one. According to the figure, the ship was under a bow sea from the portside. Figure 6.19 shows the results of the estimated offsets from that trial in three dimensions. Judging from the curves, the offsets reached a steady value after a quick regulation in the x- and z-direction. For the y-direction, the same problem appears as from the data in 2014; the curve illustrates that the steady value is not fixed and it moves to another point as time passes.

Figures 6.20 and 6.21 show power spectrum distribution (PSD) results for the surge and heave motions, respectively. There are two curves in each figure. The solid lines indicate the results of the estimated corresponding motions at the CR by using the Kalman filter, and the lines with crosses represent the results calculated from the nearby buoys. The PSD results from the buoys are calculated by a method described in Appendix A. Comparing the spectral magnitudes, the wave buoy's frequencies are shifted to a higher encounter frequency, but the peak frequencies of the KF results are still quite close to the observed frequencies. A good fit is observed for the surge motion, although there is a significant difference in the heave motion. The shapes of both curves for the heave motion are similar, but the power values remain dissimilar. As the buoy's data could not be exactly accurate and reliable, this discrepancy is unsurprising.

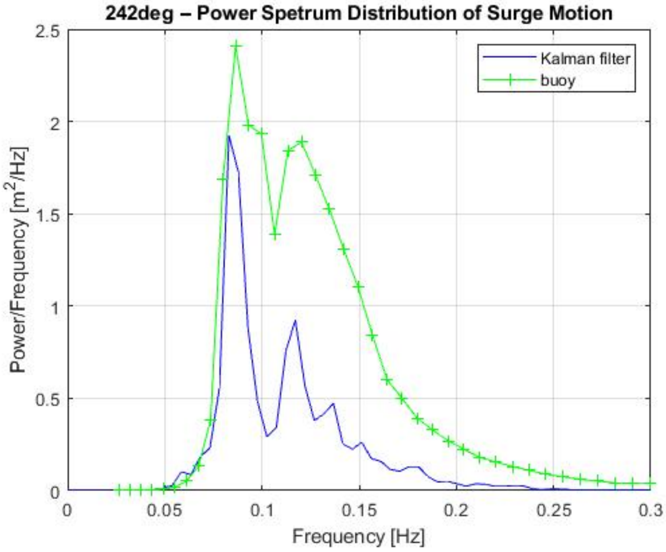

Figure 6.20 Comparison of surge PSD of trial thirty-one

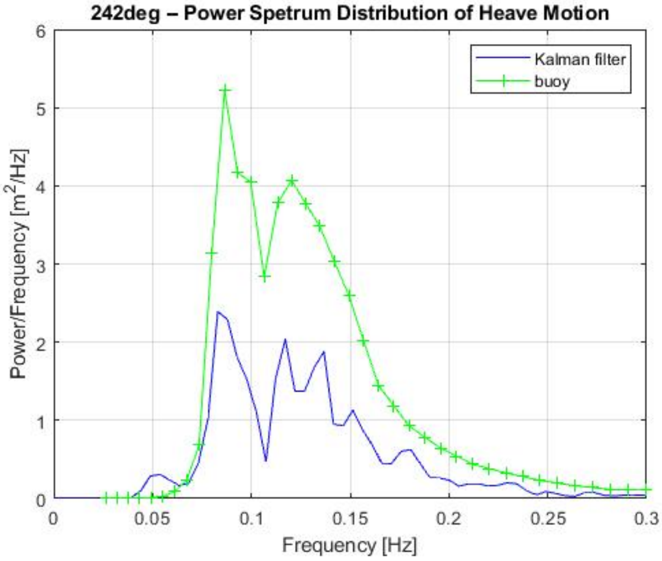

Figure 6.21 Comparison of heave PSD of trial thirty-one

Figure 6.22 shows another heading angle of the sea trials, with a following sea from the starboard side. The estimated offset values are plotted in Figure 6.23. The offsets in the x- and z-direction reach stable values after some oscillations in the first phase, as in trial thirty-one. However, there are still some uncertainties in the y-direction. The tendency is not always converged or only converges in certain periods, but the whole curve is unstable and does not reach a steady state. The marked points in these two trials are similar in the x- and z-direction but have the opposite signs in the y-direction. Because the encountered waves approached from opposite sides for these two trials, the occurrence of opposite signs is plausible. Nevertheless, the values vary in a large range, which could be due to the strong effects of the wave. This problem should be explained and tested by more cases under analogous circumstances.

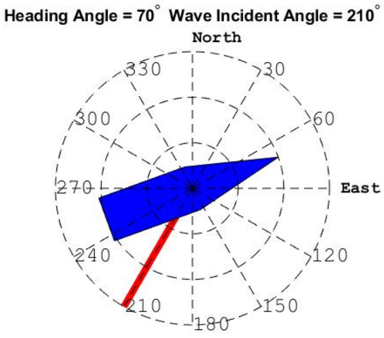

Figure 6.22 Relative sea state of trial thirty-two

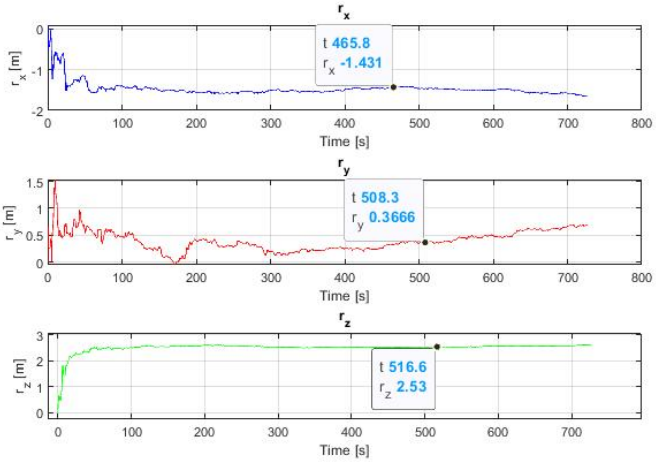

Figure 6.23 Estimated offsets of trial thirty-two

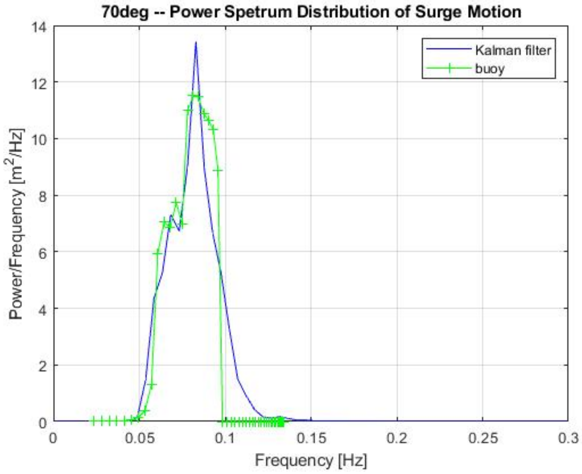

Figure 6.24 Comparison of surge PSD of trial thirty-two

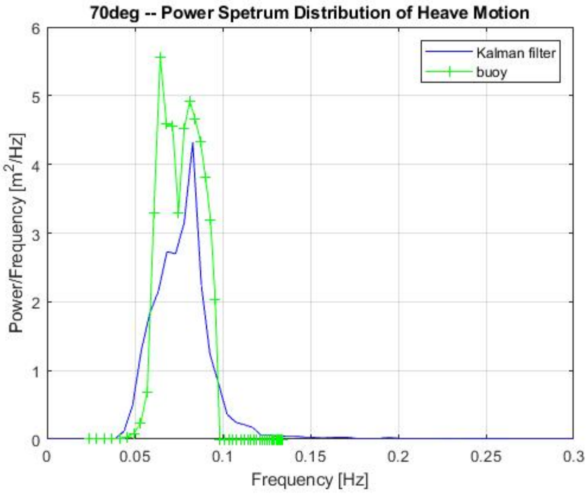

Figure 6.25 Comparison of heave PSD of trial thirty-two

The PSD results of surge and heave motions are illustrated for this sea trial in Figures 6.24 and 6.25, respectively. The wave buoy's frequencies are shifted to the lower encountered frequencies, but the peak frequencies of both methods are almost identical to each other. A good fit has been obtained in the surge motion with similar shapes and total areas of the PSD. In the heave motion, apart from the peak in the left zone at approximately 0.06 Hz, the remainder of the distribution shows a rather good fit as expected. In this case, the results have entered a region of ambiguous encountered frequencies, as illustrated in Appendix A. This ambiguity is difficult to resolve, and this region must be excluded from the RAOs. Therefore, the spectrum in these figures declines quickly and sharply when the frequency exceeds 0.1 Hz.

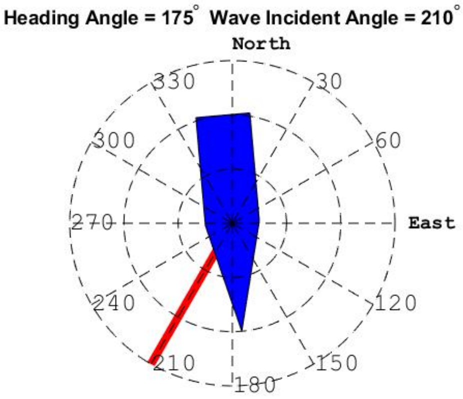

Figure 6.26 Relative sea state of trial thirty-four

Figures 6.26 to 6.29 present results of sea trial thirty-four. As described in the figure, the ship was under a bow sea from the starboard side. The estimated offsets are relatively good compared to other cases, because the offset in the y-direction seems to be relatively stable instead of oscillating. However, the values calculated from the y-direction are significantly different from the other cases, at approximately 1.95 m. The estimated values of the x- and z-direction are in steady states as in other cases, and a rather short adjustment time is needed to reach their final phases.

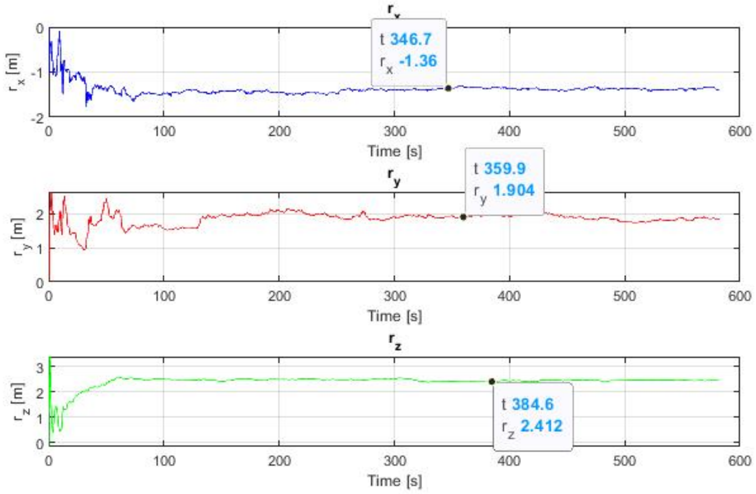

Figure 6.27 Estimated offsets of trial thirty-four

To describe the results of the PSD, first, we note that the curve shapes in the surge and heave motion match rather well, with almost identical peak frequencies. Second, they all have differences in the power magnitudes, such that the power calculated based on the buoy's data is stronger than that estimated from the KF.

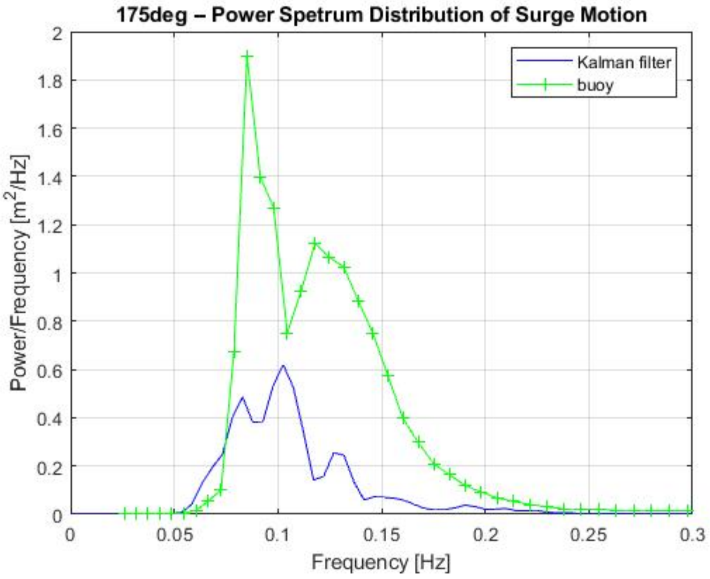

Figure 6.28 Comparison of surge PSD of trial thirty-four

Among all the spectral results describing the ship motions, the calculated peak frequencies are similar from the Kalman filter and the corresponding buoy's data. Furthermore, the shapes of spectra are similar as well. It is clearly indicated that the sets of wave information generated from these two different methods are almost identical, which demonstrates that the motion at the CR is the actual ship motion regardless of any influences either by the measurement units or external effects. There are reasonable fits in the surge motion for sea trials thirty-one and thirty-two, and the spectra fit better in sea trial thirty-one than in trial thirty-two. Neither motion fits very well in sea trial thirty-four. First, the buoy was not precisely located at the experimental site, as shown in Figure 6.8. Thus, the recorded wave information might be different from that at the experimental site with respect to the propagation and water depth. Furthermore, the precision of the recorded buoy data could affect the magnitudes of each spectrum. Second, the calculation of RAOs presented certain doubts with respect to spectral acquisition. Finally, in the higher frequencies, such as up to 0.2 Hz, the offset vector has minor effects on the spectrum when the heave and surge RAOs are close to unity.

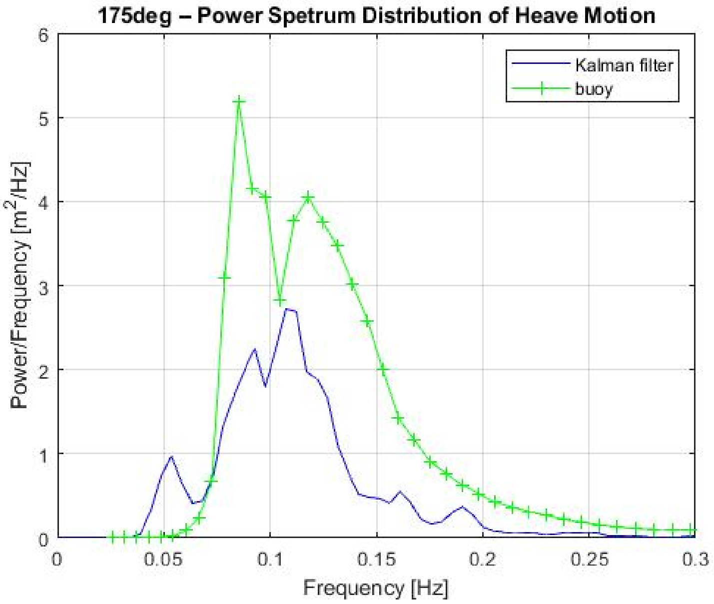

Figure 6.29 Comparison of heave PSD of trial thirty-four

$$P\;31 = 10^{-4} * \begin{bmatrix} 1 & 0 & 0 & \vdots & 0 & 0 & 1 \\ 0 & 1 & 0 & \vdots & 0 & 0 & 0 \\ 0 & 0 & 1 & \vdots & -1 & 0 & 0 \\ \cdots & \cdots & \cdots & \vdots & \cdots & \cdots & \cdots \\ 0 & 0 & -1 & \vdots & 21 & 5 & 0 \\ 0 & 0 & 0 & \vdots & 5 & 51 & 0 \\ 1 & 0 & 0 & \vdots & 0 & 0 & 18 \end{bmatrix} \begin{bmatrix} [(m/s^2)^2] & [m^2/s^2] \\ [m^2/s^2] & [m^2] \end{bmatrix}$$

$$CC\;31 = \begin{bmatrix} 1.0000 & -0.4433 & -0.0742 & -0.3621 & -0.3580 & 0.6619 \\ -0.4433 & 1.0000 & 0.0119 & -0.2126 & -0.1245 & -0.4292 \\ -0.0742 & 0.0119 & 1.0000 & -0.7903 & 0.1868 & -0.0340 \\ -0.3621 & -0.2126 & -0.7903 & 1.0000 & 0.1254 & -0.2491 \\ -0.3580 & -0.1245 & 0.1868 & 0.1254 & 1.0000 & -0.2367 \\ 0.6619 & -0.4292 & -0.0340 & -0.2491 & -0.2367 & 1.0000 \end{bmatrix}$$

$$P\,32 = 10^{-4} * \begin{bmatrix} 1 & 0 & 0 & \vdots & 0 & 0 & -1 \\ 0 & 1 & 0 & \vdots & 0 & 0 & -1 \\ 0 & 0 & 1 & \vdots & 1 & 3 & 0 \\ \cdots & \cdots & \cdots & \vdots & \cdots & \cdots & \cdots \\ 0 & 0 & 1 & \vdots & 52 & -1 & 0 \\ 0 & 0 & 3 & \vdots & -1 & 82 & 0 \\ -1 & -1 & 0 & \vdots & 0 & 0 & 40 \end{bmatrix} \begin{bmatrix} [(m/s^2)^2] & [m^2/s^2] \\ [m^2/s^2] & [m^2] \end{bmatrix}$$

$$CC\,32 = \begin{bmatrix} 1.0000 & 0.6339 & -0.0326 & -0.0078 & -0.0398 & -0.7856 \\ 0.6339 & 1.0000 & 0.0906 & 0.0475 & 0.0412 & -0.8860 \\ -0.0326 & 0.0906 & 1.0000 & 0.1165 & 0.8834 & -0.3474 \\ -0.0078 & 0.0475 & 0.1165 & 1.0000 & -0.2556 & -0.1834 \\ -0.0398 & 0.0412 & 0.8834 & -0.2556 & 1.0000 & -0.1895 \\ -0.7856 & -0.8860 & -0.3474 & -0.1834 & -0.1895 & 1.0000 \end{bmatrix}$$

$$P\,34 = 10^{-4} * \begin{bmatrix} 1 & 0 & 0 & \vdots & 0 & 0 & 1 \\ 0 & 1 & 0 & \vdots & 0 & 0 & 0 \\ 0 & 0 & 1 & \vdots & -2 & 1 & 0 \\ \cdots & \cdots & \cdots & \vdots & \cdots & \cdots & \cdots \\ 0 & 0 & -2 & \vdots & 26 & -2 & 0 \\ 0 & 0 & 1 & \vdots & -2 & 31 & 0 \\ 1 & 0 & 0 & \vdots & 0 & 0 & 19 \end{bmatrix} \begin{bmatrix} [(m/s^2)^2] & [m^2/s^2] \\ [m^2/s^2] & [m^2] \end{bmatrix}$$

$$CC\,34 = \begin{bmatrix} 1.0000 & -0.6047 & -0.0232 & -0.2676 & -0.2830 & 0.7768 \\ -0.6047 & 1.0000 & 0.0206 & -0.0834 & -0.0456 & -0.6312 \\ -0.0232 & 0.0206 & 1.0000 & -0.9068 & 0.5089 & -0.0256 \\ -0.2676 & -0.0834 & -0.9068 & 1.0000 & -0.3228 & -0.1733 \\ -0.2830 & -0.0456 & 0.5089 & -0.3228 & 1.0000 & -0.1988 \\ 0.7768 & -0.6312 & -0.0256 & -0.1733 & -0.1988 & 1.0000 \end{bmatrix}$$

The correlations of trials thirty-one, thirty-two, and thirty-four are similar to those of trials performed in 2014, and they include more correlations than the Marvin in the linear accelerations. As shown in matrices *CC31*, *CC32*, and *CC34*, strong correlations appear between linear acceleration in the z-direction and the offset in the x-axis or y-axis. Relatively weak correlations appear between the linear accelerations in the other two directions and the offset in the z-axis. The offset of the trial thirty-one error vector is (0.051, 0.056, 0.044) m. In trial thirty-four, the ship encountered a bow sea as well. Therefore, the values of the errors are close to those of trial thirty-one. More significant errors appear in trial thirty-two, as the ship encountered a following sea.

Comparing all the values in Table 6.3, apart from trial thirty-six, the offsets in the x-axis seem stable, although the differences can reach up to 0.2 m. The offsets in the z-direction are stable as well, but considering the measurement errors and the size of the ship, these differences are tolerable. A displacement bias of only 0.2 m would not matter in a ship with a length of 20 m. However, this is a not suitable compromise for the offset in the y-direction. With such significant differences, the influences made by the calculated errors or even the measurement errors are no longer predominant.

No.	Heading Angle [°]	Wave and Ship Relative Direction	Offset Value [m]			Distance between CR and CG [m]		
			r_x	r_y	r_z	x	y	z
31	242	Port	-1.37	-1.48	2.06	1.87	1.48	-0.06
32	70	Stb	-1.51	0.37	2.54	2.01	-0.37	-0.64
33	335	Port	-1.60	-1.67	2.64	2.10	1.67	-0.74
34	175	Stb	-1.40	1.93	2.46	1.9	-1.93	-0.56
35	40	Stb	-1.32	0.51	3.03	1.82	-0.51	-1.13
36	226	Port	-1.96	3.96	1.96	2.46	-3.96	-0.06

Table 6.3 CR results of Fathom 10 in 2015

Judging from Table 6.3, just as in 2014, each sea trial has a set of unique values of the estimated averaged offsets. However, with fewer sea trials, the values in Table 6.3 are more varied than those from 2014. In conclusion, the CR's location remains mainly ahead of the CG by approximately 2 m and it is close to the bow. Moreover, it remains below the CG, near the keel. In the y-direction, the values are diverse and disordered, but in most cases, the signs of the values are determined by the side from which encountered waves approach.

The extreme exception for all cases of 2014 and 2015 is sea trial thirty-six, which has the most significant offset in the x-direction, a minor offset in the z-direction, and an undesired starboard-side offset in the y-direction. This case is entirely contrary to our expectations and unique because the ship velocity was as high as 13 kn. With such a high velocity compared to the ship’s size, the impacts that occurred against encountered waves could be quite different from those at lower speeds, leading to a totally abnormal value of the location of the CR compared with other trials. When riding on this encountered wave from the bow, a strong influence would appear in the vertical direction, generating a tiny offset in the z-direction. As the uncertainties always existed in the y-direction, for this trial with a much higher velocity, this value could not be completely trusted.

Apart from this higher-speed sea trial, the other trials were all conducted at a velocity at 7.5 kn. Analysing all the sea trials of both years, the estimated offsets and the relative positions between CR and CG are systematic in most of the trials. When the encountered waves came from the portside, the CR would be at the starboard side of the CG, and vice versa. The CR would be at the portside of the CG when the ship encountered starboard waves. The CR's location contains three dimensions. In the x-direction, the values stay mostly at 2 m positive, representing that the CR is ahead of the CG. In the z-direction, most values remain at 0.7 m negative, indicating that the CR is below the CG. Judging from these values, the location of CR stays relatively stable in a specific range with a short adjustment time for each trial. However, in the y-direction, there are too many indeterminacies. Therefore, the relative position in this direction cannot be determined for now. The most probable reason for this situation is the large difference between the size of the ship and the length of encountered waves. According to the RAOs of the pitch motion of this ship at a speed of 7.5 kn, the ship is affected mainly by the encountered waves between 0.2 and 0.3 Hz, which is the ship's sensitivity range, whereas the actual encountered wave frequency is only 0.09 Hz. When a ship such as Fathom 10, with a length of 20 m, encounters these longer periods and waves of length 100 m, the ship only moves up and down rather slowly with no prominent roll and pitch motions. Hence, the roll and pitch motions would be relatively small, and they are possibly caused not by the dominant encountered waves, but rather by other shorter waves. Thus, they may not be precise enough to be utilized in the following calculations when applying the algorithm.

6.3 Result of Simon Stevin

A few examples of sea trials on the Simon Stevin are presented in this part to analyse the estimated offset values in different sea states. A few sensor boxes were installed onboard during the voyages, but in this research, only the recorded data from the sensor box placed on the bridge are available for analysis. The sensor's installation location in the ship body frame was determined to be (-1.1, 2, 6.99) m in the stern, portside, and upwards directions.

6.3.1 Analyses of Several Trials

The relationships between the ship's heading angles and incident waves are illustrated in the following figures. Figures 6.30 and 6.32 show following seas at the portside, and Figures 6.34 and 6.36 show following seas at the starboard side. Next, Figures 6.38 and 6.40 show bow seas at the portside. Finally, Figures 6.42 and 6.44 show bow seas at the starboard side. The following seas and bow seas are assumed to have fewer effects on the motions in the y-direction than the beam seas.

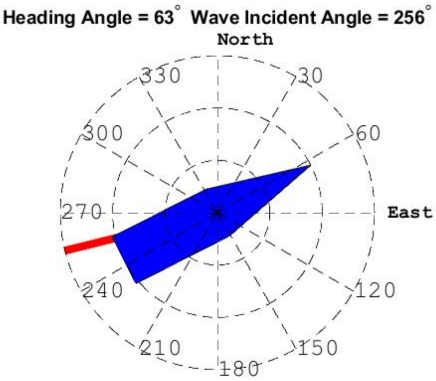

Figure 6.30 Relative sea state of trial four

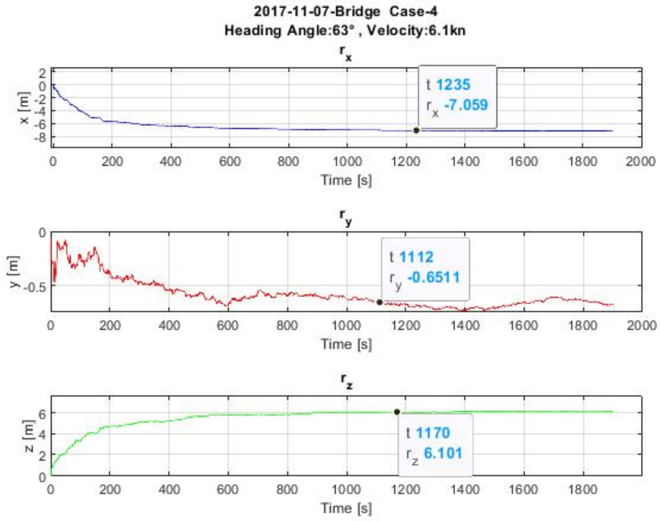

Figure 6.31 Estimated offsets of trial four

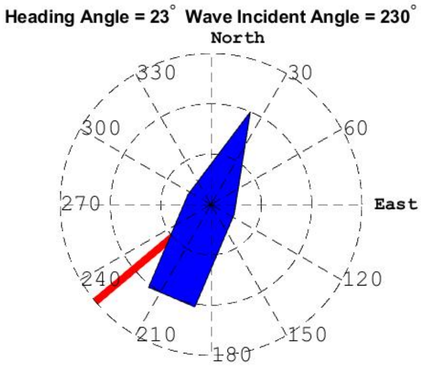

Figure 6.32 Relative sea state of trial twenty-one

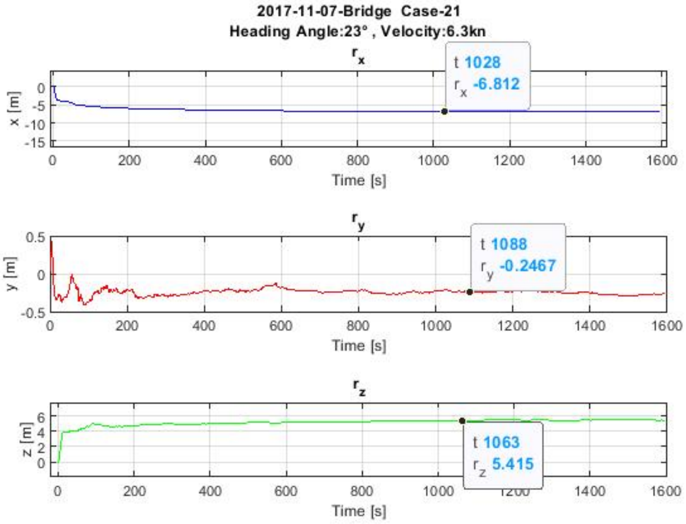

Figure 6.33 Estimated offsets of trial twenty-one

Figures 6.31 and 6.33 present the estimated offset results for two trials. Both adjust the offset values initially, and then reach a relatively stable value within a duration, especially in the x- and z-direction. Although these two trials are under somewhat similar environmental conditions, there are still differences in the values in each direction. These are approximately 0.3 m in the x-direction, 0.4 m in the y-direction, and nearly 0.6 m in the z-direction.

$$P\,4 = 10^{-4} * \begin{bmatrix} 1 & 0 & 0 & \vdots & 0 & 0 & 0 \\ 0 & 1 & 0 & \vdots & 0 & 0 & 0 \\ 0 & 0 & 1 & \vdots & 0 & 1 & 0 \\ \cdots & \cdots & \cdots & \vdots & \cdots & \cdots & \cdots \\ 0 & 0 & 0 & \vdots & 179 & -34 & 0 \\ 0 & 0 & 1 & \vdots & -34 & 517 & 0 \\ 0 & 0 & 0 & \vdots & 0 & 0 & 149 \end{bmatrix} \begin{bmatrix} [(m/s^2)^2] & [m^2/s^2] \\ [m^2/s^2] & [m^2] \end{bmatrix}$$

$$CC\,4 = \begin{bmatrix} 1.0000 & -0.0702 & -0.2804 & -0.1383 & -0.1541 & -0.2967 \\ -0.0702 & 1.0000 & -0.1968 & -0.0922 & -0.1123 & -0.4775 \\ -0.2804 & -0.1968 & 1.0000 & -0.3903 & 0.6944 & -0.3252 \\ -0.1383 & -0.0922 & -0.3903 & 1.0000 & -0.4260 & -0.1537 \\ -0.1541 & -0.1123 & 0.6944 & -0.4260 & 1.0000 & -0.1843 \\ -0.2967 & -0.4775 & -0.3252 & -0.1537 & -0.1843 & 1.0000 \end{bmatrix}$$

$$P\,21 = 10^{-4} * \begin{bmatrix} 1 & 0 & 0 & \vdots & 0 & 0 & 1 \\ 0 & 1 & 0 & \vdots & 0 & 0 & 0 \\ 0 & 0 & 1 & \vdots & -1 & 0 & 0 \\ \cdots & \cdots & \cdots & \vdots & \cdots & \cdots & \cdots \\ 0 & 0 & -1 & \vdots & 152 & -25 & 0 \\ 0 & 0 & 0 & \vdots & -25 & 357 & 0 \\ 1 & 0 & 0 & \vdots & 0 & 0 & 122 \end{bmatrix} \begin{bmatrix} [(m/s^2)^2] & [m^2/s^2] \\ [m^2/s^2] & [m^2] \end{bmatrix}$$

$$CC\,21 = \begin{bmatrix} 1.0000 & -0.3678 & 0.0010 & -0.2544 & -0.2840 & 0.7087 \\ -0.3678 & 1.0000 & -0.0045 & -0.1369 & -0.1668 & -0.2824 \\ 0.0010 & -0.0045 & 1.0000 & -0.8856 & 0.3439 & -0.0047 \\ -0.2544 & -0.1369 & -0.8856 & 1.0000 & -0.4099 & -0.1594 \\ -0.2840 & -0.1668 & 0.3439 & -0.4099 & 1.0000 & -0.1843 \\ 0.7087 & -0.2824 & -0.0047 & -0.1594 & -0.1843 & 1.0000 \end{bmatrix}$$

The P matrices for the Simon Stevin have more significant error covariances in the offset part, leading to greater variation in the estimated offset values. For instance, the errors of trial four are 0.134, 0.227, and 0.122 m in three dimensions, and a relatively strong correlation appears between the linear acceleration in the z-direction and the offset in the y-axis. Moreover, the offset in the x- and y-axis are correlated, as shown in the correlation coefficient matrix, *CC4*. Trial twenty-one has similar errors at the same level, and the corresponding correlations are stronger as well. Furthermore, as expressed in *CC21*, apart from the common correlations among linear accelerations and offsets as with other ships, certain correlations appear between the offset in the x- and y-axis. Overall, according to the matrices, the linear acceleration in the x-direction correlates with the offset in the z-direction, while the linear acceleration in the z-direction correlates with the offset both in the x- and y-axis; additionally, the offset in the x- and y-direction are correlated with each other.

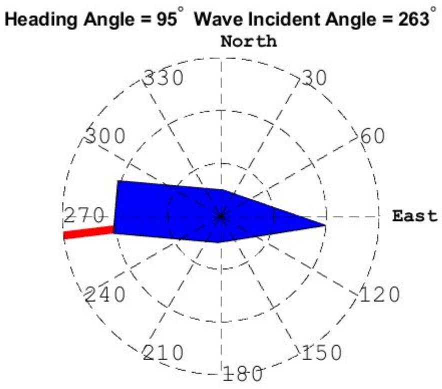

Figure 6.34 Relative sea state of trial nine

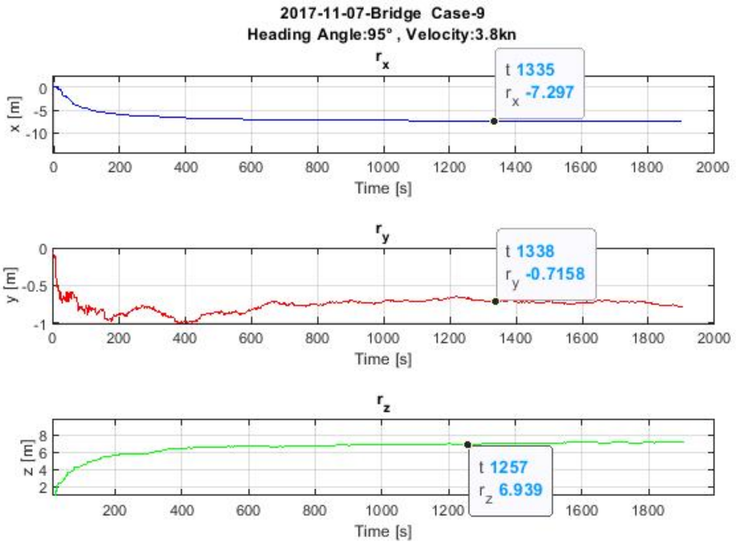

Figure 6.35 Estimated offsets of trial nine

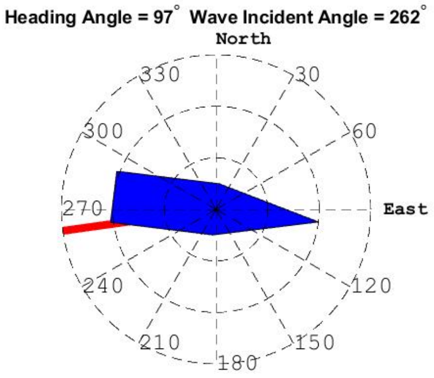

Figure 6.36 Relative sea state of trial eighteen

Figures 6.35 and 6.37 show the results of sea trials nine and eighteen, which encountered following seas but at the opposite side comparing with the previous two trials; that is, the encountered waves approached from the starboard side. As with the portside results, after quick settlements, the curves remain stable with small vibrations in all three directions. The difference in the estimated offsets values between these two trials is (0.3, 0.4, 0.2) m in three dimensions.

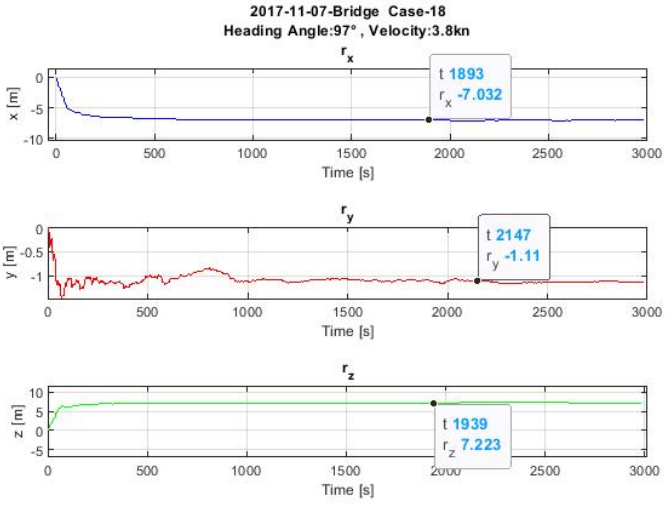

Figure 6.37 Estimated offsets of trial eighteen

$$P\,9 = 10^{-4} * \begin{bmatrix} 1 & 0 & 0 & \vdots & 0 & 0 & 0 \\ 0 & 1 & 0 & \vdots & 0 & 0 & 0 \\ 0 & 0 & 1 & \vdots & -1 & 1 & 0 \\ \cdots & \cdots & \cdots & \vdots & \cdots & \cdots & \cdots \\ 0 & 0 & -1 & \vdots & 191 & -101 & 0 \\ 0 & 0 & 1 & \vdots & -101 & 478 & 0 \\ 0 & 0 & 0 & \vdots & 0 & 0 & 137 \end{bmatrix} \begin{bmatrix} [(m/s^2)^2] & [m^2/s^2] \\ [m^2/s^2] & [m^2] \end{bmatrix}$$

$$CC\,9 = \begin{bmatrix} 1.0000 & -0.2852 & -0.2308 & -0.1032 & -0.2023 & 0.1508 \\ -0.2852 & 1.0000 & -0.1310 & -0.0570 & -0.1152 & -0.3724 \\ -0.2308 & -0.1310 & 1.0000 & -0.7784 & 0.6510 & -0.1696 \\ -0.1032 & -0.0570 & -0.7784 & 1.0000 & -0.7431 & -0.0766 \\ -0.2023 & -0.1152 & 0.6510 & -0.7431 & 1.0000 & -0.1483 \\ 0.1508 & -0.3724 & -0.1696 & -0.0766 & -0.1483 & 1.0000 \end{bmatrix}$$

In trial nine, the largest value of the error covariance appears in the offset for the y-direction, and a strong correlation also appears between the linear acceleration in the z-direction and the offset in the y-axis. Therefore, the offset in the y-axis would show more oscillation with the change in the linear acceleration in the z-axis. The values for offset errors are 0.138, 0.219, and 0.117 m in three dimensions. With such magnitudes of the errors, it is plausible that the estimated offset values would be rather different from the other cases, even those with similar experimental conditions.

Among the cases of following seas, when comparing the marked values and the mean values of the estimated offsets, a relatively stable value can indeed be reached. Furthermore, similar but unique value sets of each sea trial can be acquired under similar sea environments and environmental conditions. Even when the encountered waves have changed their directions, the

CR can still remain in the same range without resulting in significant variations in the other directions.

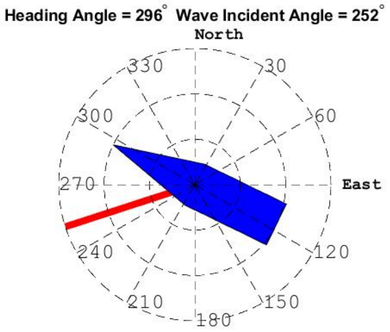

Figure 6.38 Relative sea state of trial three

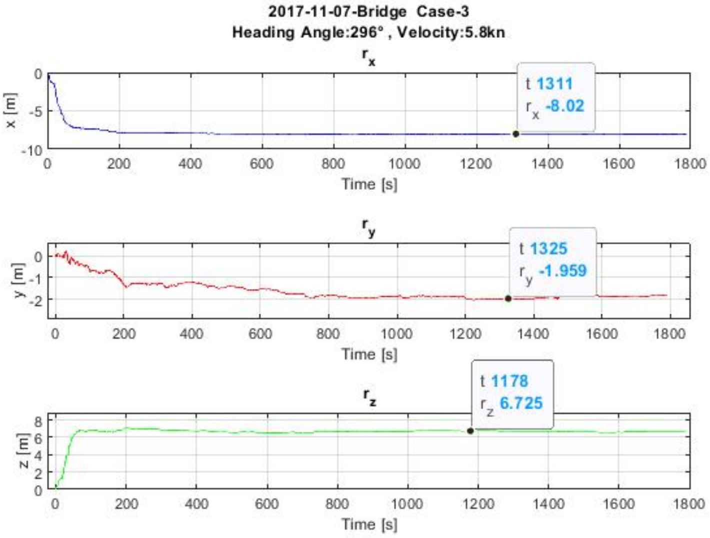

Figure 6.39 Estimated offsets of trial three

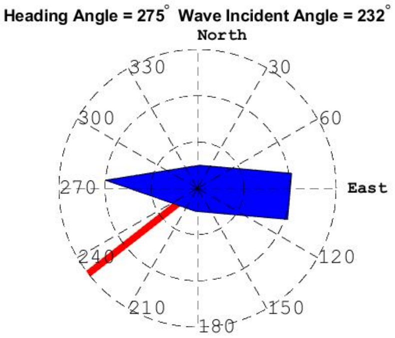

Figure 6.40 Relative sea state of trial seventeen

Bow seas always involve a rather complex sea environment and additional external forces on the ship. Judging from Figures 6.39 and 6.41, when waves came from the portside, the CR's location remains within a particular range. However, these two trials were implemented with different ship velocities, which may be the reason for the more significant differences between them. In Figures 6.43 and 6.45, when encountering waves from the starboard side, the estimated offsets are stable after settlements, and the results are similar. The only change that happens to the sign in the y-axis, which represents the CR's location on the y-axis, has been moved out of that stable range.

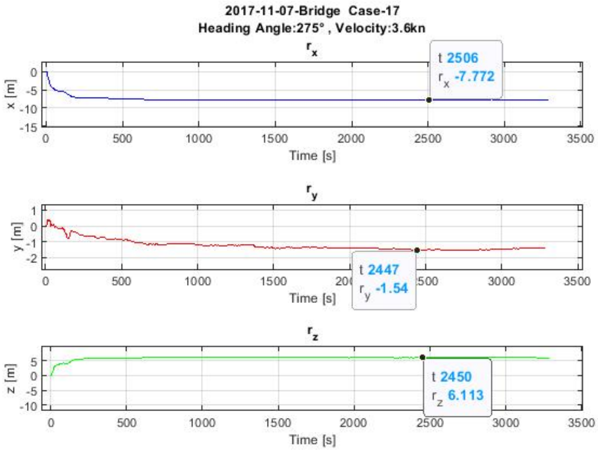

Figure 6.41 Estimated offsets of trial seventeen

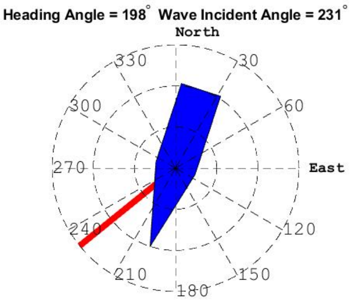

Figure 6.42 Relative sea state of trial twenty-two

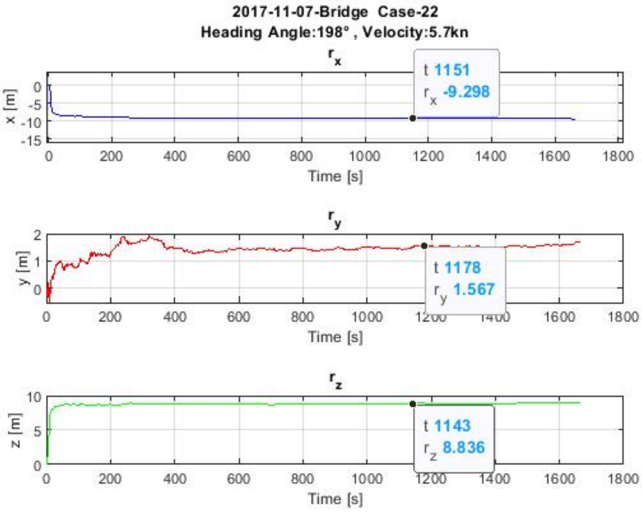

Figure 6.43 Estimated offsets of trial twenty-two

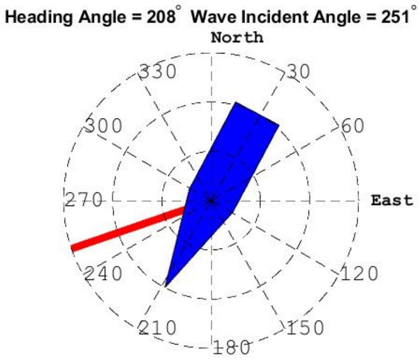

Figure 6.44 Relative sea state of trial twenty-four

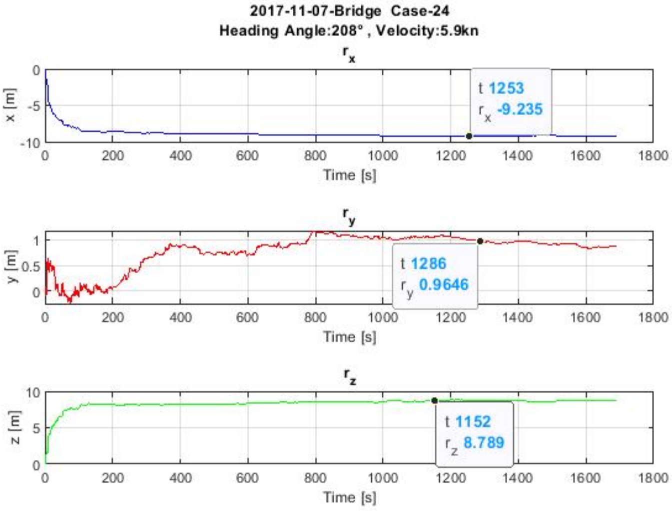

Figure 6.45 Estimated offsets of trial twenty-four

Comparing the portside and starboard side results, a sign change in the offset values in the y-direction is observed; that is, when a wave comes from the portside, the location of the CR moves slightly towards the starboard side and vice versa. Larger offsets values are produced than those from the portside, as indicated by the marked points in the figures, meaning that the CR is far from the CG.

$$P\ 17 = 10^{-4} * \begin{bmatrix} 1 & 0 & 0 & \vdots & 0 & 0 & -1 \\ 0 & 1 & 0 & \vdots & 0 & 0 & 0 \\ 0 & 0 & 1 & \vdots & 1 & -1 & 0 \\ \cdots & \cdots & \cdots & \vdots & \cdots & \cdots & \cdots \\ 0 & 0 & 1 & \vdots & 92 & 31 & 0 \\ 0 & 0 & -1 & \vdots & 31 & 305 & 0 \\ -1 & 0 & 0 & \vdots & 0 & 0 & 83 \end{bmatrix} \begin{bmatrix} [(m/s^2)^2] & [m^2/s^2] \\ [m^2/s^2] & [m^2] \end{bmatrix}$$

$$CC\ 17 = \begin{bmatrix} 1.0000 & -0.3224 & -0.0091 & -0.0396 & -0.0318 & -0.7184 \\ -0.3224 & 1.0000 & -0.0838 & -0.3801 & -0.3097 & 0.2113 \\ -0.0091 & -0.0838 & 1.0000 & 0.1474 & -0.7943 & -0.0583 \\ -0.0396 & -0.3801 & 0.1474 & 1.0000 & 0.2303 & -0.2699 \\ -0.0318 & -0.3097 & -0.7943 & 0.2303 & 1.0000 & -0.2215 \\ -0.7184 & 0.2113 & -0.0583 & -0.2699 & -0.2215 & 1.0000 \end{bmatrix}$$

$$P\,22 = 10^{-4} * \begin{bmatrix} 1 & 0 & 0 & \vdots & 0 & 0 & 1 \\ 0 & 1 & 0 & \vdots & 0 & 0 & 0 \\ 0 & 0 & 1 & \vdots & -1 & -1 & 0 \\ \cdots & \cdots & \cdots & \vdots & \cdots & \cdots & \cdots \\ 0 & 0 & -1 & \vdots & 59 & -28 & 0 \\ 0 & 0 & -1 & \vdots & -28 & 272 & 0 \\ 1 & 0 & 0 & \vdots & 0 & 0 & 53 \end{bmatrix} \begin{bmatrix} [(m/s^2)^2] & [m^2/s^2] \\ [m^2/s^2] & [m^2] \end{bmatrix}$$

$$CC\,22 = \begin{bmatrix} 1.0000 & 0.0253 & 0.2330 & -0.1293 & -0.2735 & 0.7973 \\ 0.0253 & 1.0000 & 0.2119 & -0.1180 & -0.2480 & 0.2088 \\ 0.2330 & 0.2119 & 1.0000 & -0.3043 & -0.4615 & 0.1522 \\ -0.1293 & -0.1180 & -0.3043 & 1.0000 & -0.6443 & -0.0848 \\ -0.2735 & -0.2480 & -0.4615 & -0.6443 & 1.0000 & -0.1827 \\ 0.7973 & 0.2088 & 0.1522 & -0.0848 & -0.1827 & 1.0000 \end{bmatrix}$$

The *P* matrices of trials seventeen and twenty-two presented above show the correlations among the linear accelerations and the offsets, as in the other trials. Again, the more significant errors appear in the offset of the y-axis, with values of approximately 0.17 m. However, based on the curves and marked values shown in the figures, under bow sea conditions, the differences among the estimated results are relatively larger than the impacts of the calculated errors as shown in the *P* matrix. According to the correlation coefficient matrices, strong correlations appear in two pairs. One is between the linear acceleration in the z-direction and the offset in the y-axis. The other is between the linear acceleration for the x-axis and the offset in the z-axis for both trials. However, there is a relatively strong correlation between the x- and y-axis of the offset in trial twenty-two. With more correlations, the estimated offset values would be much more easily affected with more variables.

6.3.2 Analyses of the Complete Results

Table 6.4 shows the complete results from the sea trials implemented on the Simon Stevin. All the sea trials were well-recorded with respect to the encountered wave information and ship velocities. The sea trials under following seas at the portside ranged from one to twenty-three, and those at the starboard side were trials nine and eighteen. Then, the quartering seas at the starboard side occurred in trials nineteen and twenty-six. Trials twenty-five and eleven were under beam seas but on both sides. Bow seas at the portside occurred in trials three to seventeen in the table, and at the starboard side in trials two to twenty-four. The rest of the trials were subjected to head seas. Eight and twenty were at the portside, and the others were at the starboard side. The sixth to the eighth columns show the mean values of the estimated offsets calculated in the range where the curves become stable and smooth. As the CG's location is known from the ship's stability book, and to describe a clear relationship between the CR and CG, the transformation of the offsets to the coordinate system with its origin at the CG is necessary. By subtracting the estimated average offsets values, the distance between the location of CR and the known CG is obtained, as shown in the last three columns of the table.

No.	Heading Angle [°]	Encountering Wave [°]	Relative Direction	Ship Velocity [kn]	Offset Value [m]			Distance between CR and CG [m]		
					r_x	r_y	r_z	x	y	z
1	356	214	Port	6.1	-6.77	0.06	4.79	5.67	1.94	2.20
4	63	256	Port	6.1	-7.04	-0.64	6.07	5.94	2.64	0.92
6	56	264	Port	3.7	-6.88	-0.73	6.12	5.78	2.73	0.87
12	0.7	231	Port	4.2	-6.55	-0.27	4.99	5.45	2.27	2.00
13	27	222	Port	9.5	-7.45	-0.25	5.48	6.35	2.25	1.51
15	45	229	Port	3.7	-6.96	-0.50	5.56	5.86	2.50	1.43
21	23	230	Port	6.3	-6.80	-0.25	5.42	5.70	2.25	1.57
23	34	239	Port	6.1	-6.52	-0.19	5.46	5.42	2.19	1.53
9	95	263	Stb	3.8	-7.26	-0.72	6.94	6.16	2.72	0.05
18	97	262	Stb	3.8	-7.02	-1.11	7.18	5.92	3.11	-0.19
19	145	276	Stb	5.9	-7.92	0.37	6.87	6.82	1.63	0.12
26	107	250	Stb	6.2	-7.06	-0.27	5.61	5.96	2.27	1.38
25	347	249	Port	6	-6.85	-0.38	5.16	5.75	2.38	1.83
11	134	239	Stb	3.9	-7.61	-0.49	7.22	6.51	2.49	-0.23
3	296	252	Port	5.8	-8.03	-1.90	6.68	6.93	3.90	0.31
10	299	251	Port	3.8	-6.83	-0.08	4.99	5.73	2.08	2.00
17	275	232	Port	3.6	-7.75	-1.38	6.06	6.65	3.38	0.93
2	176	221	Stb	6.7	-8.61	0.65	7.67	7.51	1.35	-0.68
7	211	267	Stb	11.4	-8.54	1.01	6.90	7.44	0.99	0.09
14	181	232	Stb	3.8	-7.61	0.18	7.02	6.51	2.18	-0.03
22	198	231	Stb	5.7	-9.22	1.48	8.82	8.12	0.52	-1.83
24	208	251	Stb	5.9	-9.17	1.00	8.67	8.07	1.00	-1.68
8	270	262	Port	3.9	-7.02	-0.47	5.93	5.92	2.47	1.06
20	247	225	Port	9.7	-8.80	-1.84	7.57	7.70	3.84	-0.68
5	235	251	Stb	3.3	-7.92	-0.10	7.83	6.82	2.10	-0.84
16	226	229	Stb	4	-7.86	-0.37	6.82	6.76	2.37	0.17

Table 6.4 CR results of Simon Stevin

Depending on the various encountered waves, the offset values vary as well. The estimated CR location appears relatively steady when comparing the results taken under similar external conditions, such as sea trials twenty-one and twenty-three. In total, no significant differences exist in the x- and z-direction. Thus, the offset in the x-axis is normally around 6 m, ahead of the CG, except for a few bow seas cases. Most of the cases in the y-direction are positive, which indicates that the CR is on the portside of the CG. In trials twenty-two and twenty-four, the values are much smaller than the others, and this situation has no relevance with the velocity in comparison with the others. There is no symmetry in the y-axis. When investigating in the z-direction, the range is not particularly stable. Under the influence of the ship's various velocities and encountered waves, certain results change signs, and even the absolute values have changed significantly. Drift of up to 2 m occurs in some cases. However, most of the negative values appear when waves approach from the starboard, regardless of the velocity.

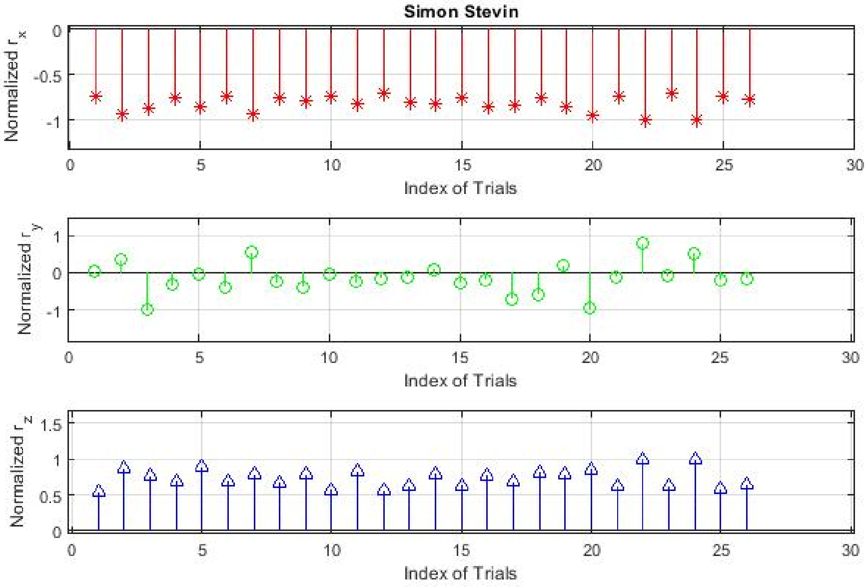

Figure 6.46 Normalization of the offset for Simon Stevin

After normalizing the estimated offset results from Table 6.4, the relevant curves are shown in Figure 6.46. The offset in the x-direction is rather similar and stable, but a stronger oscillation appears in the z-direction. Still, it is appropriate to conclude that the offset in the x- and z-axis can be determined to move within a small range. Again, in the y-direction, the values show variation on both sides, but still, a few stable cases could be observed in the earlier trials.

The various velocities and wave conditions cause variations in the estimated offset values. However, not all problems observed in the table can be solved by such simple arguments. The encountered waves were shorter than the ship's length, thus enhancing the complexity and variety of the ship's motions. Moreover, because the characteristics of waves are mainly in the information of the peak incidence, the actual waves' complexity with a broader spread of angles and frequencies has been reduced. Furthermore, rudder actions by autopilot may have more influence on a small ship in the open sea. In summary, the actual sea state is too complex to consider all the realistic factors. Certain assumptions and simplifications are required to achieve the specific research purposes. Hence, some unsatisfied or unsolved results should be accepted. In general, though, the estimated offset values show a certain systematic nature, moving within a specific range in short adjustment times. For each trial with a nearly constant condition, a unique location of the CR is produced. Compared with the location of the known CG, the location of the CR is in front, slightly portside, and higher; based on the ship layout, this result is credible.

6.4 Results of Agulhas II

The experiments were performed in the summer of 2017 because it was quite a long voyage, and the sensor boxes were functioning when they were installed onboard. It is necessary to select several parts of the available recorded data to avoid undesired and redundant information and errors, and then the selected parts of data are utilized to estimate the location of the CR. On this ship, there were two sensor boxes installed at entirely different locations onboard. Therefore, it is necessary to process the measured data from both sensors to select the common, valid, and overlapped parts at first. Then, the time-synchronized parts for both sensors must be identified from the selected parts of data to make complete and proper preparations for the determination algorithm.

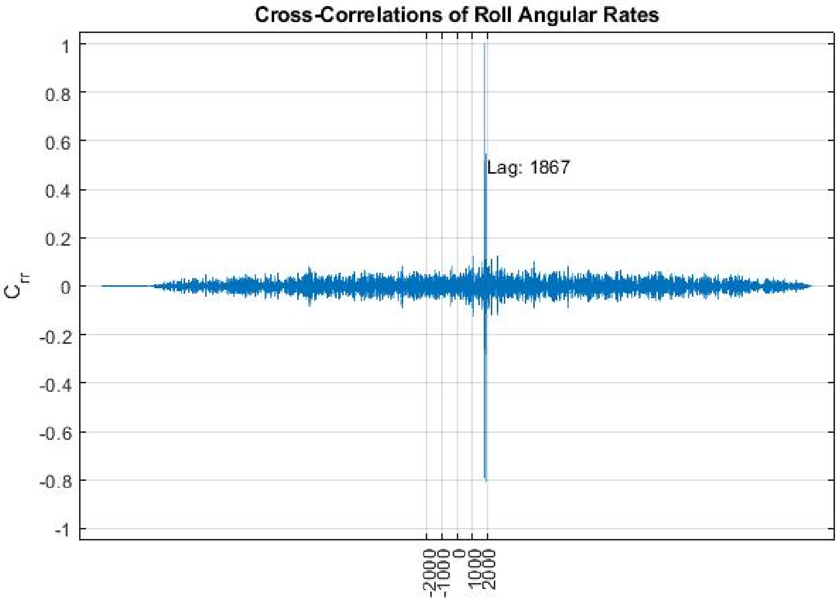

Figure 6.47 Lag of roll angular rates

The first step is to reduce the sampling frequency to 2 Hz, as the two sensor boxes have different recording frequencies, 10 Hz and 8 Hz, because it is likely to compare different recorded data under the same frequency when trying to find the synchronized parts. Based on the assumption that the ship body is rigid, every point's angular rate should be the same. Hence, the angular rates of both sensors should be identical as well. Thus, after down-sampling the original data, it is feasible to find out the identical parts of the angular rates of both sensors; that is, the synchronized parts of both sensor boxes are determined. As shown in Figure 6.47, the lag between these two sensor boxes is found. Then, the synchronized parts are found by aligning one sensor with the other according to this lag. As shown in Figure 6.48, the identical parts of the roll angular rates are expressed after down-sampling to 2 Hz, and the time intervals are also acquired. Finally, the corresponding data for these obtained time intervals are the synchronized parts as expected.

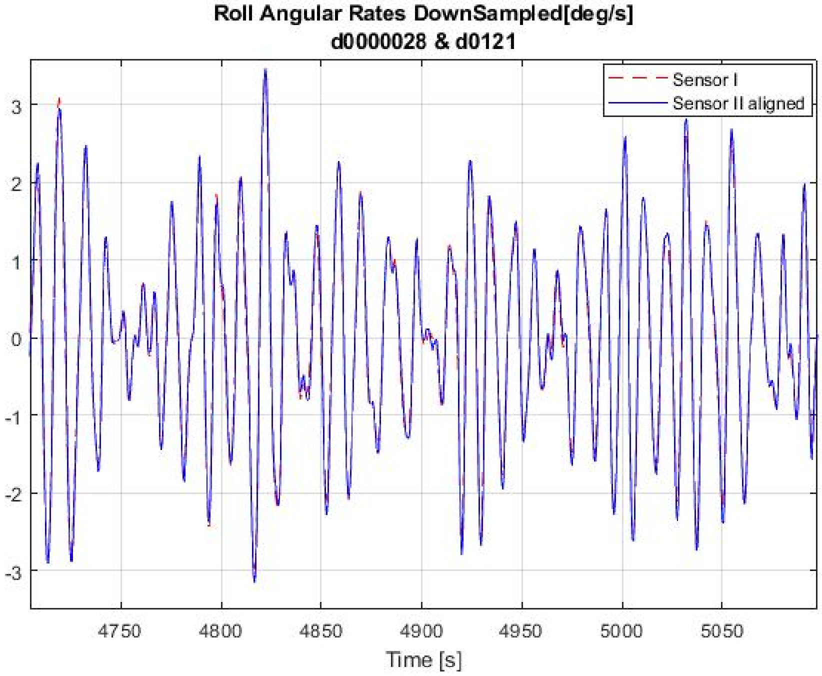

Figure 6.48 Synchronized part for both sensors after down-sampling

6.4.1 Analyses of Several Trials

Figures 6.49 and 6.51 express the relationship between heading angles and incident waves quartering from the portside. On the Agulhas II, there were two sensor boxes onboard, marked as sensors I and II. As shown in Figures 6.50 and 6.52, the estimated offset values for both sensor boxes are quite oscillatory but arrive at essentially stable ranges instead of constant values. In comparison, sensor II has better and more stable results. The curves of sensor II quickly reach the stable range and then oscillate. Thus, the overshooting time for sensor II is relatively shorter than that for sensor I. Comparing the curves in three dimensions respectively, corresponding curves are similar for these two trials. That is, the results of the x offsets are similar for both trials for sensor I, and likewise for the other results. Second, the shapes of curves in the y-direction are almost identical in both sensors for both trials. Thus, the similar results would be generated.

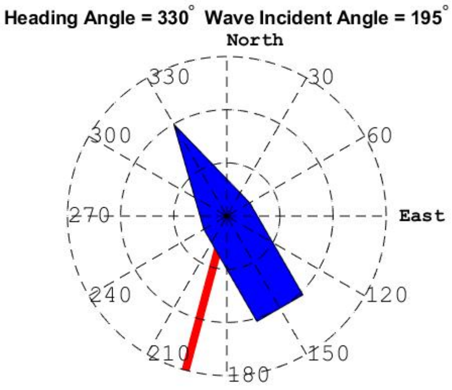

Figure 6.49 Relative sea state of trials 28 and 121

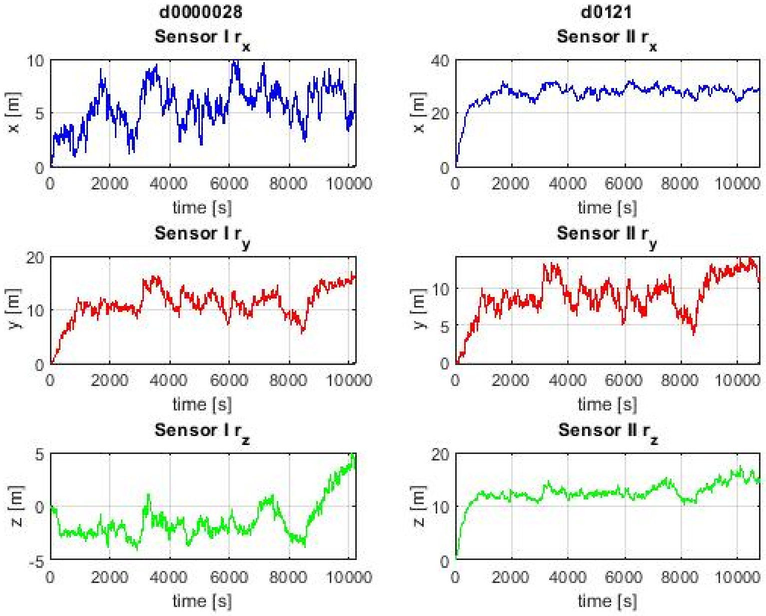

Figure 6.50 Estimated offsets of trials 28 and 121

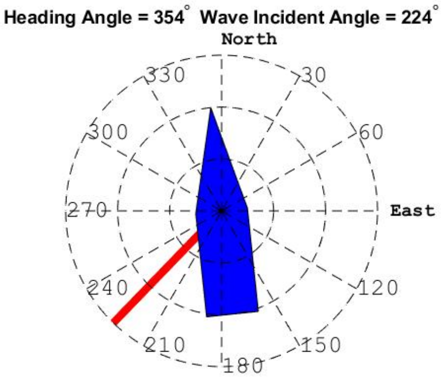

Figure 6.51 Relative sea state of trials 38 and 135

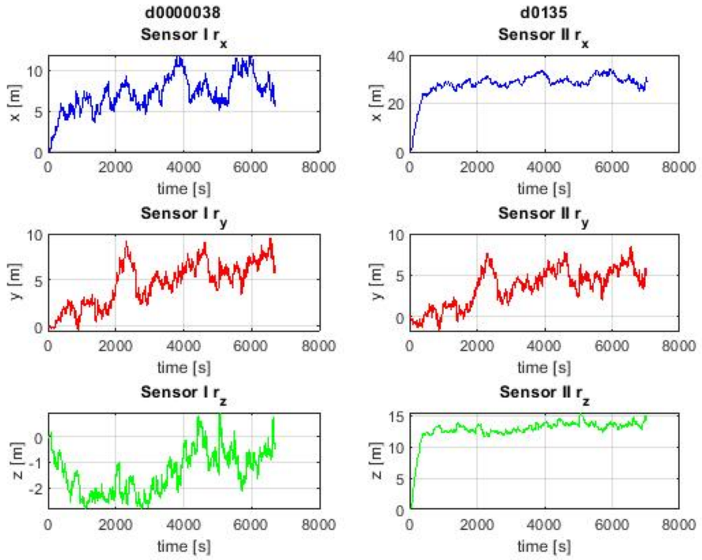

Figure 6.52 Estimated offsets of trials 38 and 135

$$P\,28 = 10^{-4} * \begin{bmatrix} 1 & 0 & 0 & \vdots & 0 & 0 & 8 \\ 0 & 2 & 0 & \vdots & 0 & 0 & 55 \\ 0 & 0 & 3 & \vdots & -25 & -83 & 0 \\ \cdots & \cdots & \cdots & \vdots & \cdots & \cdots & \cdots \\ 0 & 0 & -25 & \vdots & 3754 & 535 & 1 \\ 0 & 0 & -83 & \vdots & 535 & 3572 & 2 \\ 8 & 55 & 0 & \vdots & 1 & 2 & 2487 \end{bmatrix} \begin{bmatrix} [(m/s^2)^2] & [m^2/s^2] \\ [m^2/s^2] & [m^2] \end{bmatrix}$$

$$P\,121 = 10^{-4} * \begin{bmatrix} 1 & 0 & 0 & \vdots & 0 & 0 & 7 \\ 0 & 1 & 0 & \vdots & 0 & 0 & 14 \\ 0 & 0 & 1 & \vdots & -12 & -22 & 0 \\ \cdots & \cdots & \cdots & \vdots & \cdots & \cdots & \cdots \\ 0 & 0 & -12 & \vdots & 2801 & 320 & -2 \\ 0 & 0 & -22 & \vdots & 320 & 2724 & -2 \\ 7 & 14 & 0 & \vdots & -2 & -2 & 1909 \end{bmatrix} \begin{bmatrix} [(m/s^2)^2] & [m^2/s^2] \\ [m^2/s^2] & [m^2] \end{bmatrix}$$

$$CC\,28 = \begin{bmatrix} 1.0000 & 0.9938 & 0.2716 & -0.2633 & -0.2436 & 0.9945 \\ 0.9938 & 1.0000 & 0.2700 & -0.2431 & -0.2447 & 0.9998 \\ 0.2716 & 0.2700 & 1.0000 & -0.2516 & -0.9877 & 0.2589 \\ -0.2633 & -0.2431 & -0.2516 & 1.0000 & 0.0976 & -0.2374 \\ -0.2436 & -0.2447 & -0.9877 & 0.0976 & 1.0000 & -0.2342 \\ 0.9945 & 0.9998 & 0.2589 & -0.2374 & -0.2342 & 1.0000 \end{bmatrix}$$

$$CC\,121 = \begin{bmatrix} 1.0000 & 0.9869 & 0.3346 & -0.2667 & -0.2683 & 0.9906 \\ 0.9869 & 1.0000 & 0.3183 & -0.2512 & -0.2563 & 0.9977 \\ 0.3346 & 0.3183 & 1.0000 & -0.4610 & -0.9015 & 0.2862 \\ -0.2667 & -0.2512 & -0.4610 & 1.0000 & 0.0335 & -0.2299 \\ -0.2683 & -0.2563 & -0.9015 & 0.0335 & 1.0000 & -0.2297 \\ 0.9906 & 0.9977 & 0.2862 & -0.2299 & -0.2297 & 1.0000 \end{bmatrix}$$

As expressed in the P matrices, *P28* is the error covariance matrix calculated from sensor I, and *P121* is that from sensor II. Here, 28 and 121 are the sea trial numbers recorded from sensors I and II, respectively, and they are treated as a synchronized pair. The offset in the z-direction is related not only to the linear acceleration in the x-direction, but also to that in the y-direction. Of course, the remaining components of the offset are related to the linear acceleration in the z-direction. All these correlations are based on the constructed mathematical model. The correlations among the state variables are much stronger than those from other employed ships. For example, 0.032 is the correlation coefficient of the offset in the x- and y-direction. Nevertheless, the largest covariances appear in the offset part. The corresponding errors are then at 0.613, 0.597, and 0.498 m for sensor I, and 0.529, 0.522, and 0.437 m for sensor II in three dimensions, respectively. With such significant error amplitudes, it is inevitable that the estimated offset would vary accordingly and that the offsets would be more oscillatory in the figures.

Furthermore, based on the correlation coefficient matrices *CC28* and *CC121*, strong correlations appear more frequently than for other ships. According to the mathematical model, the correlations of offset in the z-axis and linear accelerations in the x- and y-direction are probable and plausible. At the same time, it is also reasonable that the linear acceleration in the z-direction correlates with the offset in the x- and y-axis. However, the offset in the x- and y-direction are strongly correlated, while the linear accelerations in the x- and y-axis are correlated as well. With many such correlations, the estimated offset values would be easily affected by any changes, leading to oscillatory results.

$$P\,38 = 10^{-4} * \begin{bmatrix} 1 & 0 & 0 & \vdots & 0 & 0 & 5 \\ 0 & 1 & 0 & \vdots & 0 & 0 & -5 \\ 0 & 0 & 1 & \vdots & -4 & 10 & 0 \\ \cdots & \cdots & \cdots & \vdots & \cdots & \cdots & \cdots \\ 0 & 0 & -4 & \vdots & 1864 & 433 & 0 \\ 0 & 0 & 10 & \vdots & 433 & 3838 & 3 \\ 5 & -5 & 0 & \vdots & 0 & 3 & 1615 \end{bmatrix} \begin{bmatrix} [(m/s^2)^2] & [m^2/s^2] \\ [m^2/s^2] & [m^2] \end{bmatrix}$$

$$P\,135 = 10^{-4} * \begin{bmatrix} 1 & 0 & 0 & \vdots & 0 & 0 & -14 \\ 0 & 1 & 0 & \vdots & 0 & 0 & 10 \\ 0 & 0 & 1 & \vdots & 13 & -18 & 0 \\ \cdots & \cdots & \cdots & \vdots & \cdots & \cdots & \cdots \\ 0 & 0 & 13 & \vdots & 1440 & 479 & 2 \\ 0 & 0 & -18 & \vdots & 479 & 2728 & 3 \\ -14 & 10 & 0 & \vdots & 2 & 3 & 1170 \end{bmatrix} \begin{bmatrix} [(m/s^2)^2] & [m^2/s^2] \\ [m^2/s^2] & [m^2] \end{bmatrix}$$

$$CC\,38 = \begin{bmatrix} 1.0000 & -0.9768 & -0.1232 & -0.3075 & -0.2589 & 0.9832 \\ -0.9768 & 1.0000 & 0.0929 & 0.1915 & 0.1773 & -0.9850 \\ -0.1232 & 0.0929 & 1.0000 & -0.3515 & 0.8726 & -0.1138 \\ -0.3075 & 0.1915 & -0.3515 & 1.0000 & 0.1447 & -0.2503 \\ -0.2589 & 0.1773 & 0.8726 & 0.1447 & 1.0000 & -0.2244 \\ 0.9832 & -0.9850 & -0.1138 & -0.2503 & -0.2244 & 1.0000 \end{bmatrix}$$

$$CC\,135 = \begin{bmatrix} 1.0000 & -0.9952 & -0.0188 & 0.2544 & 0.2003 & -0.9977 \\ -0.9952 & 1.0000 & 0.0397 & -0.2989 & -0.2551 & 0.9961 \\ -0.0188 & 0.0397 & 1.0000 & 0.3790 & -0.7644 & 0.0410 \\ 0.2544 & -0.2989 & 0.3790 & 1.0000 & 0.3060 & -0.2688 \\ 0.2003 & -0.2551 & -0.7644 & 0.3060 & 1.0000 & -0.2342 \\ -0.9977 & 0.9961 & 0.0410 & -0.2688 & -0.2342 & 1.0000 \end{bmatrix}$$

A similar set of correlations is expressed as for the former trial with the *P* and *CC* matrices for another sea trial pair, 38 and 135. The same correlation pairs appear as for trials 28 and 121, except for the offset in the x- and y-axis. Moreover, the most significant errors are found in the y-direction of the offset, which indicates more vibrations would occur in that variable.

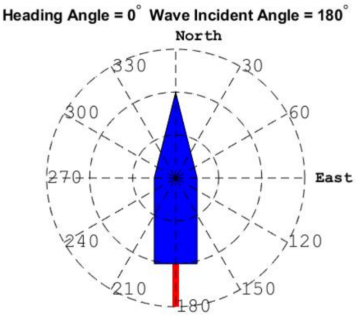

Figure 6.53 Relative sea state of trials 43 and 145

Figure 6.53 shows a precise following sea state, and the results of the offsets oscillate before entering a stable range, as shown in Figure 6.54. The offsets from sensor I show a better adjusting process than the quartering sea trials mentioned above, by first undergoing a period of adjustment and then reaching a stable range instead of oscillating continually. Nevertheless, a longer time is required before the offset values enter their relatively stable ranges for sensor II compared with the previous trials. One possible reason for this phenomenon is the effect of the following seas. These have less influence and less significant effects on the ship than quartering seas or bow seas. Hence, finding the location would require a longer time. The shapes and values of the curves in the y-direction for both sensors appear similar to those of other trials. However, there are significant differences in the shapes and values for the x- and z-direction, respectively, particularly for the z-direction, which are quite unlike the other trials.

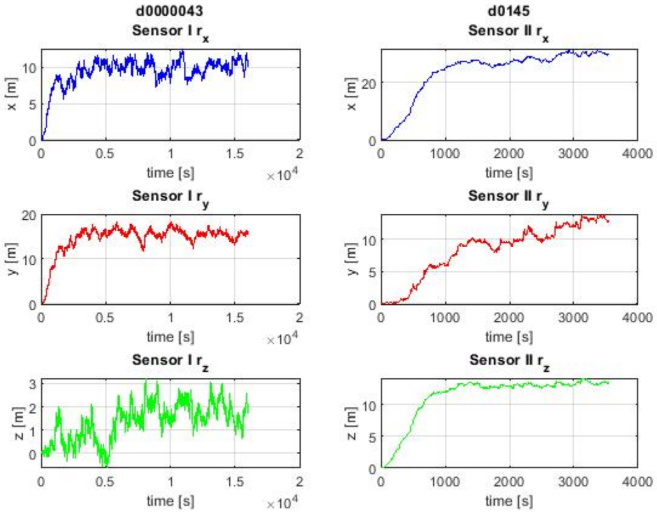

Figure 6.54 Estimated offsets of trials 43 and 145

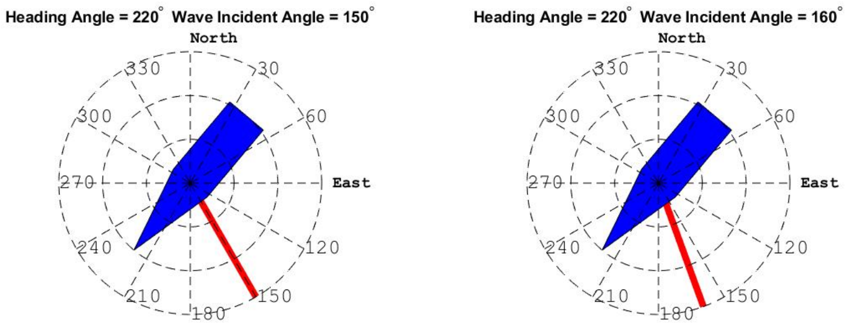

Figure 6.55 Relative sea state of trials 10 and 44 as well as 10 and 80

The sea trials described in Figure 6.55 encountered bow seas from the portside. Because dataset ten was recorded over a long period, two synchronized datasets from sensor II could be matched with it. These two datasets were under almost identical sea conditions, with only a 10° difference in the heading angle. The same features are revealed in Figures 6.56 and 6.57 as in the previous sea trials:

1. Most of the curves take a period for adjustments, and then arrive in a relatively stable range for each variable.

2. The offset results in the y-direction are almost identical for both sensors, either in terms of their shapes or values.

3. Enormous variances in the z offsets' characteristics, with similarities in neither the shapes nor the values.

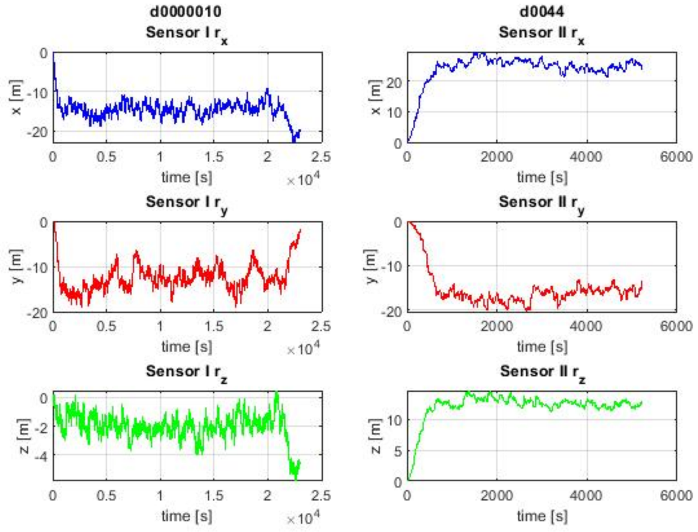

Figure 6.56 Estimated offsets of trial 10 and 44

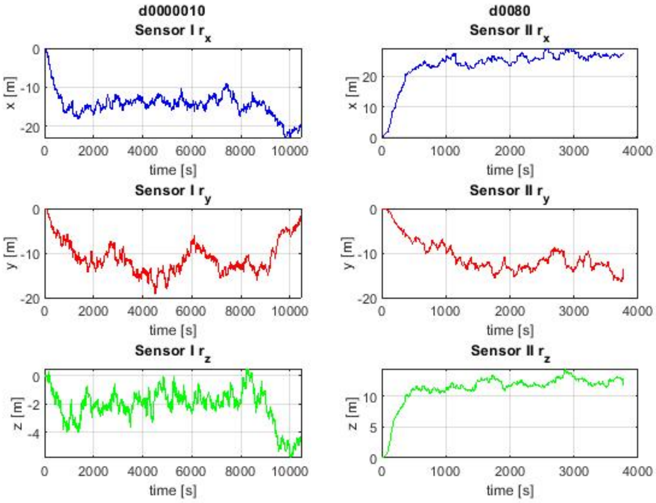

Figure 6.57 Estimated offsets of trials 10 and 80

Judging from the *P* matrices of these two pairs of sea trials, there are no significant differences from other trials, such as the same correlation patterns and rather significant errors in the offset parts, leading to oscillations in the curves. However, the estimated values are quite unlike those of other trials.

$$P\,10 = 10^{-4} * \begin{bmatrix} 1 & 0 & 0 & \vdots & 0 & 0 & 19 \\ 0 & 1 & 0 & \vdots & 0 & 0 & 4 \\ 0 & 0 & 1 & \vdots & -22 & 7 & 0 \\ \cdots & \cdots & \cdots & \vdots & \cdots & \cdots & \cdots \\ 0 & 0 & -22 & \vdots & 3482 & 48 & -1 \\ 0 & 0 & 7 & \vdots & 48 & 5494 & 4 \\ 19 & 4 & 0 & \vdots & -1 & 4 & 2954 \end{bmatrix} \begin{bmatrix} [(m/s^2)^2] & [m^2/s^2] \\ [m^2/s^2] & [m^2] \end{bmatrix}$$

$$P\,44 = 10^{-4} * \begin{bmatrix} 1 & 0 & 0 & \vdots & 0 & 0 & 12 \\ 0 & 1 & 0 & \vdots & 0 & 0 & -3 \\ 0 & 0 & 1 & \vdots & -14 & 6 & 0 \\ \cdots & \cdots & \cdots & \vdots & \cdots & \cdots & \cdots \\ 0 & 0 & -14 & \vdots & 1673 & 74 & -2 \\ 0 & 0 & 6 & \vdots & 74 & 2660 & 3 \\ 12 & -3 & 0 & \vdots & -2 & 3 & 1402 \end{bmatrix} \begin{bmatrix} [(m/s^2)^2] & [m^2/s^2] \\ [m^2/s^2] & [m^2] \end{bmatrix}$$

$$P\,80 = 10^{-4} * \begin{bmatrix} 1 & 0 & 0 & \vdots & 0 & 1 & 11 \\ 0 & 1 & 0 & \vdots & 0 & 0 & -18 \\ 0 & 0 & 1 & \vdots & -14 & 35 & 0 \\ \cdots & \cdots & \cdots & \vdots & \cdots & \cdots & \cdots \\ 0 & 0 & -14 & \vdots & 1758 & 86 & 2 \\ 1 & 0 & 35 & \vdots & 86 & 2751 & -3 \\ 11 & -18 & 0 & \vdots & 2 & -3 & 1435 \end{bmatrix} \begin{bmatrix} [(m/s^2)^2] & [m^2/s^2] \\ [m^2/s^2] & [m^2] \end{bmatrix}$$

$$CC\,10 = \begin{bmatrix} 1.0000 & -0.9765 & 0.1230 & -0.2073 & -0.2174 & 0.9988 \\ -0.9765 & 1.0000 & -0.1158 & 0.1682 & 0.1272 & -0.9747 \\ 0.1230 & -0.1158 & 1.0000 & -0.9634 & 0.4324 & 0.1248 \\ -0.2073 & 0.1682 & -0.9634 & 1.0000 & -0.1774 & -0.2038 \\ -0.2174 & 0.1272 & 0.4324 & -0.1774 & 1.0000 & -0.2015 \\ 0.9988 & -0.9747 & 0.1248 & -0.2038 & -0.2015 & 1.0000 \end{bmatrix}$$

$$CC\ 44 = \begin{bmatrix} 1.0000 & -0.9704 & 0.1126 & -0.2435 & -0.2165 & 0.9970 \\ -0.9704 & 1.0000 & -0.0898 & 0.1704 & 0.1187 & -0.9684 \\ 0.1126 & -0.0898 & 1.0000 & -0.9331 & 0.4720 & 0.0908 \\ -0.2435 & 0.1704 & -0.9331 & 1.0000 & -0.1282 & -0.2130 \\ -0.2165 & 0.1187 & 0.4720 & -0.1282 & 1.0000 & -0.2054 \\ 0.9970 & -0.9684 & 0.0908 & -0.2130 & -0.2054 & 1.0000 \end{bmatrix}$$

$$CC\ 80 = \begin{bmatrix} 1.0000 & -0.9956 & -0.0682 & -0.2374 & -0.1581 & 0.9951 \\ -0.9956 & 1.0000 & 0.1075 & 0.1735 & 0.1804 & -0.9988 \\ -0.0682 & 0.1075 & 1.0000 & -0.5704 & 0.9470 & -0.1195 \\ -0.2374 & 0.1735 & -0.5704 & 1.0000 & -0.2772 & -0.1820 \\ -0.1581 & 0.1804 & 0.9470 & -0.2772 & 1.0000 & -0.1973 \\ 0.9951 & -0.9988 & -0.1195 & -0.1820 & -0.1973 & 1.0000 \end{bmatrix}$$

The correlations of these two pairs are similar to those of the aforementioned sea trials. Strong correlations appear in four places. The first is between the linear accelerations in the x- and y-direction and the second is between the linear acceleration in the z-direction and offset in the y-axis. The remaining correlations are between the linear accelerations in these two directions and the offset in the z-axis. As discussed previously, these strong correlations would have significant effects on the estimated offset values.

Comparing the stable values of each offset, these two bow seas trials are considerably divergent from other trials, as the offsets in the x-direction for sensor I are negative with large amplitudes, which indicates that the sensor is behind the CR, in contrast to the other sea state trials, and this divergence appears in the y-direction for both sensors as well.

6.4.2 Analyses of the Complete Results

Table 6.5 shows the results of distances between the CR and CG from the two sensor boxes onboard. The contents of the first column are the matched datasets from the two sensors, namely the selected parts of data when both sensors were working normally and recording motion information as expected. The second and third columns describe the relative angles and positions between all current encountered waves and the ship's current heading angles. Sensor I was placed in the engine room, at a position estimated as (-8, 0, 0) m in a coordinate system with CG as the origin. Thus, sensor I was behind the CG. Sensor II was on the observation deck, and its position was measured as (12.7, 0, 22.3) m in the same coordinate system as sensor I. The following six columns are the relative locations between the CR and CG for both sensors in three dimensions. The data in Table 6.5 show that with encountered waves coming from the portside, the location of the CR shifts towards the starboard side from the midship plane in most of the trials, which intuitively seems to be plausible.

Both sensors should yield consistent results, which means that the values from the last six columns should be identical or at least similar when they refer to similar parameters. However, depending on the different encountered waves and ship velocities, some trials are similar as expected, whereas others seem to be outliers. In addition, based on the *P* matrices, the offset errors vary dramatically during the calculation, while many correlations appear in the *CC* matrices, which have caused oscillations during the estimation process, leading to various values of the estimated offset for each time and further affecting the averaged estimated offset values. Thus, the outliers or strange values would appear even under similar sea state conditions.

For the trials from the second row to the fourth row, the ship encountered quartering seas, and the relative distances showed in the table are not the same. Each sea trial has its unique position of the CR, but overall, the CR is placed to the starboard from midships when encountered waves approach from the portside. In the x-direction, a constant deviation of approximately 1 m between the two sensors appears, but a larger deviation of up to 4 m appears among all distances for the x-axis. On one aspect, when considering the calculated errors from the *P* matrices, the errors could go up to 0.6 m. Thus, the actual calculated values of the offset may have a difference up to approximately 1.2 m. On another aspect, with respect to the ship's length, a discrepancy of a few meters is not that severe. Hence, a deviation of approximately two or three meters is acceptable for the x-direction.

In the y-direction, the estimated positions obtained for both sensors are relatively similar, although they vary among the trials. The differences between the two sensors can be surmised to be the effects of the *P* matrices' calculation errors. However, among all sea trials, the broad variation of the values would be caused by the encountered waves.

There is a systematic discrepancy in the z-axis between both sensors. The estimated location of the CR is higher for sensor II than sensor I, in contrast to the similar values in the x-direction. A preliminary analysis indicates that the reason for this discrepancy might be that the lateral accelerations could be corrupted by the comparatively large gravitational acceleration, on which the estimated z-component is mainly dependent. In addition, minor errors in the angles when entering the transformation should be considered. Moreover, calculation errors would have affected the values as well, but not in a dominant way.

When the ship was in the process of dynamic positioning, the values in the table could be treated as outliers by comparison with other trials. Inconsistency in all three dimensions with other trials indicates that the ship's velocity has a certain degree of influence on determining the CR's location. Moreover, a thruster activity might have altered the ship's dynamic behaviour and then led to these locations. Case 43&145 shows the results of following seas, with similar values as quartering seas but with a lower z-component of the location from sensor I. Significant differences appear between both sensors, up to 5 m. These would be abnormal, though. Considering the characteristics of following seas, the magnitudes of the ship's behaviour would be enhanced. Thus, the amplitudes of the estimated locations have been enlarged as well.

Most strange results were observed in the sea trials with bow seas, as illustrated in the last row of Table 6.5. Complete relative positions were estimated from these two sensors, and then similar values were produced in comparison with the same sensor between these two trials. These results suggest that under a similar sea environment, similar estimated offset values would be generated as well. However, the situation with bow seas seems to be much more complicated. The ship's behaviour would be complex and strongly coupled in that case. Therefore, the location component of the CR in the y-direction estimated from the two sensors is always on the CG's portside, in contrast to the other trials. Furthermore, the relative positions in the x-direction from both sensors are dramatically diverse, from ahead of the CG to behind it. The reason for these seemingly random and weird values would be the coupled ship motions caused by the bow seas. The determination algorithm is not able to separate ship motions thoroughly, thus leading to greater uncertainties in determining the locations of the CR and affecting the final positions.

In general, the results shown in the figures or illustrated from the table have proved that each sea trial could obtain a unique location of the CR. When the ship encountered similar sea states, the similar locations of CR could be acquired by different sea trials. Nevertheless, instead of being identical, there are differences between the results generated by the two sensor boxes for each trial, which the remaining statistical uncertainty cannot explain. Yet, the location of the CR defined in this work is not a fixed point in the Agulhas but an approximated range. Rapid variations may appear within a wave period or an eigen period of ship motion. Thus, the instantaneous CR would probably vary when a wave's slope reaches the portside or starboard side of the ship. The relative positions in the x- and y-direction seem to agree better between the two sensors than those in the z-direction. Excessively high values were obtained from sensor II, along with those systematic discrepancies. Because the ship's speed and the wave incidence angle can lead to the different characteristics of the CR, they would have impacts on the values in sensor II as well, but not primarily. The probable reason for this would be the large difference between the locations of these two sensors, 20 m in the vertical direction. Such a great height difference is easily affected by the gravitational acceleration, and this enhances or corrupts lateral accelerations, on which the estimated z-coordinate is mainly dependent. Considering the RAOs of ship motions at a speed of 7 kn, after comparing with several waves' directions, the ship's sensitivity range is between 0.05 and 0.1 Hz. Enormous amplitudes appear in the roll motion, indicating that the encountered waves affect the roll motion strongly in this sensitivity range, and leading to obvious roll motions that can affect the offset in the z-direction. In this situation, a longer ship encounters longer waves, and ship motions are more complicated and irregular, especially when the lengths are close. A more detailed investigation into this problem is on-going.

Data Set	Relative Angle [°]	Wave and Ship Relative Direction	Ship Velocity [kn]	CR by Sensor I [m]			CR by Sensor II [m]		
				x	y	z	x	y	z
25&118	130	Port	0 (DP)	-4.82	-0.91	10.79	-10.38	-9.82	18.80
28&121	135	Port	7.5	-13.95	-11.37	1.73	-15.37	-9.19	9.56
36&130	170	Port	14.1	-18.23	-4.29	0.35	-19.10	-3.88	7.08
38&135	130	Port	9.9	-16.06	-5.92	1.20	-16.90	-4.69	9.13
43&145	180	/	12.8	-17.97	-15.47	-1.81	-15.59	-10.36	9.18
10&44	70	Port	8.7	6.53	12.66	1.97	-12.67	16.62	9.55
10&80	60	Port	8.7	6.15	12.42	1.78	-13.02	11.97	10.26

Table 6.5 CR results of Agulhas II

6.5 Results of Catamaran Willi

Two sets of experiments were implemented for the catamaran: those performed at the indoor basin and those at a harbour nearby along the river Hunte.

6.5.1 Results in the Manoeuvre Basin

Owing to the basin's size limitation, each experiment could only last for a few minutes, even including turnings and the round trip. Therefore, it is possible that the CR's location could not be identified owing to such short-duration experiments. The sensor was placed precisely at the centre zone of the upper platform on the Willi. Hence, the vertical distance between the sensor and the bottom of the Willi was 0.59 m, the longitudinal position was 0.54 m from the bow, and 0 m in the transverse direction, namely at the midships.

Figure 6.58 shows the case of the Willi making a round trip, by first adjusting its position to the edge of the wider part of the basin, moving straight ahead until the other side of the basin, and then turning back to its place of departure. The first part of the curves for all dimensions shows strong oscillations before adjusting to relatively steady values. This phenomenon is caused by the propellers in the stern on both sides when the ship is accelerating. In the final phase, the curves seem to be unstable and non-convergent again. Because the catamaran was trying to return to its departure point and making turns for a while, the full details of the procedure could not be completely revealed within such a short experimental period. A small change could result in a significant difference in that scenario. Furthermore, there was insufficient time to fix and readjust the difference, which could even lead to an opposite result as before. Thus, the expectation of achieving converged estimated offsets would be realized by implementing a longer experimental period.

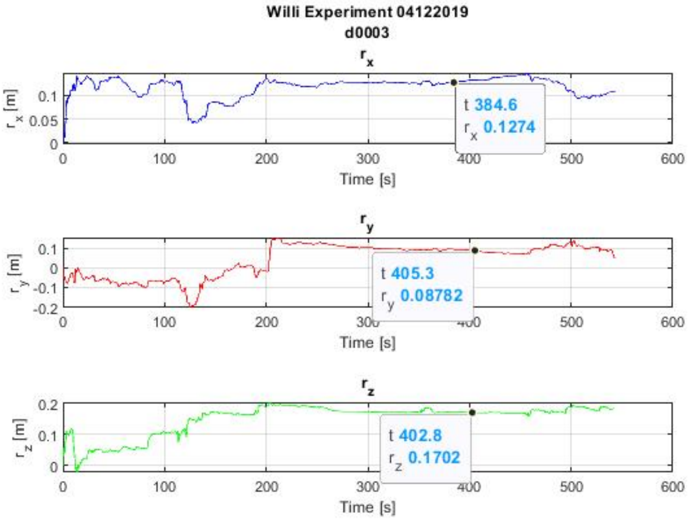

Figure 6.58 Estimated offsets of trial three

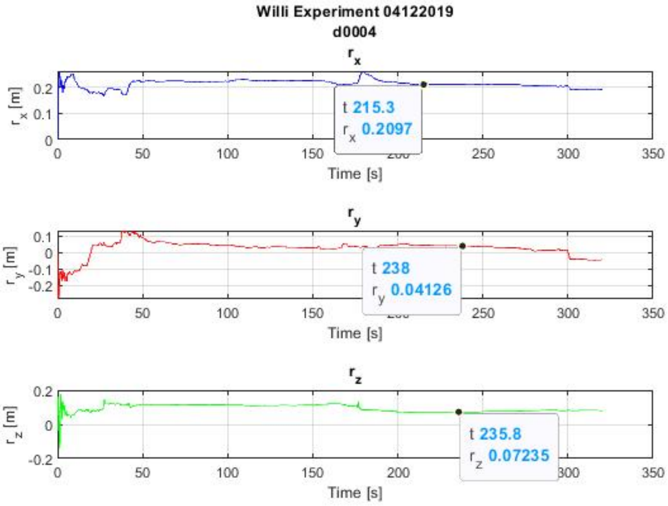

Figure 6.59 Estimated offsets of trial four

Figure 6.59 shows the results from a trial in which the catamaran moved freely, affected by the residual waves caused by the previous behaviour, drifting and rotating without any external power. Before reaching the stable range of estimated offsets, there is time to adjust the results into their ideal values, as with other trials illustrated previously. During the rest of the rather stable phases, the outlier that appeared in the middle of the curve for the z-direction reduced the following estimated value. Still, the outliers in other directions did not change the tendency by the end of the experiment. Because the catamaran was operating and stopped without any contribution from itself, certain strange behaviours may appear in the terminal motion. As in the other trials on different ships, usually, the voyage to go out and return would not be considered because there are too many uncertainties and disturbances.

6.5.2 Results at the Yachthafen

The nearest, larger and available water field to perform more realistic experiments for the catamaran Willi is the Yachthafen along the river Hunte. The sensor box was well-fixed on the upper platform of the Willi and then carried out to the assigned experiment site. No additional ships or vessels were traveling in water field during the experiment. Therefore, the encountered waves were only due to wind sea.

The procedure was separated into three parts, making turns along the portside or starboard side, making circles in the clockwise and counter-clockwise directions, and moving straight ahead. The catamaran was equipped with two propellers in the stern as the main power supplement. In most experimental procedures, the propellers should be working and accelerated from time to time to maintain continuous and relatively stable motions.

Figure 6.60 shows the results when the Willi was turning along the starboard side. The parts with many tiny oscillations indicate that the propellers are actively working to maintain the motion. Thus, adjustments appear in those periods. When the catamaran is turning regularly with an almost constant velocity, the offset values become stable. Even after a period of acceleration, the offsets return to the former values.

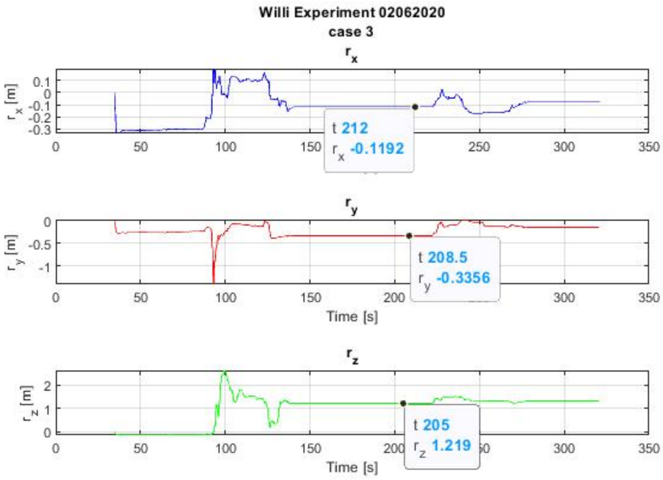

Figure 6.60 Estimated offsets of case three

Between the two manoeuvres, there is always a rest gap for the catamaran. On the one hand, it is to separate each trial easily when processing the measured sensor data, and on the other hand, to let the catamaran settle to make sure that there are no remaining influences from the former trials. Figure 6.61 clearly shows the information about this gap during which the catamaran is drifting freely. As shown in the figure, the offset values are significantly different from case three, and slight vibrations appear. Without the impact of power, the catamaran encountered relatively steady and clear waves. Therefore, massive changes would not be aroused.

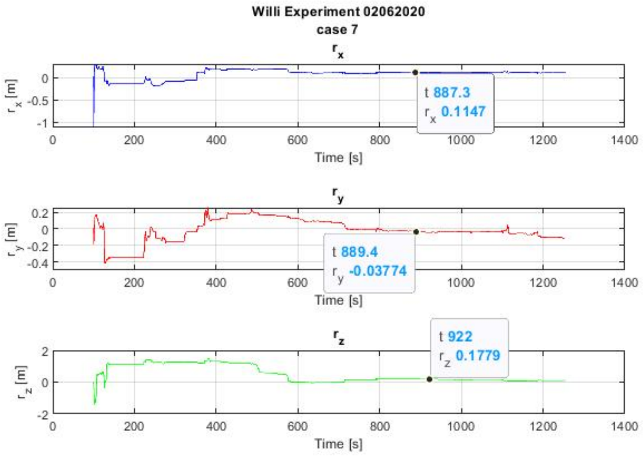

Figure 6.61 Estimated offsets of case seven

$$P\,3 = 10^{-4} * \begin{bmatrix} 1 & 0 & 0 & \vdots & 0 & 0 & 0 \\ 0 & 1 & 0 & \vdots & 0 & 0 & 0 \\ 0 & 0 & 1 & \vdots & 0 & 0 & 0 \\ \cdots & \cdots & \cdots & \vdots & \cdots & \cdots & \cdots \\ 0 & 0 & 0 & \vdots & 12 & 0 & -1 \\ 0 & 0 & 0 & \vdots & 0 & 12 & 1 \\ 0 & 0 & 0 & \vdots & -1 & 1 & 51 \end{bmatrix} \begin{bmatrix} [(m/s^2)^2] & [m^2/s^2] \\ [m^2/s^2] & [m^2] \end{bmatrix}$$

$$CC\,3 = \begin{bmatrix} 1.0000 & -0.2149 & -0.2050 & -0.1993 & -0.2333 & -0.1544 \\ -0.2149 & 1.0000 & -0.2028 & -0.1843 & -0.2230 & -0.1858 \\ -0.2050 & -0.2028 & 1.0000 & -0.1984 & -0.2199 & -0.1983 \\ -0.1993 & -0.1843 & -0.1984 & 1.0000 & -0.2201 & -0.2586 \\ -0.2333 & -0.2230 & -0.2199 & -0.2201 & 1.0000 & -0.0953 \\ -0.1544 & -0.1858 & -0.1983 & -0.2586 & -0.0953 & 1.0000 \end{bmatrix}$$

The *P3* matrix indicates that the correlations are relatively small with a simple sea environment. These weak correlations are also expressed in the correlation coefficient matrix *CC3*, because no values larger than 0.5 or even 0.3 appear in the complete matrix. Again, the significant values appear in the offset part and the error values are 0.035, 0.035, and 0.071 m in three dimensions, which means that the differences in the values would be of the order of centimetres.

Figures 6.62 and 6.63 show the estimated offsets under the condition that the catamaran was making circles in the clockwise direction. The curves for cases in the x- and y-direction take a shorter time to adjust the results than those in the z-direction. The tendency of the values for each offset component is relatively steady, and the amplitudes are similar to each other. As shown in the figures, the CR's location is behind the sensor and closer to the stern by approximately 10 cm, slightly portside from the sensor by approximately 10 cm, and 10 cm below the sensor. Again, the results demonstrate that with similar experimental conditions, the estimated offsets are similar as well.

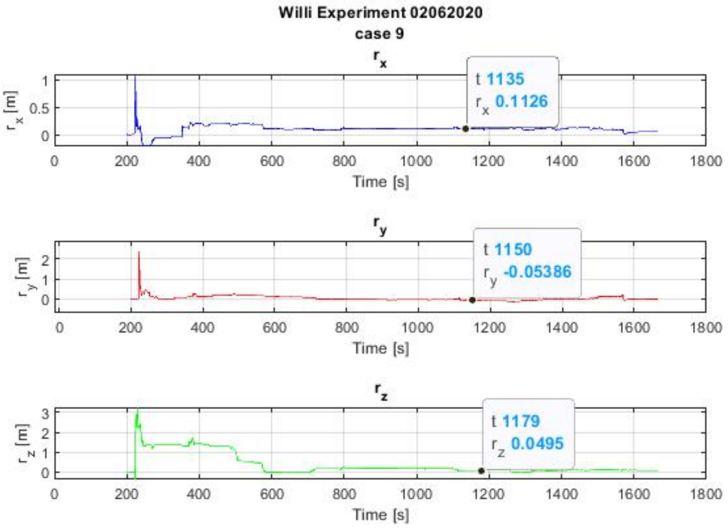

Figure 6.62 Estimated offsets of case nine

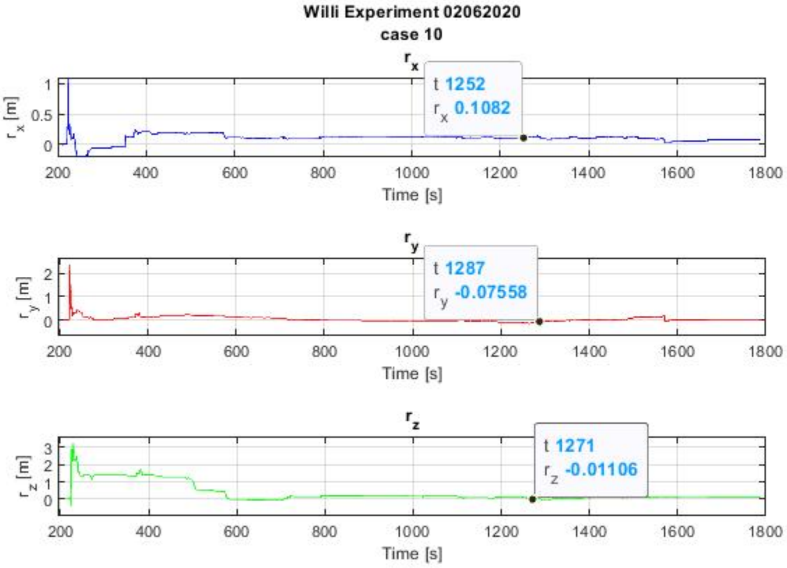

Figure 6.63 Estimated offsets of case ten

Figures 6.64 and 6.65 show the results of making circles but in the opposite direction, namely counter-clockwise, compared with cases nine and ten. As presented in the figures, much more small vibrations occur in the x- and y-direction, but the curves in the z-direction stay relatively flat and stable. The offsets of the x- and y-component finally seem to reach their expected values. In comparison with cases nine and ten, the offsets values are similar as well. Despite the catamaran's motion orientation, when performing similar motions, the respective offsets remain similar. The most probable cause for the small vibrations would be the propeller actions.

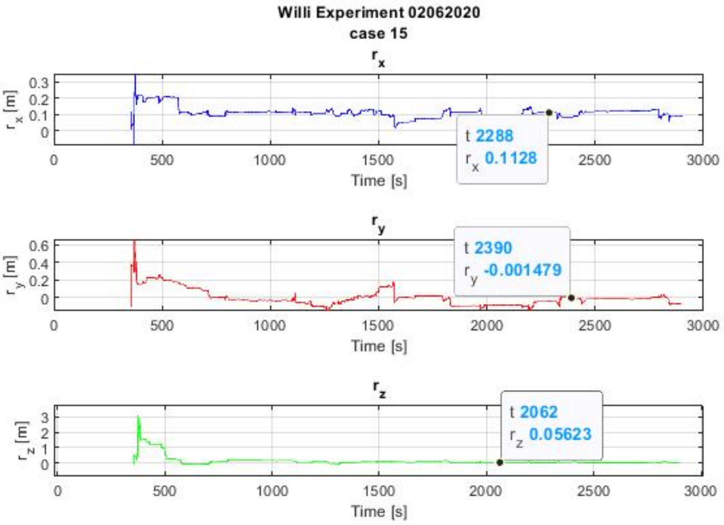

Figure 6.64 Estimated offsets of case fifteen

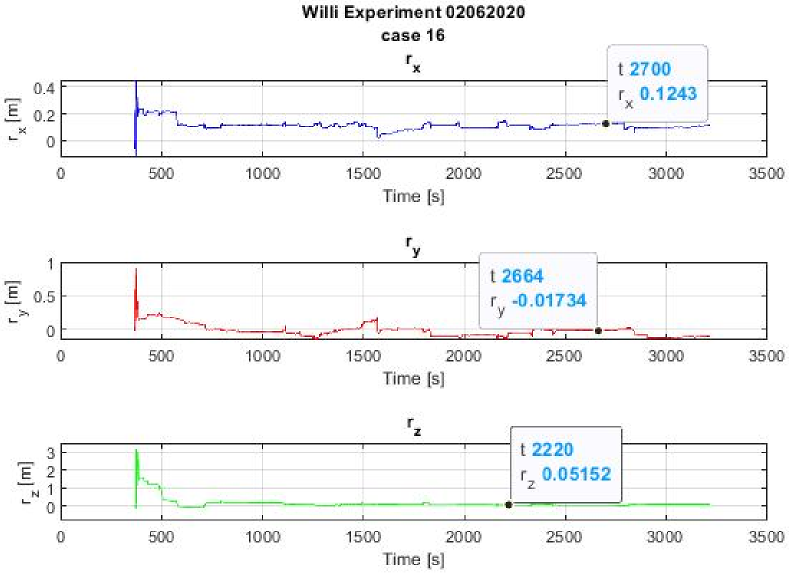

Figure 6.65 Estimated offsets of case sixteen

The matrices *P9* and *P16* express the error covariances during the catamaran's circular manoeuvres. Regardless of the orientations of the circles, the matrices are similar, with weak or even no correlations among the variables, but strong relations in the offset part. The values of the offset would change by centimetres as well, as the errors would be at 0.056, 0.066, and 0.056 m for trial sixteen. For trial nine, the errors are smaller but also of the order of centimetres.

Based on *CC9* and *CC16*, obvious correlations appear between the linear acceleration in the z-direction and the offset in the x-axis. An additional strong correlation is shown between the linear acceleration in the x-axis and the offset in the z-axis for trial nine. Oscillations appear but do not significantly change the offset values, as neither of these correlations is as strong as those in Agulhas or Simon Stevin.

$$P\,9 = \ 10^{-4} * \begin{bmatrix} 1 & 0 & 0 & \vdots & 0 & 0 & -1 \\ 0 & 1 & 0 & \vdots & 0 & 0 & 0 \\ 0 & 0 & 1 & \vdots & 1 & 0 & 0 \\ \cdots & \cdots & \cdots & \vdots & \cdots & \cdots & \cdots \\ 0 & 0 & 1 & \vdots & 11 & 0 & 0 \\ 0 & 0 & 0 & \vdots & 0 & 15 & 0 \\ -1 & 0 & 0 & \vdots & 0 & 0 & 10 \end{bmatrix} \begin{bmatrix} [(m/s^2)^2] & [m^2/s^2] \\ [m^2/s^2] & [m^2] \end{bmatrix}$$

$$CC\,9 = \begin{bmatrix} 1.0000 & 0.0113 & -0.1024 & -0.0670 & 0.0357 & -0.7117 \\ 0.0113 & 1.0000 & -0.3417 & -0.2633 & -0.1588 & -0.2644 \\ -0.1024 & -0.3417 & 1.0000 & 0.5218 & -0.1754 & -0.3221 \\ -0.0670 & -0.2633 & 0.5218 & 1.0000 & -0.2031 & -0.2052 \\ 0.0357 & -0.1588 & -0.1754 & -0.2031 & 1.0000 & -0.2112 \\ -0.7117 & -0.2644 & -0.3221 & -0.2052 & -0.2112 & 1.0000 \end{bmatrix}$$

$$P\,16 = \ 10^{-4} * \begin{bmatrix} 1 & 0 & 0 & \vdots & 0 & 0 & 0 \\ 0 & 1 & 0 & \vdots & 0 & 0 & 0 \\ 0 & 0 & 1 & \vdots & 0 & 0 & 0 \\ \cdots & \cdots & \cdots & \vdots & \cdots & \cdots & \cdots \\ 0 & 0 & 0 & \vdots & 31 & 0 & 0 \\ 0 & 0 & 0 & \vdots & 0 & 44 & 0 \\ 0 & 0 & 0 & \vdots & 0 & 0 & 31 \end{bmatrix} \begin{bmatrix} [(m/s^2)^2] & [m^2/s^2] \\ [m^2/s^2] & [m^2] \end{bmatrix}$$

$$CC\,16 = \begin{bmatrix} 1.0000 & -0.2711 & -0.2043 & -0.2418 & -0.3518 & 0.1429 \\ -0.2711 & 1.0000 & -0.1633 & -0.1095 & -0.1860 & -0.3368 \\ -0.2043 & -0.1633 & 1.0000 & -0.5182 & 0.0366 & -0.1593 \\ -0.2418 & -0.1095 & -0.5182 & 1.0000 & -0.1861 & -0.1904 \\ -0.3518 & -0.1860 & 0.0366 & -0.1861 & 1.0000 & -0.1956 \\ 0.1429 & -0.3368 & -0.1593 & -0.1904 & -0.1956 & 1.0000 \end{bmatrix}$$

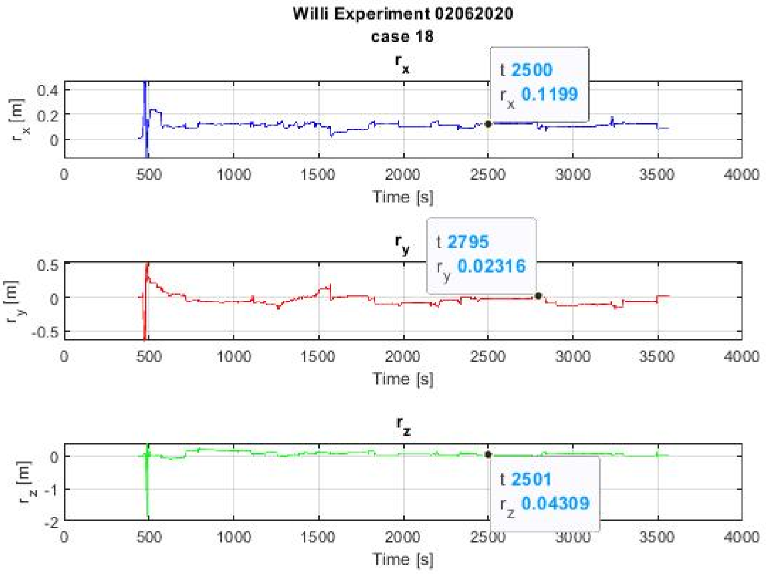

Figure 6.66 Estimated offsets of case eighteen

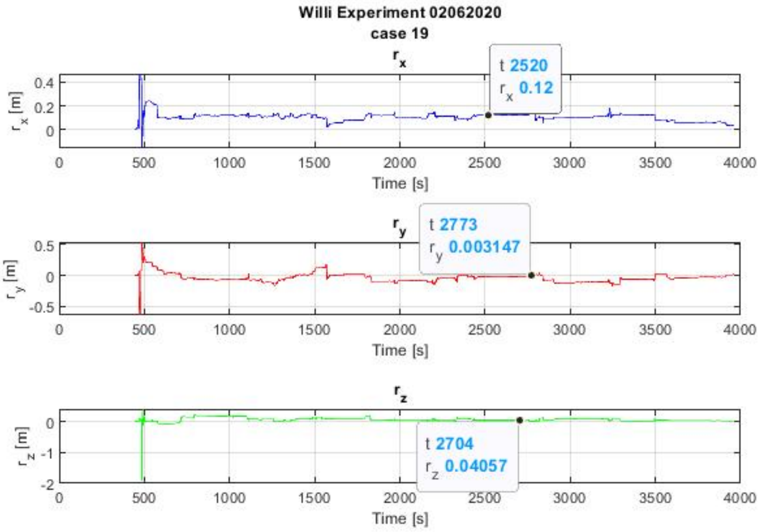

Figure 6.67 Estimated offsets of case nineteen

At the end of the experiments, the catamaran performed a few forward-motion trials, with full acceleration. The results are shown in Figures 6.66 and 6.67. Under continuous acceleration, it is plausible that small oscillations occur in the curves of the estimated offsets. However, the average of each offset remains relatively stable. Furthermore, the offset values are quite close to those of the other cases, as discussed before. Significant differences are shown in the z-direction. Under the fully forward-moving process, the surge and sway motions are reduced in comparison with the heave motion. Because the z offset is mainly dependent on the surge and sway motion, its value would be considerately reduced as well.

$$P\,19 = 10^{-4} * \begin{bmatrix} 2 & 0 & 1 & \vdots & 0 & -7 & 1 \\ 0 & 2 & 0 & \vdots & 4 & 0 & 2 \\ 1 & 0 & 1 & \vdots & 0 & -4 & 0 \\ \cdots & \cdots & \cdots & \vdots & \cdots & \cdots & \cdots \\ 0 & 4 & 0 & \vdots & 27 & 0 & 0 \\ -7 & 0 & -4 & \vdots & 0 & 47 & 0 \\ 1 & 2 & 0 & \vdots & 0 & 0 & 27 \end{bmatrix} \begin{bmatrix} [(m/s^2)^2] & [m^2/s^2] \\ [m^2/s^2] & [m^2] \end{bmatrix}$$

$$CC\,19 = \begin{bmatrix} 1.0000 & 0.2063 & 0.9509 & 0.0939 & -0.9948 & 0.2097 \\ 0.2063 & 1.0000 & 0.0399 & 0.8791 & -0.2479 & 0.1909 \\ 0.9509 & 0.0399 & 1.0000 & -0.0404 & -0.9615 & 0.1508 \\ 0.0939 & 0.8791 & -0.0404 & 1.0000 & -0.1380 & -0.2512 \\ -0.9948 & -0.2479 & -0.9615 & -0.1380 & 1.0000 & -0.1869 \\ 0.2097 & 0.1909 & 0.1508 & -0.2512 & -0.1869 & 1.0000 \end{bmatrix}$$

For the trial with the catamaran moving forward with more complicated motions, more correlations appear in the *CC* matrix. For example, the linear accelerations in the x- and z-axis are strongly correlated, the linear acceleration in the y-axis correlates to the offset in the x-direction, and the linear acceleration in the z-direction correlates to the offset in the y-axis. With the appearance of more correlations, more oscillations are occurred as well, but the calculated errors are still of the order of centimetres. Therefore, the estimated values expressed in the figures are different from those of other trials, but not dramatically so.

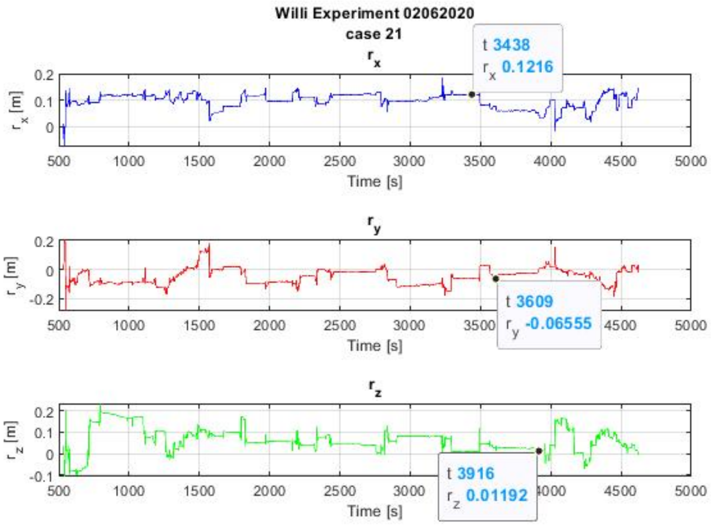

Figure 6.68 Estimated offsets of case twenty-one

The last figure expresses the results when the catamaran returned to the bank side. With the continuous actions of propellers, various velocities, diverse heading angles, and bank effects from the side, the entire set of results is full of vibrations with multiple magnitudes. Nevertheless, the average of each offset's component holds a relatively stable value, and the values are still quite similar to those of other cases.

Table 6.6 shows the estimated offsets of all cases. The data interval in the first column indicates that the measured dataset is separated into several sections based on the experimental duration and the catamaran's behaviour. From case seven, the offsets become relatively stable, with differences among the trials only up to several centimetres in all three dimensions, and sometimes even as small as a few millimetres. Considering the size of Willi and the influences from the calculated errors in the *P* matrices, these error magnitudes are tolerable. In general, the location of the CR estimated from these cases can be determined as 10 cm behind the sensor in the x-direction, 3 cm to portside of the sensor, and 8 cm below the sensor in the vertical direction.

For cases one to four, the catamaran made turns along both sides with diverse velocities due to the uneven accelerations produced by the remote controller. Therefore, a series of various offsets are estimated based on these cases. Even though the trajectories of these swerves seem to be similar, with diverse velocities and the impacts from the propellers, the estimated locations would be independent.

Cases five to eight were in the drift phase. The catamaran tried to eliminate the remaining power from the previous activities and then returned to its initial state without acceleration. Hence, there is a transition of the offsets before reaching their critical values, resulting in outliers for cases five and six. The most significant values for each axis are generated. The succedent offset values of cases seven and eight are reasonable and credible, and these values are rather analogous with the results of the following cases.

Data Interval	r_x [m]	r_y [m]	r_z [m]
1	-0.166	-0.205	-0.114
2	-0.119	-0.336	1.213
3	-0.105	-0.189	1.302
4	-0.033	-0.121	1.314
5	0.166	0.155	0.577
6	0.122	0.088	0.904
7	0.116	-0.045	0.147
8	0.114	-0.025	0.116
9	0.106	-0.020	0.096
10	0.103	-0.018	0.092
11	0.104	-0.021	0.106
12	0.103	-0.035	0.083
13	0.104	-0.038	0.078
14	0.106	-0.032	0.063
15	0.106	-0.031	0.063
16	0.105	-0.041	0.065
17	0.106	-0.044	0.061
18	0.106	-0.045	0.059
19	0.099	-0.044	0.055
20	0.099	-0.041	0.055
21	0.094	-0.038	0.055

Table 6.6 Offsets results of catamaran

From cases nine to fifteen, the catamaran was making circles with a stable velocity that was introduced by the continuous acceleration from the propellers. The curves of estimated offsets are all convergent. The average values of the offsets, as shown in the table, are close to each other. Therefore, the location of the CR in this period is reasonably well determined. When making circles, the waves would mainly impinge upon the catamaran's portside and starboard side, and judging from the mathematical model as described in Chapter 4.4.3, these increasing impacts on the sides would lead to a more significant y-component of the offset but a smaller z-component.

Case sixteen was in the transition again, and from cases seventeen to twenty, the catamaran was moving straight ahead until the edge of the water field, then turning back and moving straight again, and so forth. The manoeuvring causes oscillations in three directions. Although the offsets are of similar values, there are still some differences on the order of millimetres, and these tiny deviations can be ignored. Therefore, the offsets have been determined in these cases.

The last row describes the process when the catamaran returned to the shore. Unlike the other trials on different ships, the values of the offset seem to remain in a stable range instead of being outliers. The reason for this is mainly that the catamaran is still in the process of moving straight ahead and continuously accelerating, as in the previous cases.

As described in Figure 6.69, all the estimated offset values in the table above are normalized and compared. Except for a few of the initial cases, the offsets in three dimensions are relatively stable and close to each other, indicating that the CR moves within a narrow and well-determined range.

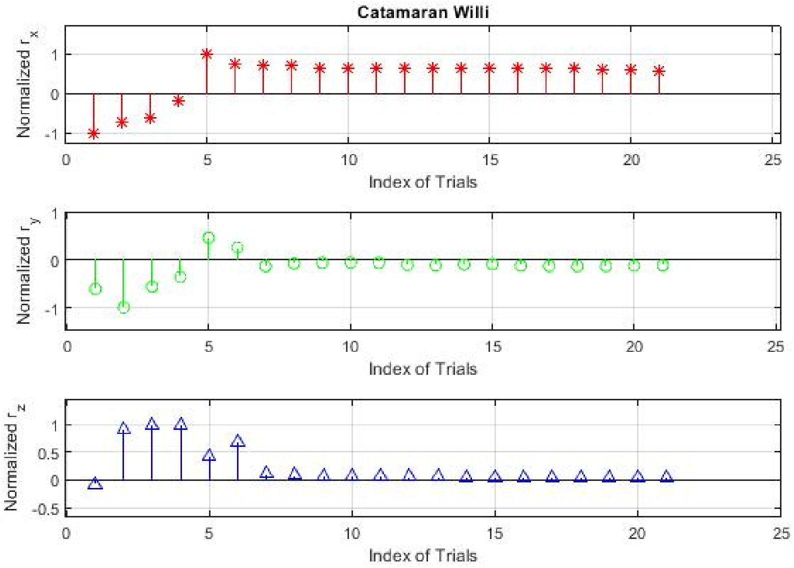

Figure 6.69 Normalization of the offset for Willi

Overall, the experiments with the catamaran were successful and the location of the CR was generally estimated. Although there are some outliers and few unmatched values, the relative range of the CR has been determined, even when the experiment could only last for several minutes. The determination algorithm is capable and fast enough to identify the range or the location of the CR, regardless of the duration of the experiments.

7 Conclusion

This chapter summarizes the present work based on analyses of the estimated results, discussing whether the determination algorithm is proved or not, whether the expected values are found, the reasons for the appearance of abnormal values, and the problems that occurred during the experiments or calculations. Finally, a plan for future research to solve the remaining problems in the current work is proposed, and further work on applications of the CR to be performed in the near future is discussed.

7.1 Summary of Results and Conclusion

The purpose of this research is to determine the CR's location based on wave-induced ship motions; therefore, in the first part of the thesis, a detailed illustration of how to define the CR, the way to locate it, and its necessity are presented. Afterward, several investigations about the CR and its related centres such as the CG, CM, CF, CB, and PP are conducted. Because the measured motion data are essential to study the CR, the measurements and their applications are studied in detail. After describing the expected variables and the known information, a primary mathematical model is constructed, and thus the complete methodology to ascertain the location of the CR is generated. In consideration of the mathematical model structure, the Kalman filter is selected because of its high performance with respect to processing the original data to mitigate errors and biases. Furthermore, its concise and explicit mathematical formation is also an advantage over the other methods.

Five different kinds of ships were utilized for the experiments, thereby enabling a comprehensive verification to test the proposed determination algorithm. In the previous chapter of this thesis, all the results from every ship are presented in detail and analysed. After analysing the estimated location of the CR or its position with respect to the known CG on various ships, a fundamental conclusion is drawn that the proposed CR's location can be found using a simple determination algorithm with the assistance of low-cost sensor boxes onboard.

For Marvin, because the ship was not moving in a river, all motions at the bow were caused manually. Thus, unstable offset values are shown in the x-direction due to introduced bow motions. In contrast, the offset values in the y- and z-axis are relatively stable when placing the sensor box on the desk of the cabin or on top. Overall, the CR’s location in the y-direction is almost along the transverse line of the ship and slightly lower than the keel in the z-direction. The CR’s location has been determined for these two directions and remains stable in a narrow range. However, it cannot be determined with certainty on the x-axis. The offset values of Marvin can be divided into two sets: one for the sensor located on the desk in the cabin, and the other for the sensor located on top of the cabin. Furthermore, the differences between these two sets of values are consistent with those between the two sensor positions, which also indicates that the CR’s location is well-determined and reasonable.

Fathom 10 is a relatively smaller ship and encountered significantly longer waves when conducting the experiments. According to all trials in 2014 and 2015, the estimated CR’s location is approximately 2 m ahead of the CG in the x-axis and approximately 0.8 m lower than the CG in the z-direction. However, the offset values are not stable in the y-axis for both years. Moreover, the offset values in the y-axis are systematic in 2015, based on the direction from which the encountered waves approached. The reason for the unstable offset values in the y-axis is that the longer encountered waves impacting on this small ship make relatively minor contributions to pitch and roll motions, such that the pitch and roll motions may even be caused by other shorter waves, rather than the dominant encountered waves on which we focused.

Many trials were implemented in Simon Stevin, and most of the offset values in the x-direction are stable and vary within a specific range, the average value of which is 6.44 m ahead of the CG and closer to the bow. The values in the z-axis are relatively stable, but vary within a wider distribution range. In contrast, the offset values in the y-direction are oscillatory, and not according to the encountered wave direction. The situation for Simon Stevin was contrary to that of Fathom 10, such that the ship was relatively longer than the encountered waves. This situation resulted in complicated sea conditions, not to mention the various velocities when conducting experiments.

A long journey of Agulhas II was recorded. Therefore, certain specific and limited parts were selected regarding two onboard sensor boxes. In total, the offset values are not stable as we expected, with discrepancies of a few meters among the trials. Nevertheless, Agulhas II is a longer ship, and this discrepancy can be tolerated except for the z-axis. It was demonstrated that the primary IMU equipped with three linear accelerometers and two or three gyroscopes in only one location at a random position in the ship is sufficient to calculate the CR's location and corresponding ship motions. When there were two sensor boxes onboard at arbitrary positions, the location of the CR could still be detected from both sensors. Theoretically, they should be identical, but there were still differences between them for each case in real-world scenarios. The characteristics of each sensor box could cause slight differences between them. However, the reason for a more significant discrepancy that appeared in the z-direction for Agulhas II is still not clear. The much higher installation position of the sensor box may strongly affect the measured ship motions, especially for the component introduced by the gravitational acceleration, thus generating this discrepant value for z-direction.

The final experiments about the catamaran have been well interpreted to imply that the determination algorithm can be applied to research, because the water field in which the experiments were conducted was rather clear with respect to the surrounding wave conditions. The catamaran was constructed with specific parameters. Thus, the results are more easily analysed owing to the significant degree of known information. Furthermore, the results demonstrated that the CR's location remains relatively stable and varies within a narrow range, regardless of the manoeuvres performed.

Based on all the ships' results, it has been shown that the Kalman filter with a straightforward model, coping with the effects of geometric offsets, along with the assistance of the Euler transformation, is sufficient to calculate the location of the CR and ship motions at the CR. The simple model is preferred even though a more sophisticated system model may lead to better reductions in the noise and biases, because previous knowledge of the ship's dynamic parameters, damping coefficient, or inertia information would not be completely obtained before the ship's proper operations.

The P matrix is introduced to explain certain differences that appeared in the final estimated values of the offset, especially when the results differ but are calculated under similar sea states. For example, significant errors affected the estimated offset for the ship Agulhas, with magnitudes on the order of metres. Meanwhile, for the ship Simon Stevin, more minor errors are generated, and thus the estimated values of the offset are more stable and deviated slightly be approximately 1 m, which is relatively acceptable in comparison to the size of the ship itself. Nevertheless, not all differences in results can be explained by the P matrix. For example, significant differences appeared for the ship Fathom 10. Although the errors seem to be small with magnitudes of centimetres, the final estimated values of the offset change by decimetres or, much worse, even metres. Considering the size of Fathom 10, this level of change would be too much to accept, as we required the deviation to be less than 1% of the ship's length. However, when considering other factors, such as the encountered waves, the results seem reasonable. Because the ship was under relatively longer waves, complicated motions were generated, more significant biases or noises would be introduced into the measured data, thus leading to the inaccurate estimations.

Overall, the results seem to be quite sensitive to the variations in the ship's velocity and incident waves' characteristics. For example, the relative proportions of the ships and waves affect ship motions sideways primarily. Thus, the more significant oscillations more often appear in the y-axis. Still, on the whole, it can be surmised that under a similar sea state, a similar result is acquired. No unique values of the locations of CR are, because errors caused by the measurement devices or the ship itself or generated during processing should be clarified. However, specific ranges of the offset values are obtained for each ship as we expected. In actual sea trials, there are always many uncertainties when implementing the experiments. Therefore, it is possible and tolerable that some of the abnormal results could not be explained based on the limited knowledge we are aware of for now.

In conclusion, the proposed determination algorithm and an essential IMU are applicable and capable to determine the CR's location and the ship motions at the CR. Except for a few outliers, the remaining estimated results are qualified to be regarded as satisfying the requirements. However, there are still some problems with this algorithm. A few uncertainties about the strange results should be settled, and when encountering complicated waves, the locations of the CR would be strongly affected. Therefore, the stability of the algorithm should be improved, and more ship parameters should be introduced to separate the motions in three dimensions clearly and precisely.

7.2 Future Work

In this work, the wave information obtained from nearby buoys is provided only for one of the experiments. The information is imprecise owing to the distance between the experimental location and the buoys. When utilizing the ship motions at the CR, the current wave information is estimated, as shown in Chapter 6.2. Comparing the wave characteristics from these two different sources is insufficient to say that the waves are the same. The causes of differences are difficult to distinguish because of the uncertainty and inaccuracy of the compared wave information. More sources of wave characteristics are highly needed in the proximate water zone, either recorded by buoys or calculated from other methodologies.

The construction of the mathematical model to determine the location of the CR is quite clear and easily understood, without any complicated ship hydro-coefficients. So far, the model is capable of calculating the location of the CR. However, even when the possible causal factors of strange values have been eliminated, outliers still exist. The remaining reason will be the inaccuracy of the initial mathematical model. This situation occurs mostly in the larger ship with a longer voyage. More complicated sea states would be encountered with longer sailing times, especially in the open sea. For a more realistic application in the future, the mathematical model should introduce the ship’s static and dynamic parameters to enhance the stability and universal performance without restrictions of water fields, sizes, or kinds of the ships.

The measurement devices that were installed onboard are well-developed and sufficient but low-cost. Additional functions are also possible to include in the near future, but still with the criteria of lower cost and easy operability by anyone on the ship.

Further investigations will focus on the problems as we illustrated in the previous chapter, such as the appearance of the outliers. Furthermore, regardless of all the probable factors, such as the direction of encountered waves, the ship's velocities, and the ship's manoeuvrability, the determined location of the CR would be in a specific range or even better at a unique position. The research on the relationship between the CR's location and the various influencing parameters is conducive to the fundamental understanding of a ship's dynamic behaviour in waves. Once the CR is ascertained, the next step will be to use the motions at the CR to estimate or predict the characteristics of the encountered waves.

Appendix

A Calculation of Motion Spectra from Wave Buoy Data

The calculation of motion spectra from the directional wave spectra as obtained from the wave-buoy is outlined in this section. Wave-buoy spectra are given as power spectral densities $S(\omega_f, \alpha)$, where ω_f denotes the frequency and α is the wave direction relative to the ship's velocity vector. When waves at a certain frequency ω_f pass a moving ship, a different frequency is apparent to the ship, which is the encounter frequency ω_e. In deep water, these two frequencies are related by

$$\omega_e = \omega_f \left(1 - \frac{v \cos(\alpha)}{g} \omega_f\right) \quad (22)$$

where g represents the gravitational acceleration and v denotes the vessel's speed. A relative angle of $\alpha = 0°$ represents following waves in this convention. In Figure A.0.1, the encounter frequency is plotted as a function of the sea-state frequency for following seas and at a particular ship speed of 7.5 knots. The graph indicates that up to three values of ω_f from regions I, II, and III may be mapped onto one value of ω_e. In the current experiment, the following waves were found mainly in region I.

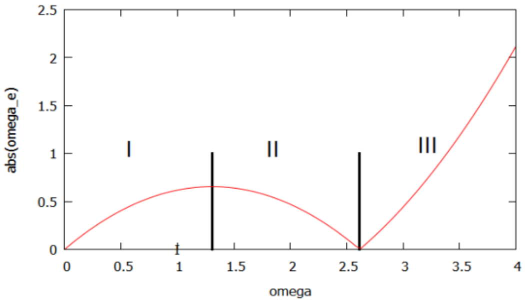

Figure A.0.1 Encounter frequency ω_e as a function of sea-state frequency ω_f

The encounter spectrum $S_e(\omega_e, \alpha)$ as seen by the moving vessel is related to the wave spectrum by (Price, 1974 [81])

$$\mathrm{S_e}(\omega_e(\omega_f), \alpha) = \frac{\mathrm{S}(\omega_f, \alpha)}{\left|\frac{d\omega_e}{d\omega_f}\right|} \quad (23)$$

At the boundary between region I and II, the factor $|\frac{d\omega_e}{d\omega_f}|$ vanishes; this creates a singularity in the encounter spectrum. Because the wave buoy spectra showed no energy in this frequency range, no measures for removing the singularity had to be taken. From the encounter spectrum, the motion spectra for the different degrees of freedom $S_i(\omega_f)$ can obtained as

$$S_i(\omega_e) = |h_i(\omega_e, \alpha)|^2 \, S(\omega_e, \alpha) \quad (24)$$

where i denotes the index of the degree of freedom and $h_i(\omega_e, \alpha)$ is the corresponding response amplitude operator (RAO). In this research, the RAOs were calculated by the strip theory program Octopus [82] and Hydrostar (Bureau, 2018 [83]).

References

[1]. Basic transformation geometry, http://www.gradeamathhelp.com/transformation-geometry.html. Retrieved by 06.07.2021.

[2]. Decaudin P. (1996): Geometric Deformation by merging a 3D-object with a simple shape, Graphics Interface' 96 proceedings.

[3]. Ault, J.; Bower, A.; Qi, Y. (2021): Dynamics and Vibrations, textbook.

[4]. Fernandes, A. C.; Asgari, P.; Soares, A. R. W. (2016): Asymmetric roll center of symmetric body in beam waves, Ocean Engineering.

[5]. Costa, Daniel. de. Oliveira, et al (2018): Instantaneous center of rotation in pitch response of a FPSO submitted to head waves, 37th International Conference on Ocean, Offshore and Arctic Engineering, OMAE.

[6]. Rogne, R. H.; Johansen, T. A.; Fossen, T. I. (2015): On attitude observers and inertial navigation for reference system fault detection and isolation in dynamic positioning. In Proc. European Contr. Conf. (ECC), 3665-3672. Linz, Austria.

[7]. Triantafyllou, M.; Athans, M. (1981): Real time estimation of the heaving and pitching motions of a ship, using a Kalman filter. IEEE OCEANS, p.1090–1095, Boston, USA.

[8]. Fossen, T. (2011): Handbook of Marine Craft Hydrodynamics and Motion Control. Wiley, 2011. ISBN 9781119991496.

[9]. Bont, J. D.; van der Molen, W. et al (2010): Calculations of the motions of a ship moored with moormaster units, PIANC MMX Congress Liverpool UK 2010.

[10]. Yang, W. L.; Wei, S. F. et al. (2009): Numerical simulation and testing analysis of adaptive heave motion measurements, 2009 International Conference on Measuring Technology and Mechatronics Automation.

[11]. Küchler, S.; Eberharter, J. K., et al (2011): Heave motion estimation of a vessel using acceleration measurements, 18th IFAC World Congress.

[12]. Marconi, L.; Isidori, A.; Serrani, A. (2002): Autonomous vertical landing on an oscillating platform: an internal-model based approach, Automatica, 38(1), 21-32.

[13]. Ivče, R.; Jurdana, I.; Mohović, Đ. (2010): Parametric roll monitoring with an integrated ship's system, 52th International Symposium ELMAR: 333-336.

[14]. Nicolau, V. (2003): The influence of the ship's steering machine over yaw and roll motions, University of Galati, Fascicle III.

[15]. Ibrahim, R., A.; Grace, I., M. (2009): Modeling of ship roll dynamics and its coupling with heave and pitch, Mathematical Problems in Engineering, Volume 2010.

[16]. Wicaksono, A.; Kashiwagi, M. (2018): Wave-induced steady force and yaw moments of a ship advancing in oblique seas, Journal of Marine Science and Technology, volume 23, pages 767-781.

[17]. Das, S. K.; Das, S. N.; Sahoo, P. K. (2006): Investigation of sway, roll and yaw motions of a ship with forward speed: numerical modeling for flared up conditions, 5th International Conference on High Performance Marine Vehicles.

[18]. Zhang, B. J.; Ma, S., N. (2019): Research on motion response and sickness incidence of the fishing boat in heading and quartering seas, Journal of FisheriesScience.com.

[19]. Umeda, N.; Hashimoto H. (2002): Qualitative aspects of nonlinear ship motions in following and quartering seas with high forward velocity, Journal of Marine Science and Technology 6:111-121.

[20]. Maki, A.; Naoya, U. (2009): Bifurcation and chaos in yaw motion of a ship at lower speed in waves and its prevention using optimal control, 10th International Conference on Stability of Ships and Ocean Vehicles.

[21]. Ueng, Shyh-Kuang; Lin D.; Liu Chieh-Hong (2008): A ship motion simulation system, Springer-Verlang, Virtual Reality, pp. 65-76.

[22]. Woolley, M. (2009): Time for the navy to get into the game, Proceedings Magazine, U.S Naval, Vols. 135/4/1,274.

[23]. Ergum, D.; Romesh, M. (2009): Developing an effective maritime education and training system- TUDEV, ACCRA-GHANAN: s.n., IMLA Conference.

[24]. Sandaruwan, D., et al (2010): A six degrees of freedom ship simulation system for maritime education, the International Journal on Advances in ICT for Emerging Regions, 2010(03) 02: 34-47.

[25]. Ayaz, Z., Turan; O., Vassalos, D. (2003): A 6 DOF maneuvering model for controlled ship motions of POD-driven ships in astern seas, IFAC Maneuvering and Control of Marine Craft.

[26]. Giron-Sierra, J. M., et al. (2004): Advance in the 6 DOF motions model of a fast ferry, IFAC Conference on Computer Applications in Marine Systems.

[27]. Center of Mass, Wikipedia: https://en.wikipedia.org/wiki/Center_of_mass. Retrieved by 06.07.2021.

[28]. Krate, P. (2013): The impact of sloshing liquids on ship stability for various dimensions of partly filled tanks, The International Journal on Marine Navigation and Safety of Sea Transportation, vol. 7, No. 4, pp. 481-489.

[29]. Hu, Y.; Tao, L. (2013): Real time zero phase filtering for heave measurement, 11th IEEE International Conference on Electronic Measurement & Instruments, 321-326.

[30]. Bryne, T. H.; Rogne, R. H.; Fossen, T. I. (2016): Attitude and heave estimation for ships using MEMS-based inertial measurements, IFAC, International Federation of Automatic Control, 568-575.

[31]. Lee, S. K.; You, J. M. et al. (2016): Experimental study on the six degree-of-freedom motions of a damaged ship floating in regular waves, IEEE Journal of Oceanic Engineering, Vol. 41, No.1, 40-49.

[32]. Lee, S. Y.; Rhee, K. P. (2002): Design of ship-motion regulators for foil catamarans in irregular sea waves, IEEE Journal of Oceanic Engineering, Vol.27, No. 3, 738-752.

[33]. Journée, J.; Adegeest L. J. M. (2003): Theoretical manual of strip theory program “SEAWAY for Windows”, Ship Hydromechanics Laboratory, Delft University of Technology, Advance Maritime Consulting, Report 1370.

[34]. Journée, J. (2001): Verification and validation of ship motions program SEAWAY, Ship Hydromechanics Laboratory, Delft University of Technology, Report 1213a, http://www.shipmotions.nl. February 2001.

[35]. Söding, H. (2006): Program PDSTRIP: Public domain strip Method.

[36]. Tannuri E.A.; Sparano J.V.; Simos, A.N.; Da Cruz J.J. (2003): Estimating directional wave spectrum based on stationary ship motion measurements. Applied Ocean Research, 25(5):243–261, 2003.

[37]. Chiotoroiu, L (2015): Ship Theory, textbook.

[38]. Schneekluth, H.; Bertram, V. (1998): Ship Design for Efficiency and Economy, Butterworth-Heinemann.

[39]. Abankwa, N. O.; Bowder, J., et al. (2018): Estimating the longitudinal center of flotation of a vessel in waves using accelerations measurements, IEEE Sensor Journal.

[40]. Herder, J. L.; Schwab, A. L. (2004): On dynamically equivalent force systems and their application to the balancing of a broom of the stability of a shoe box, in Proceedings of DETC04 ASME Design Engineering Technical Conferences and Computers and Information in Engineering Conference, New York, USA.

[41]. Butuşină, P. D.; Dinu, D. (2012): Ship's pivot point in current and swell, the Pilot.

[42]. Butusina, P.; Dinu, D. (2012): Experiment and theory regarding the pivot point, Constanta Maritime University Annals, Year XII, vol. 15.

[43]. Capt. Cauvier, H. (2008): The pivot point, the Pilot, No. 295.

[44]. Seo. S. G. (2016): Safer and more efficient ship handling with the pivot point concept, the International Journal on Marine Navigation and Safety of Sea Transportation, vol. 10, No. 4.

[45]. Karolius, K. B.; Vassalos, D. (2018): Tearing down the wall- the inclining experiment, Ocean Engineering.

[46]. Froude, W. (1861): On the rolling of ships, Read at the Second Session of the Institution of Naval Architects.

[47]. Chen, Hamn-Ching; Liu Tuanjie (2001): Time-domain simulation of large amplitude ship roll motions by a chimera RANS method, Proceedings of the Eleventh (2001) international Offshore and Polar Engineering Conference.

[48]. Fernandes, A. C.; Asgari, P.; Soares, A. R. W. (2016): Asymmetric roll center of symmetric body in beam waves, Ocean Engineering.

[49]. Costa, Daniel. de. Oliveira, et al (2018): Instantaneous center of rotation in pitch response of a FPSO submitted to head waves, 37th International Conference on Ocean, Offshore and Arctic Engineering, OMAE.

[50]. Kliava, J.; Mégel, J. (2010): Non-uniqueness of the point of application of the buoyance force, European Journal of Physics, 31(2010), 741-762.

[51]. Techet, A. H. (2004): Hydrodynamics for ocean engineers, textbook.

[52]. Jeong Tae-Gweon (2012): A study on comparison between center of lateral resistance and pivot point being used in handling ships at the present time, pp. 160~161.

[53]. Carreño J. E.; Mora J. D., Pérez F. L. (2012): A study of shallow water's effect on a ship's pivot point, INGENIERÍA E INVESTIGACIÓN Vol. 32 No. 3, 27-31.

[54]. Perera L. P. (2015): Ship maneuvering prediction under navigation vector multiplication based pivot point estimation, IFAC, International Federation of Automatic Control.

[55]. Rules for Classification: Ships, Part 3 Hull, Chapter 4 loads, DNV GL, 2020.

[56]. Sotnikova M. V. (2012): Linear model identification by least squares method as applied to ship motion, Gyroscopy Navigation 3, 100-103.

[57]. Åström K. J.; Källström C. G. (1976): Identification of ship steering dynamics, Automatica Volume 12, Issue 1, page: 9-22.

[58]. Clark P.; Kirsteins I.; Atlas L. (2010): Multiband analysis for colored amplitude-modulated ship noise, 2010 IEEE International Conference on Acoustics, Speech and Signal Processing.

[59]. Fitch J. P.; Lehman S. K., et al. (1991): Ship wake-detection procedure using conjugate gradient trained artificial neural networks, IEEE Transactions on Geoscience and Remote Sensing, Volume 29, Issue 5, page: 718-726.

[60]. Abankwa, N. O. et al. (2015): Ship motion measurement using an inertial measurement unit, IEEE 2nd World Forum on Internet of Things (WF-IoT).

[61]. Hibbert, G. K.; Lesser, G. R. (2013): Measuring vessel motions using a rapid-deployment device on ships of opportunity, Coasts and Ports 2013, 21st Australasian Coastal and Ocean Engineering Conference and the 14th Australasian Port and Harbour Conference.

[62]. Godhavn, J. M. (2000): High quality heave measurements based on GPS RTK and accelerometer technology. In Proceedings of MTS/IEEE OCEANS, volume 1, 309-314. Providence, RI.

[63]. Fossen, T.; Perez, T. (2009): Kalman filtering for positioning and heading control of ships and offshore rigs. IEEE Control Systems Magazine, 29(6), 32-46.

[64]. Trapezoidal Rule, https://www.math24.net/trapezoidal-rule. Retrieved by 06.07.2021.

[65]. cumtrapz, https://de.mathworks.com/help/matlab/ref/cumtrapz.html. Retrieved by 06.07.2021.

[66]. pwelch,https://de.mathworks.com/help/signal/ref/pwelch.html?searchHighlight=pwelch&s_tid=srchtitle. Retrieved by 06.07.2021.

[67]. Butterworth, S. (1930): On the theory of filter amplifiers, the Wireless Engineer, vol.7, pp. 536-541.

[68]. Butter, https://www.mathworks.com/help/signal/ref/butter.html. Retrieved by 06.07.2021.

[69]. Zumbahlen H. (2011): Linear circuit design handbook, Engineeri Engineeri Analog Devices Inc.

[70]. FIR,https://en.wikipedia.org/wiki/Finite_impulse_response#:~:text=In%20signal%20processing%2C%20a%20finite,to%20zero%20in%20finite%20time. Retrieved by 06.07.2021.

[71]. fir1,https://de.mathworks.com/help/signal/ref/fir1.html?searchHighlight=fir1&s_tid=srchtitle#d123e63932. Retrieved by 06.07.2021.

[72]. Ehrman, L. M.; Lanterman, A. D. (2008): Extended Kalman filter for estimating aircraft orientation from velocity measurements, IET Radar Sonar Navigation, 2008 2 (1), pp. 12-16.

[73]. Wan, E. A.; van der Merwe, R. (2000): The unscented Kalman filter for nonlinear estimation, Proceedings of the IEEE 2000 Adaptive Systems for Signal Processing, Communications, and Control Symposium.

[74]. Kulikov, G. Y.; Kulikova, M. V. (2016): The accurate continuous-discrete extended Kalman filter for radar tracking, IEEE Transactions on Signal Processing, Vol. 64, No. 4.

[75]. Zhang, Pifu; Gu, J., et al. (2005): Navigation with IMU/GPS/Digital compass with unscented Kalman filter, Proceedings of IEEE International Conference on Mechatronics & Automation.

[76]. Du, Hongsong; Cheng, Jianhua; Wang, Bingyu (2013): Design of adaptive Kalman filter algorithm in integrated navigation system for land vehicles, Proceedings of 2013 IEEE International Conference on Mechatronics and Automation.

[77]. Germani, A.; Manes, C.; Palumbo, P. (2005): Polynomial extended Kalman filter, IEEE Transactions on Automatic Control, Vol. 50, No. 12.

[78]. Kalman, R. E. (1960): A new approach to linear filtering and prediction, Journal of Basic Engineer, 35-45.

[79]. Gupta, N. (2007): Kalman filtering in the presence of state space equality constraints, Numerical Analysis Group, Oxford University Computing Laboratory, Report no. 07/14.;

[80]. Korte, H.; Stuppe, S.; Wesuls, J. H.; Takagi, T. (2017): The inertia value transformation in maritime applications, INTEC.

[81]. Price, W. G.; Bishop, R. E. D. (1974): Probabilistic theory of ship dynamics, ch. 9.

[82]. Octopus Office 6 User Manual (2010): https://www.scribd.com/document/286098640/User-Manual-OCTOPUS-OFFICE-SHIP-MOTION-ANALYSIS-SOFTWARE. Retrieved by 06.07.2021.

[83]. Bureau Veritas (2018): Hydrostar for experts, user manual, the manual is part of the software download, https://marine-offshore.bureauveritas.com/software. Retrieved by 06.07.2021.

[84]. Simon Stevin, https://www.vliz.be/en/rv-simon-stevin. Retrieved by 06.07.2021.

[85]. S. A. Agulhas II, https://en.wikipedia.org/wiki/S._A._Agulhas_II. Retrieved by 06.07.2021.

[86]. Bekker, A.; Omer, H. (2018): Human responses to wave slamming vibration on a polar supply and research vessel, Applied Ergonomics 67. 71-82.

[87]. Taylor, J. R. (1997): An introduction to Error Analysis: The study of Uncertainties in Physical Measurement, 2nd ed. Sausalito, CA: University Science Books.

[88]. corrcoef, https://de.mathworks.com/help/matlab/ref/corrcoef.html, Retrieved by 06.07.2021.

[89]. Open Sea Map, http://map.openseamap.org/?mlat=-34.189297&mlon=18.433641&zoom=14f&mtext=False%20Bay%20Yacht%20Club&layers=BFTFFFTFFTF0FFFFFFFF, Retrieved by 19.06.2021.

Abschließende Erklärung

Ich versichere hiermit, dass ich meine Promonsarbeit ´Sensor Integration for Ship Motion Analysis´ selbständig und ohne fremde Hilfe angefertigt habe, und dass ich alle von anderen Autoren wörtlich übernommenen Stellen wie auch die sich an die Gedankengänge anderer Autoren eng anlegenden Ausführungen meiner Arbeit besonders gekennzeichnet und die Quellen zitiert habe.

Oldenburg, den

...(Unterschrift)...